STUDY OF DIFFUSION AND CONDUCTION IN LITHIUM GARNET OXIDES
$Li_xLa_3Zr_{x-5}Ta_{7-x}O_{12}$ (x=5-7) WITH INTERATOMIC POTENTIALS

By

Jin Dai

A DISSERTATION

Submitted to
Michigan State University
in partial fulfillment of the requirements
for the degree of

Materials Science and Engineering—Doctor of Philosophy

2023

ABSTRACT

Lithium-ion batteries, based on the pioneering work of three Nobel Laureates, are everywhere in our lives from portable electronics, electric vehicles, to grid storage. However, they currently employ liquid electrolytes containing flammable organic solvents that could lead to a fire if batteries are overheated. Solid electrolytes, also called fast-ion conductors or superionic conductors, are alternatives with the uttermost safety. Among various solid electrolytes, lithium garnet oxides are a promising family of materials due to their high ionic conductivity and electrochemical stability. This work discusses the study of diffusion and conduction in $Li_xLa_3Zr_{x-5}Ta_{7-x}O_{12}$ (x=5-7) garnet oxides using computational methods. We developed two new generations of interatomic potentials, induced dipole, and machine learning, for this composition series. We compared them with existing interatomic potentials in terms of force/virial error against density-functional theory, prediction of phase transition, self-diffusivity, and ionic conductivity, and found machine learning interatomic potentials have the best accuracy. We then applied machine learning interatomic potentials to investigate the temperature and composition dependence of diffusion and conduction in bulk materials and the influence of grain boundary structure on ionic conductivity. We believe that the atomic insight obtained from this work could be worthwhile in understanding the bottleneck of materials performance and could provide guidance on further improvements.

ACKNOWLEDGEMENTS

TABLE OF CONTENTS

CHAPTER 1 Introduction

1.1 The world's energy issues and energy storage systems

Energy plays an important role in human lives, and most of them are generated from the fossil fuels such as coal, natural gas, petroleum, etc. However, the ever-increasing demand for energy and the limitation of fossil fuel due to the accessibility and climate change require the shift of electricity generation from fossil fuels to renewable energy sources such as wind, solar, hydropower, etc. According to the world energy outlook 2022, the global energy share of electricity generation from solar photovoltaic (PV) and wind will increase from 10% in 2021 to 40% by 2030, and 70% by 2050[1]. Therefore, to efficiently use intermittent clean energy, there is a motivation to develop energy storage (ES) systems that store the electrical energy when the demand is low and release it when the demand is high.

Energy storage (ES) technologies can be classified into five scientific categories, mechanical, thermal, electrical, chemical, and electrochemical[2, 3]. Mechanical ES includes four types, pumped-storage hydroelectricity (also known as pumped hydro), compressed air energy storage (CAES), liquid air energy storage (LAES), and flywheels. Thermal ES includes thermal chemicals, sensible thermal, and latent thermal. Chemical ES stores the energy/power in the form of gas, called power to gas or PtG, like hydrogen and synthetic natural gas (SNG). Electrochemical ES such as rechargeable batteries convert electrical energy from a power grid stored in its electrodes into chemical energy and then convert it back to electric energy by an electrochemical reduction-oxidation (redox) reaction. Electrical ES like supercapacitors store energy electrostatically without chemical reactions, utilizing high surface area electrode materials and thin dielectrics to achieve higher capacitance.

Figure 1a summarized the range of discharged time at a rated power and energy capacity

of ES systems. It can be seen that different technologies have different characteristics and can be mapped to the most suited applications. For example, PtG has the highest energy capacity and the longer discharge time at rated capacity and therefore is suitable for storing a large amount of energy that is discharged over long periods, however, they are still in the research and demonstration stage. Pumped hydro has the highest energy capacity and a daily based energy to power shift ability and therefore is most suited to support the national grid energy storage, in addition, it is the most commercially mature technology and currently occupies over 97% of the total storage capacity in operation[4]. Supercapacitors and batteries have lower energy capacity and shorter discharge time at rated power and therefore are suited for short-term and higher-power ES systems. Even though supercapacitors and batteries are similar as they both store and release electrical energy, their applications are different. Supercapacitors can release a large amount of energy in a very short time, however, their energy density is still very low as shown in **Figure 1**b, and therefore are suited for a small burst of power. In comparison, batteries have high energy density and can convert energy on an hourly basis and therefore are commonly used in solar and wind energy storage to compensate for the day-night load imbalance.
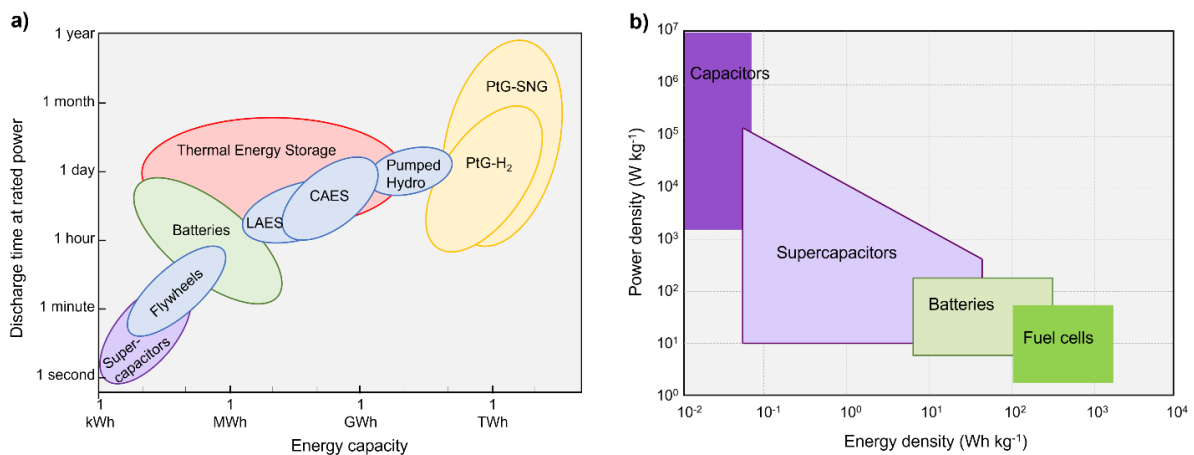
Figure 1 (a) Comparison of the range of the discharge time at a rated power and energy capacity of different energy storage (ES) systems[4]. (b) Ragone plot of performance ranges of various energy storage devices[5].

2

1.2 Li-ion battery

Li-ion batteries (LiBs) are the most common ES system and have been widely used in our daily life from portable electronics to electric vehicles. They outperform all the other rechargeable batteries such as nickel–metal hydride (Ni-MH), Ni-cadmium (Ni-Cd), and lead acid in terms of the gravimetric and volumetric energy densities (**Figure 2**)[6, 7]. In 2019, the Nobel Prize in Chemistry was awarded jointly to M. Stanley Whittingham, John B. Goodenough, and Akira Yoshino for the development of rechargeable LiBs. **Figure 3** shows the three-generation batteries designed by them.
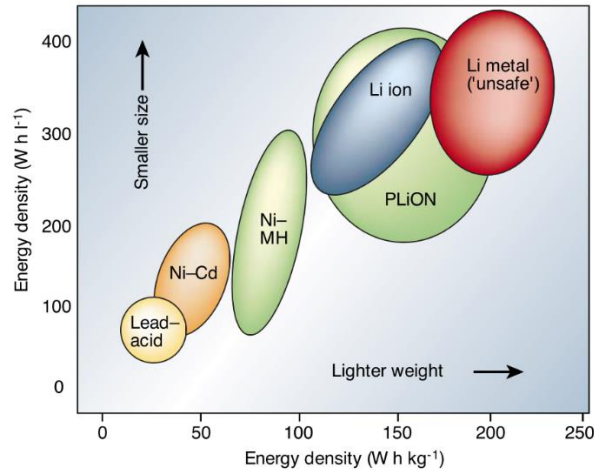
Figure 2 Energy density for different rechargeable batteries[6].

In 1972, Prof. Whittingham developed the first generation of rechargeable Li metal battery using titanium disulphide (TiS_2) as the positive electrode, Li metal as the negative electrode, and lithium perchlorate in dioxolane as the electrolyte with the potential of 2 V. TiS_2 is a light material and has a high energy density that meets the requirement of the battery electrode. In addition, TiS_2 is a layered structure that easy for ions to intercalate/deinterclate. Using Li metal as a negative electrode arising from the fact that Li is the lightest metal (0.534 g cm^{-3}) and the most electropositive (–3.04 V vs standard hydrogen electrode), which enables the high theoretical

specific capacity (3860 mA h g^{-1}) and high-output voltage and therefore high-energy density, respectively. Unfortunately, this trailblazing work soon encountered a safety issue, during each subsequent charge-discharge recycle, Li dendrite formation at the interface of Li-metal/liquid electrolyte propagates and penetrates the barrier and contacts the positive electrode, causing a short circuit and leading to an explosion. In 1980, Prof. Goodenough expanded Whittingham's work and discovered that by replacing the metal sulphide (TiS$_2$) in the positive electrode with a metal oxide (LiCoO$_2$), which also has a layered structure, lightweight but a higher potential of 4V, the capacity of battery could be doubled. This discovery is the decisive step in our "mobile living" life. LiCoO$_2$ is still the dominant material for the positive electrode nowadays. In the meantime, Prof. Yoshino made another significant breakthrough by using petroleum coke as the negative electrode. Petroleum coke is also a layered structure and enables Li-ions to intercalate/deinterclate. Since the presence of Li is ionic instead of metallic state, this type of battery is called a Li-ion battery. This rocking-chair technology solved the dendrite issue in Li-metal batteries.

Specifically, during the discharging (spontaneous) process, Li-ions deintercalated from the layered graphite carbon (anode) and migrate across the electrolyte to intercalate into the layered structure of metal oxide (cathode), in the meanwhile, the electrons flow from the anode to the cathode through the external circuit to compensate for electroneutrality. The reactions are:

Anode reaction:
$$Li_xC \xrightarrow{discharge} xLi^+ + xe^- + C$$

Cathode reaction:
$$Li_{1-x}CoO_2 + xLi^+ + xe^- \xrightarrow{discharge} LiCoO_2$$

Overall reaction:
$$Li_xC + Li_{1-x}CoO_2 \xrightarrow{discharge} C + LiCoO_2$$
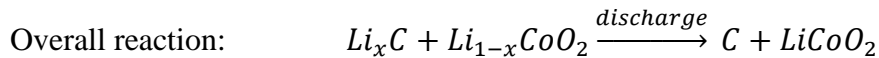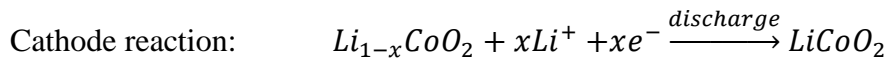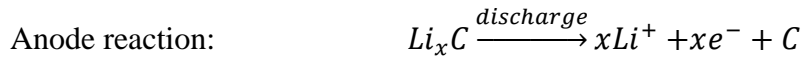
This process is in reverse for the charging process.

LiBs apply organic liquid as electrolytes, most of which are solutions of lithium salt in mixtures of two or more solvents, e.g., 1M solutions of LiPF$_6$ dissolved in 1:1 volume EC (ethylene

carbonate) and PC (propylene carbonate). These kinds of organic liquid electrolytes are flammable and have poor electrochemical stability. Therefore, to solve this safety issue, there is a need for the development of non-flammable solid-state electrolytes (SSEs) for LiBs[8-10].
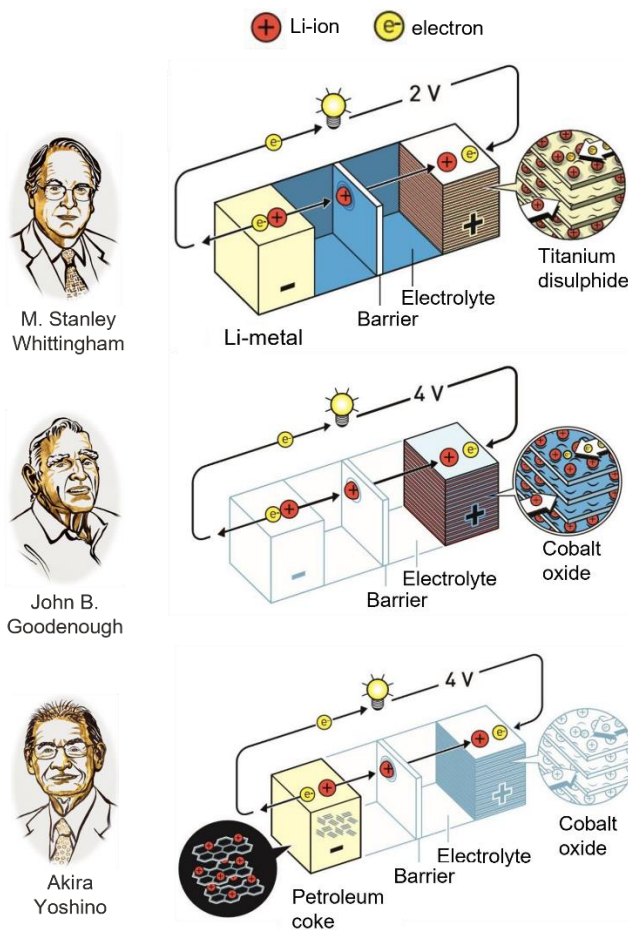
Figure 3 The most powerful batteries developed by the Nobel Prize winners. All the batteries undergo a spontaneous discharging state. The Nobel Prize in Chemistry 2019 - Popular information.

1.3 Motivation for the study

1.3.1   Seeking a promising solid electrolyte

To be used as a solid-state electrolyte (SSE), the material needs to possess high ionic conductivity at room temperature, negligible electronic conductivity, excellent electrochemical stability with both electrodes, especially with Li metal, environmentally benign, low cost, and

easiness of preparation[11]. **Figure 4** compared the ionic conductivity of some well-known SSEs at different temperatures along with the organic liquid electrolytes (1M solutions of $LiPF_6$ dissolved in 1:1 volume EC: PC), which is the goal of SSEs[12-19]. It can be seen that none of these Li-ion conductors can provide both high ionic conductivity and a wide electrochemical window. Even though the LGPS exhibits remarkably high ionic conductivity, it has a very limited electrochemical stability window from 1.7 to 2.1 V, as shown in **Figure 4**b[20]. Overall, Li garnet oxides are believed to be a promising candidate for solid electrolytes because of their relatively high ionic conductivity and good electrochemical stability.
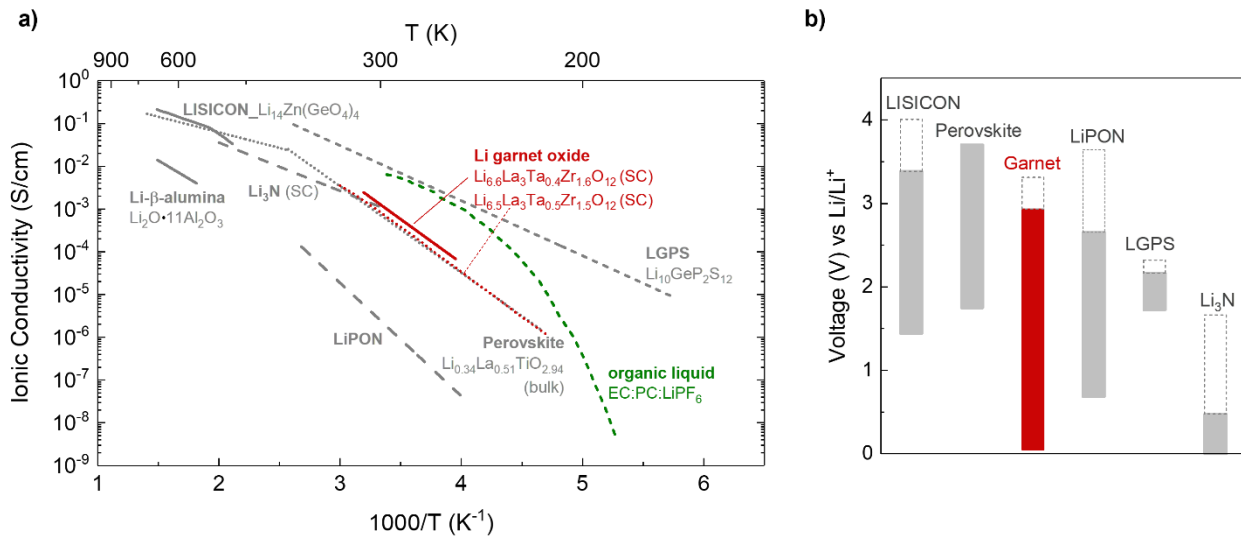
Figure 4 (a) Ionic conductivity as a function of the temperature of a few important solid-state electrolytes from literatures[12-19, 21]. The organic liquid electrolyte is shown for comparison. SC: single crystal. (b) the electrochemical window of a few solid electrolytes, the oxidation potential to fully delithiate the material is marked by the dashed lines. Edited from [20].

1.3.2   Experimental versus computational studies

First of all, experimental samples often contain impurities, for example, they could be Al-contaminated when alumina crucibles are used in the preparation process[22]. Secondly, lithium garnet oxide $Li_7La_3Zr_2O_{12}$ exhibits a tetragonal-cubic phase transition after being exposed to H_2O/CO_2 during material synthesis and characterization[23]. In addition, normally experimental

6

samples are added with an arbitrary amount of extra Li to compensate for the Li loss in the preparation process, i.e. usually inaccurate Li composition. On the other hand, computational studies have advantages over experiments as simulation materials are pure phases and without the complication of structure defects like grain boundaries.

1.3.3   Accuracy versus efficiency of different computational methods

A lot of computational methods have been used to study SSE. These methods generally fall into three categories, density-functional theory (DFT), semi-empirical (SE) and density-functional tight-binding (DFTB) potential, and empirical interatomic potential (IP). The relationship between these methods is shown in **Figure 5**[24].

Density-functional theory (DFT) is one of the most widely used computational tools for studying the properties of solid-state materials. It generates the energy, force, and stress of atoms and cells based on fundamental principles of quantum mechanics without any empirical parameters and therefore is the most accurate computational method. However, as seen in **Figure 5**, DFT is very slow at a time scale of ps and therefore is restricted to model systems containing typically hundreds of atoms. For example, running a molecular dynamics (MD) trajectory of 1-ps (e.g., 1000 calculations for a timestep of 1 fs) for a unit lithium garnet oxide cell with about 200 atoms takes about 15 hours, which means running a 1-ns (i.e., a common trajectory length using the IP method) would take 625 days[24]. Therefore, it is unrealistic to run DFT-based MD for big structures and at low temperatures. For example, lithium garnet oxide structures with grain boundaries (GBs), which will be discussed in Chapter 5, could contain more than ten thousand atoms. Since it usually needs to run much longer trajectories to capture the property information at low temperatures due to the slow mobility of atoms, DFT has been widely used in studying the self-diffusivity and ionic conductivity at high temperatures and then extrapolating the room temperature values according

7

to the Arrhenius relationship. However, this methodology could be inaccurate. For example, Miara et al.[25] performed a DFT-MD simulation for $Li_{6.75}La_3Zr_{1.75}Ta_{0.25}O_{12}$ at the temperature range of 600-1500 K and extrapolated the room temperature ionic conductivity of 1.2×10^{-2} S/cm, which is one order magnitude higher than the hot-pressing sample (0.87×10^{-3} S/cm)[26].

The second category includes the SE and DFTB. DFTB has several versions, e.g., self-consistent charge (SCC) DFTB (also referred to as DFTB2), which is an approximation method of the Kohn-Sham DFT method. It has less accuracy but 2 orders of magnitude faster compared to the standard DFT. xTB[27] and PM6[28], the variants of DFTB and SE, respectively, have similar or even worse force/virial accuracy than the Core model[24]. Besides, the computational cost of this group is still very high[24].

The third group is IP models, including physically motivated models such as Core, core-shell (CS), induced dipole (ID) and fluctuating charge, and pure mathematic machine-learning interatomic potential (MLIP) models. Compared to DFT and DFTB, IP methods are faster but less accurate. In recent years, a lot of efforts have been devoted to developing accurate IP models. In particular, MLIP has become an increasingly popular tool in the study of materials science.
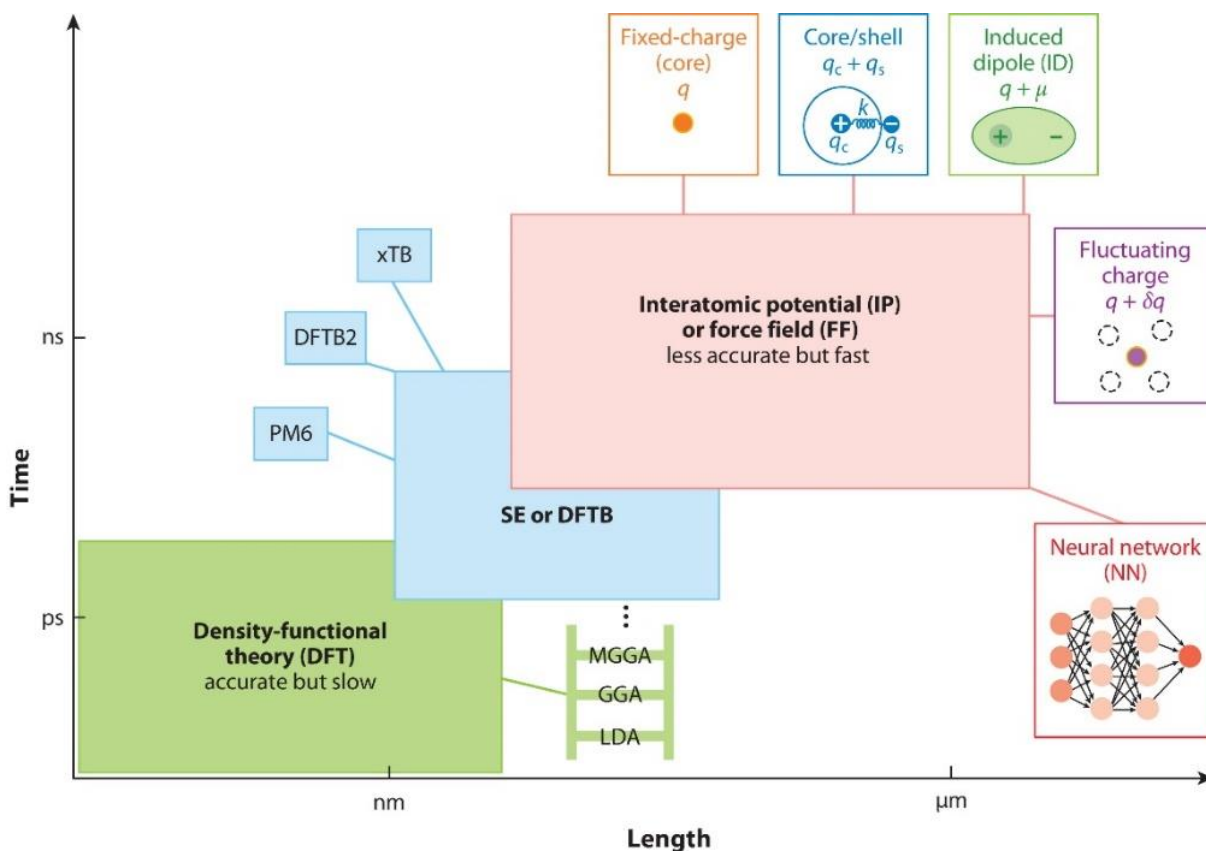
Figure 5 Schematic of different computational methods based on their length and time scales[24].

1.4 Thesis overview

With the introduction and motivation discussed above, this thesis is organized into the following five chapters.

Chapter 2 provides the background of several inorganic solid electrolytes, the structure of lithium garnet oxides, computational methods applied in this work, and methods for property calculations of lithium garnet oxides. In Chapter 3, we compared MD simulation results of $Li_7La_3Zr_2O_{12}$ from three IP models, i.e., Core, CS, and ID, including the lattice parameters, self-diffusivity, jump length, residence time, ionic conductivity, dielectric constant, and elastic modulus. In Chapter 4, we constructed new potentials of DFTB and MLIP models and compared them with the IP models through force error, lattice parameter, and radial distribution function by

performing MD simulations of $Li_6La_3TaZrO_{12}$. It turns out that the MLIP model approaches the DFT accuracy and matches the ionic conductivity of literature-reported experimental values. Then we used the MLIP model to study the transport of lithium garnet oxide series $Li_xLa_3Zr_{x-5}Ta_{7-x}O_{12}$ (x=5-7) and solve the problem of what composition gives the highest ionic conductivity. In Chapter 5, we used the MLIP model to study the GB contribution to the ionic conductivity of lithium garnet oxide $Li_7La_3Zr_2O_{12}$. In Chapter 6, we summarized the present work and discussed the future direction.

CHAPTER 2 Background

2.1 Inorganic solid-state electrolytes

During the last few decades, a wide variety of inorganic materials have been explored and studied to be used as possible solid-state electrolytes (SSEs) in all-solid-state Li-ion batteries (ASSLiB)[11, 29-33]. Among them, Li-β-alumina, Li_3N, lithium superionic conductor (LISICON), amorphous lithium phosphorus oxynitride (LiPON), perovskite-type oxides, Li garnet-type oxides, and $Li_{10}GeP_2S_{12}$ (LGPS) have attracted a great deal of attention. Some of the crystal structures are shown in **Figure 6**.
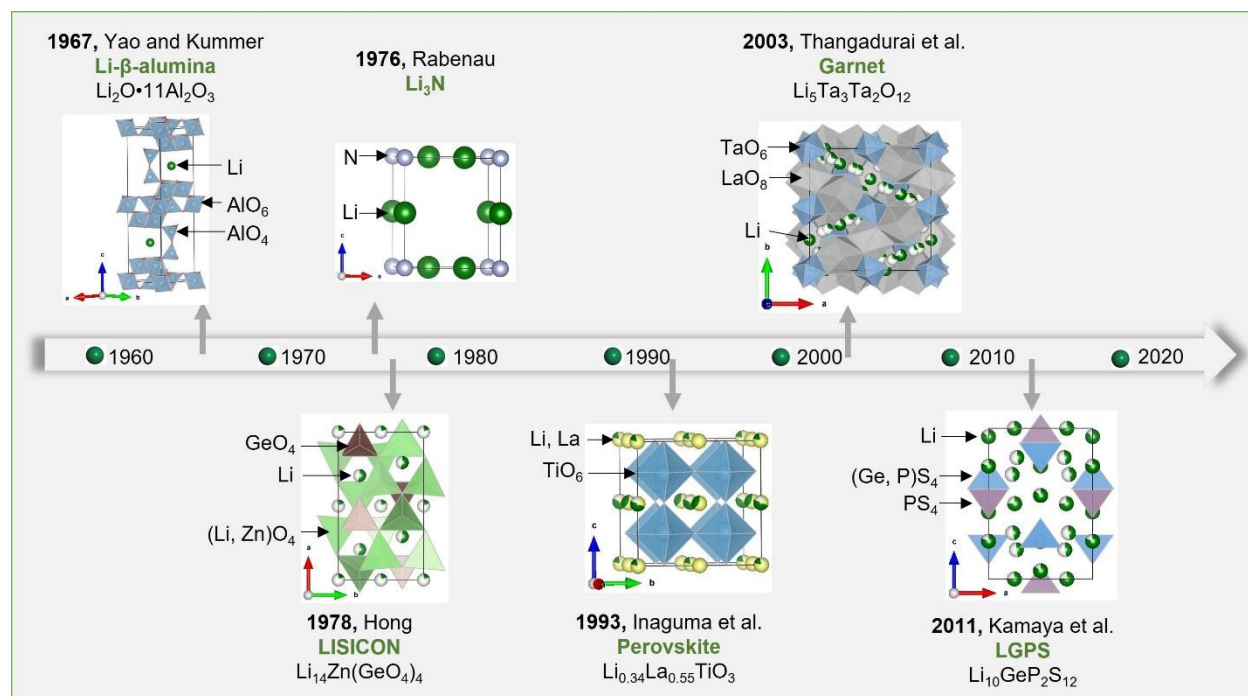
Figure 6 Historical developments of Li-ion solid electrolytes.

2.1.1 Li-β-alumina

In 1967, Yao and Kummer first discovered β-alumina, which has the empirical formula $Na_2O\bullet11Al_2O_3$. It is a hexagonal structure with the lattice parameter of a=5.58 and c=22.45 Å. The

self-diffusivity of Na^+ at 25 °C and 300 °C are 4.0×10^{-7} and 1.0×10^{-5} cm^2/s, respectively[34]. They also synthesized Li-β-alumina by exchanging cation Na^+ with Li^+, which shows an expansion in the lattice (a=5.593 and c=22.642 Å) despite the smaller size of Li^+ with the ionic conductivity of one to two orders of magnitude lower[34]. However, it is difficult to prepare a pure phase.

2.1.2 Li_3N

Li_3N crystal is a hexagonal structure with space group P6/mmm (a=3.648 and c=3.875 Å)[35]. It consists of Li_2N layers perpendicular to the c axis and connected by Li atoms occupying the sites between the respective N atoms. Li_3N attracted high interest owing to its high Li content and its layered structure building up of sequential Li_2N and Li layers. The ionic conductivity of a single crystal at 300 K is 1.2×10^{-3} S/cm perpendicular to the c-axis and 1.0×10^{-5} S/cm along the c-axis, with an activation energy of 0.29 and 0.49 eV, respectively[18]. However, its low thermodynamic decomposition potential (0.44 V) and sensitivity to moisture limit its use as a solid electrolyte[36].

2.1.3 LISICON and thio-LISICON

LISICON was first proposed by Hong in 1978 for a new Li-ion superionic conductor $Li_{14}Zn(GeO_4)_4$ [14], which is a member of $Li_{16-2x}Zn_x(GeO_4)_4$ ($0.5 \leqslant x \leqslant 3.5$) series. It is an orthorhombic structure with space group Pnma (a=10.828, b=6.251, c=5.140 Å). The structure has a rigid 3D network of $Li_{11}Zn(GeO_4)_4$, in which Li, Ge, and Zn are located in tetrahedral sites, and the remaining Li^+ occupy octahedra sites. The Li^+ diffusion pathway is formed through the tetrahedral and interstitial octahedral sites. It has an ionic conductivity of 0.13 S/cm at 300 °C. Then, in 2000, Kanno et al. synthesized a family of thio-LISICON by replacing O^{2-} in LISICON

12

with S^{2-}[37], among which $Li_{4+x+\delta}(Ge_{1-\delta-x}Ga_x)S_4$ (x=0.25) exhibits the highest ionic conductivity that reaches up to 6.5×10^{-5} S/cm at ambient temperature.

2.1.4 LiPON

The amorphous lithium phosphorus oxynitride (LiPON) thin film was first studied by Bates et al. in 1992 and successfully incorporated into rechargeable thin-film lithium batteries[38]. LiPON was fabricated by sputtering Li_3PO_4 in N_2. Its composition can be represented by $xLi_2O\bullet yP_2O_5\bullet zPON$, where PON is phosphorous oxynitride. LiPON has a conductivity of $\sim2.3\times10^{-6}$ S/cm at 25 °C[16].

2.1.5 Perovskite-type

In 1993, Inaguma et al. first discovered cubic perovskite $Li_{0.34(1)}La_{0.51(1)}TiO_{2.94(2)}$ (a=3.871 Å) with the bulk and total ionic conductivity of 1×10^{-3} and 2×10^{-5} S/cm, respectively at room temperature[15]. The ideal perovskite has a formula of ABO_3, where A and B refer to twelve-coordinated and six-coordinated cations, respectively. It is a cubic structure with space group Pm-3m. The octahedral BO_6 occupies the corner of the cube, leaving the center for cation A and vacancies. The introduction of Li modifies the structure and vacancies and the ionic conductivity changes with Li concentration. However, the major disadvantage of perovskite is the facile reduction of Ti^{4+} into Ti^{3+} via a chemical reaction with low-potential anodes such as Li metal.

2.1.6 Garnet-type

In 2003, Thangadurai et al. first reported Li garnet oxides $Li_5La_3M_2O_{12}$ (M=Nb, Ta), both of which exhibit the same order of magnitude of bulk ionic conductivity of $\sim10^{-6}$ S/cm at 25 °C[39]. Since then, lithium garnet oxides have attracted extensive interest, and tremendous work has been devoted to studying the structure and properties of lithium garnet oxides. The details of the

13

structure will be introduced in section 2.2. The properties of the lithium garnet family $Li_xLa_3Zr_{x-5}Ta_{7-x}O_{12}$ (x=5-7) will be discussed in the following chapters using theoretical calculations.

2.1.7 LGPS

In 2011, Kamaya et al. synthesized a new lithium superionic conductor, $Li_{10}GeP_2S_{12}$ with a structure different from thio-LISICON[12]. It is a tetragonal phase with a lattice parameter of a=8.71771(5) and c=12.63452(10) Å. The Li ions move in one-dimensional z-axis and exhibit ionic conductivity of over 10^{-2} S/cm at 27 °C (as shown in **Figure 4**a), which is comparable to those of the commercial organic liquid electrolytes being used in LiBs. However, it is highly sensitive to moisture and is unstable against Li metal anodes.

2.2 Lithium garnet oxides

Li garnet oxides are based on garnets with the general structural formula, $A_3B_2(SiO_4)_3$ or $Si_3A_3B_2O_{12}$ (space group #230, Ia-3d), where A and B refer to eight-coordinated and six-coordinated cation sites, respectively (as shown in AO_8 dodecahedra and BO_6 octahedra in **Figure 7**a). Li garnet oxides replace Si in the garnets by Li. A large number of compounds have been found with the Li garnet structure, in which element A could be replaced by La, Nd, Ba, Sr, etc., and element B could be Ta, Zr, Nb, Te, etc.[24, 40]. In $Li_xA_3B_2O_{12}$, there are two kinds of polyhedra to accommodate Li atoms, i.e., LiO_6 octahedron (Oh) and LiO_4 tetrahedron (Td). Each LiO_4 Td is surrounded by four LiO_6 Oh and each LiO_6 Oh is linked by two LiO_4 Td. The Td and Oh are connected by a triangular oxygen face called the bottleneck for Li ion transport. There are 24 Td and 48 Oh in each cell and provides 72 sites for Li atoms in total. However, due to the exclusion principle, a cluster of Td-Oh-Td with three Li neighboring atoms does not exist, therefore the maximum concentration of Li per unit formula is 7.5 instead of 9 as there are 8 formulas in each unit cell.

Li garnet oxides have two types of phases, cubic phase (space group #230, Ia-30) and tetragonal phase (space group #142, $I4_1/acd$). Specifically, there are two special model materials for the cubic phase, endmember $Li_3Nd_3Te_2O_{12}$ (Li_3-phase) and intermediate member $Li_5La_3Ta_2O_{12}$ (Li_5-phase). In the Li_3-phase, Li atoms locate exclusively and fully in Td-24d sites, as shown in **Figure 7**e, in which the blue rectangle represents LiO_6 Oh, the pink squares represent LiO_4 Td, and the orange dots represent Li atoms. The absence of Li atoms in the neighboring Oh sites reduces the repulsion between Li atoms and thus leads to very low ionic conductivity of ~10^{-5} S/cm at 600 °C with high activation energy (> 1 eV)[41, 42]. As Li content increase, extra Li are incorporated into the Oh sites, and due to the electrostatic repulsion, not all Td/Oh sites can be occupied at the same time, resulting in Li atoms occupying both Td and Oh sites randomly (as shown in **Figure 7**f). For example, in the Li_5-phase, the occupancies of Td and Oh are 0.802(4) and 0.43(2), respectively[43]. Even though the average distance between Td-24d and Oh-48g sites is about 2 Å, the majority of the Li atoms are found in off-center Oh-96h sites due to strong repulsion between neighboring atoms, suggesting that Li atoms jump ~2.5 Å to the next site[44], as shown in **Figure 7**b. For the tetragonal phase, a typical model is the practical upper endmember $Li_7La_3Zr_2O_{12}$ (Li_7-phase) at room temperature (as shown in **Figure 7**c, d, g), which contains 7 Li per unit formula by replacing pentavalent Ta in Li_5-phase with tetravalent Zr. In the tetragonal phase, Td-24 sites are separated into Td-8a (dark pink) and Td-16e (light pink) sites and Oh-48g sites are separated into Oh-16f and Oh-32g sites. The tetragonal phase is an ordered structure, in which Td-8a, Oh-16f, and Oh-32g are fully occupied by Li atoms while Td-16e sites are fully empty. The complete ordering of Li-vacancies in a tetragonal structure leads to low ionic conductivity, which is about 2 orders of magnetic lower than that of the cubic phase[45]. However, when $Li_7La_3Zr_2O_{12}$ is exposed to the air, the Li-ordering can be disrupted by protons due to Li^+/H^+

exchange and induce the tetragonal-to-cubic phase transition[23]. Furthermore, $Li_7La_3Zr_2O_{12}$ undergoes an intrinsic phase transition when the temperature increase. It has been reported that the tetragonal-to-cubic phase transition occurs between 373 to 923 K depending on the purity of the sample[24].
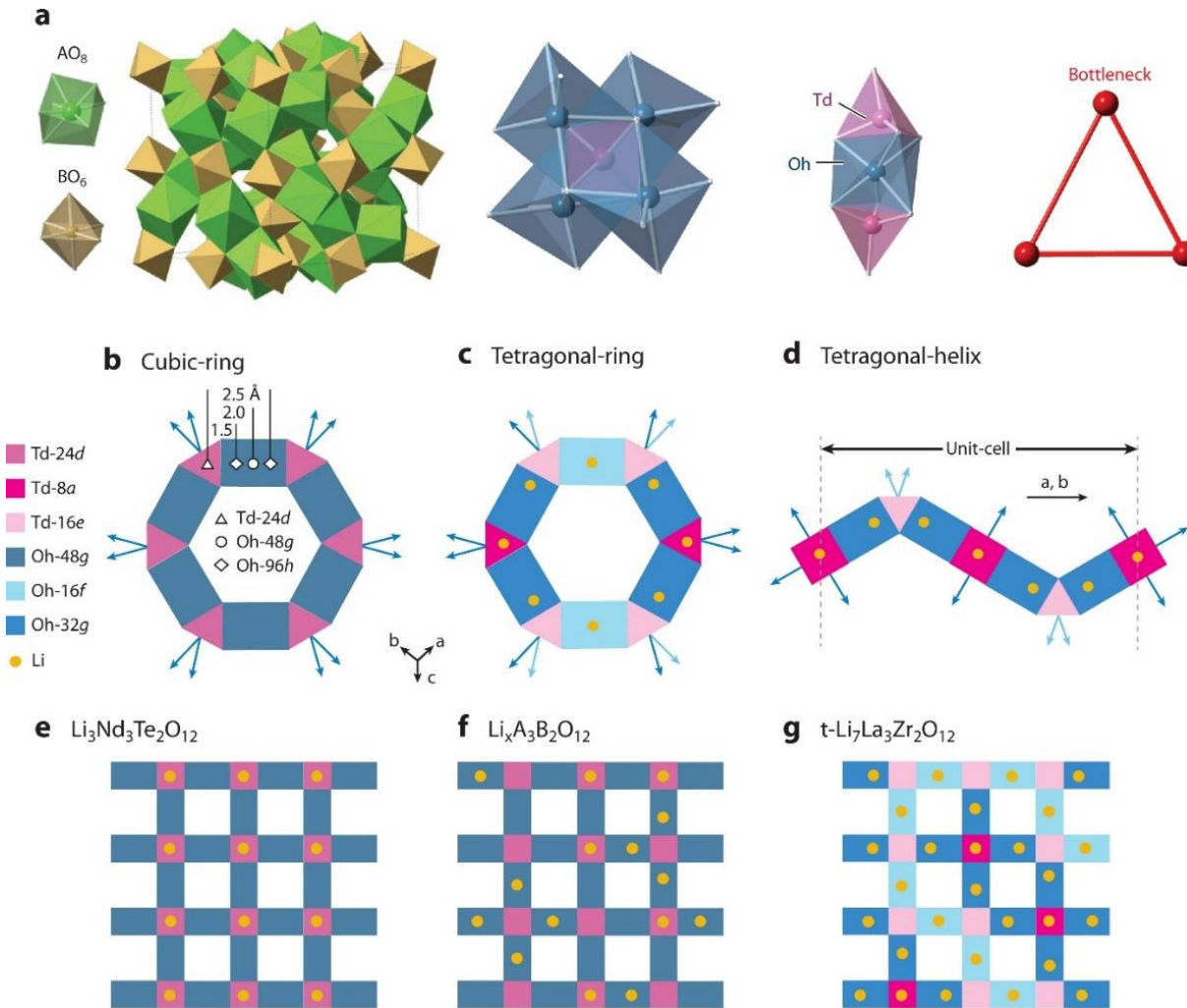
Figure 7 (a) 3D schematics of Li garnet oxide ($Li_xA_3B_2O_{12}$) structures. (b) and (c) 2D schematic of a polyhedral ring of cubic and tetragonal phase, respectively. (d) Characteristic of 8-member helix in a unit cell of tetragonal phase along the crystallographic a or b direction. (e-f) 2D schematic of two endmembers of Li garnet oxides $Li_3Nd_3Te_2O_{12}$, $Li_xA_3B_2O_{12}$ (3<x<7), and $Li_7La_3Zr_2O_{12}$ [24].

To stabilize the cubic phase and improve the ionic conductivity of lithium garnet oxides, multiple elements have been considered as aliovalent ion doping at Zr sites in $Li_7La_3Zr_2O_{12}$, such

as Ta[19, 27, 46-52], Al[26, 53-55], Ga[56-58], Nb[59], W[60, 61], and Mo[62, 63] and so on. This work will be focusing on studying the properties of Li garnet oxides series $Li_xLa_3Zr_{x-5}Ta_{7-x}O_{12}$ (x=5-7).

2.3 Computational methods and molecular dynamics simulation

2.3.1 Density functional theory

Density functional theory (DFT) was developed by Kohn and Sham in the 1960s[64, 65]. It transforms the interacting many-electron system into a non-interacting single-electron system by replacing the complex many-electron wave function with the electron density. The Kohn-Sham total energy with respect to electron density can be expressed as

$$E[n(\boldsymbol{r})] = T + E_{ext} + E_H + E_{xc} + E_{II}$$

where T is the non-interacting kinetic energy, E_{ext} is the external electron-ion interaction, E_H is the Hartree energy, E_{xc} is the exchange-correlation (XC) energy, and E_{II} is the ion-ion interaction. $n(\boldsymbol{r})$ is the electronic density given by

$$n(\boldsymbol{r}) = \sum_\alpha |\psi_\alpha(\boldsymbol{r})|^2$$

where $\psi_\alpha(\boldsymbol{r})$ is the wave function of the electronic state α. Now the energy can be rewritten in order as

$$E[n(\boldsymbol{r})] = \sum_\alpha f_\alpha \langle\psi_\alpha| \left(-\frac{1}{2}\nabla^2 + V_{ext} + \frac{1}{2}V_H + V_{xc}\right)|\psi_\alpha\rangle + E_{II}$$

where f_α is the occupation of a single-particle state ψ_α, $V_H(\boldsymbol{r}) = \int \frac{n(\boldsymbol{r}')}{|\boldsymbol{r}-\boldsymbol{r}'|}d^3r'$, $V_{xc}(\boldsymbol{r}) = \frac{\delta E_{xc}[n(\boldsymbol{r})]}{\delta n(\boldsymbol{r})}$. The only unknown part is E_{xc}, which can be approximated by functionals, such as local density approximation (LDA)[65], generalized gradient approximation (GGA)[66], and meta-generalized GGA (MGGA)[67]. LDA approximates the XC energy density at a local position by the value of

a uniform electron gas with the same electron density, GGA includes the electron density gradient and MGGA includes the Laplacian of the electron density. The most commonly used GGA type in solid-state calculation is Perdew-Burke-Ernzerh (PBE)[68, 69].

2.3.2 Density-Functional Tight-Binding Potential

The simulation methods next to DFT are semiempirical (SE) potentials like parameterization method 6 (PM6) and density-functional tight-binding (DFTB) potentials like extended tight-binding (xTB) and self-consistent charge DFTB (SCC-DFTB or DFTB2). DFTB is based on a second-order expansion of the Kohn-Sham total energy in DFT with respect to electronic density fluctuation [70-72]. By expanding $E[n(\boldsymbol{r})]$ at $n_0(\boldsymbol{r})$ up to second order in fluctuation $\delta n(\boldsymbol{r})$, and for brevity, $n(\boldsymbol{r}) \to n$, $n(\boldsymbol{r}') \to n'$, $n_0(\boldsymbol{r}) \to n_0$, $n_0(\boldsymbol{r}') \to n_0'$, $\int d^3\boldsymbol{r} \to \int$, and $\int d^3\boldsymbol{r}' \to \int'$, the energy reads as following:

$$E[n_0 + \delta n] = \sum_\alpha f_\alpha \langle \psi_\alpha | \left(-\frac{1}{2}\nabla^2 + V_{ext} + V_H[n_0] + V_{xc}[n_0] \right) | \psi_\alpha \rangle$$

$$+ \frac{1}{2} \iint \left(\frac{1}{|\boldsymbol{r} - \boldsymbol{r}'|} + \frac{\delta^2 E_{xc}}{\delta n \delta n'} |_{n_0} \right) \delta n \delta n'$$

$$- \frac{1}{2} \iint \frac{n_0 n_0'}{|\boldsymbol{r} - \boldsymbol{r}'|} + E_{xc}[n_0] - \int V_{xc}[n_0] n_0 + E_{II}$$

Note that linear terms in δn cancel each other. The first line is the band-structure energy (E_{bs}), the second line is the energy from the density fluctuations (E_{2nd}), and the third line including the 'double-counting' terms and the ion-ion repulsion (E_{II}) is called short-range repulsive energy (E_{rep}). Therefore, the total energy has the form of:

$$E_{tot}[n_0 + \delta n] = E_{bs}[n_0] + E_{2nd}[n_0, \delta n^2] + E_{rep}[n_0]$$

From here, DFTB requires the introduction of several approximations. First, band structure term, using the Hamiltonian operator $\widehat{H}[n_0]$ instead, becomes:

$$E_{bs} = \sum_\alpha f_\alpha \langle \psi_\alpha | \hat{H}[n_0] | \psi_\alpha \rangle$$

The electronic eigenstates (ψ_α) are expanded into a linear combination of pseudo-atomic orbitals (φ_μ) with minimal local basis since electrons are assumed tightly bound.

$$\psi_\alpha = \sum_\mu c_\mu^\alpha \varphi_\mu$$

where φ_μ is determined by solving the modified Kohn-Sham equation:

$$[\hat{T} + V_{eff} + V_{conf}]\varphi_\mu = \varepsilon_\mu \varphi_\mu$$

Where $\hat{T}$ is the kinetic energy operator, V_{eff} is the effective potential of a neutral pseudo-atom, and V_{conf} is the confinement potential to enforce the compact basis of the atomic orbitals with the form [73]

$$V_{conf}(r) = \left(\frac{r}{r_0}\right)^2$$

where r_0 is the compression radius. Taking the atomic eigenvalues of the free atom as the diagonal elements of the Hamiltonian matrix and making a two-center approximation for non-diagonal elements yields [73]:

$$H_{\mu\nu}^0 = \begin{cases} \varepsilon_\mu^{neutral\ free\ atom} & if\ \mu = \nu \\ \langle \varphi_\mu^i | \hat{H}[n_0^i + n_0^j] | \varphi_\nu^j \rangle & if\ i \neq j \\ 0 & otherwise \end{cases}$$

where i and j are the indices of atoms on which the wave functions and potentials are centered. The $H_{\mu\nu}^0$ and the overlap matrix elements $S_{\mu\nu} = \langle \varphi_\mu | \varphi_\nu \rangle$ can be precalculated and tabulated in Slater-Koster parameter files with respect to the interatomic distance r_{ij}. This step saves computational costs and makes the simulation almost two orders faster than the standard DFT method.

The second term the charge-density fluctuations δn is a superposition of atomic contributions δn_α:

$$\delta n = \sum_\alpha \delta n_\alpha$$

which can be approximated by atomic charge fluctuations at atom α, $\Delta q_\alpha = q_\alpha - q_\alpha^0$. q_α is determined from Mulliken population analysis and q_α^0 is the number of electrons of the neutral atom α. Now the second term can be written as

$$E_{2nd} = \frac{1}{2} \sum_{\alpha\beta} \gamma_{\alpha\beta} \Delta q_\alpha \Delta q_\beta$$

for $\alpha \neq \beta$, $\gamma_{\alpha\beta}$ is determined from the Coulomb interaction between the induced charges Δq_α and Δq_α; for the on-site contribution, $\gamma_{\alpha\alpha}$ is determined by the second derivative of the total atom energy with respect to the occupation numbers of the highest occupied atomic orbital.

The third term repulsive energy is the difference between the total energy in DFT and the corresponding electronic energy derived from SCC-DFTB, it can be approximated as the sum of pair potentials:

$$E_{rep}[n_0] = \sum_{\alpha,\beta} U(r_{\alpha\beta})$$

where $U(r_{\alpha\beta})$ is represented by the analytical functions with spline form of the interatomic distance $r_{\alpha\beta}$:

$$U(\boldsymbol{r}_{\alpha\beta}) = \begin{cases} e^{-a_1 r_{\alpha\beta} + a_2} + a_3 & 0 \leq r_{\alpha\beta} \leq r_{exp} \\ \sum_i c_i (r_{cut} - r_{\alpha\beta})^i & r_{exp} \leq r_{\alpha\beta} \leq r_{cut} \\ 0 & r_{cut} \leq r_{\alpha\beta} \end{cases}$$

where the parameters a_i and c_i are fitted and tabulated in Slater-Koster parameter files.

2.3.3 Interatomic Potential

Interatomic potential (IP) or force field (FF) is a set of functions that define the interactions in the molecular/material system. Physically motivated IP consists of two parts: short-range repulsion between atoms and long-range electrostatic potentials. The widely used short-range interatomic potential functions like Buckingham and Morse were adopted in this work. They are functions of atomic pair distance with forms as the following:

$$U_{ij}^{Buckingham} = Ae^{-\frac{r_{ij}}{\rho}} - \frac{C}{r_{ij}{}^6}$$

$$U_{ij}^{Morse} = E_0 \left\{ \left[1 - e^{-k(r_{ij}-r_0)} \right]^2 - 1 \right\}$$

where r_{ij} is the distance between two interacting atoms i and j, and A, ρ, C, E_0, k, and r_0 are the potential parameters.

In terms of the electrostatic potentials, there are three forms have been used in this work, i.e., Core, core-shell (CS), and induced dipole (ID) models together with the fluctuating charge (FQ) model[74-76], the schematics of which are shown in **Figure 5**. The non-polarizable Core model is the simplest model that describes an atom as a single core with a fixed charge, and therefore only the short-range IP parameters are needed to be trained.

The CS and ID models considered the polarization effects, which makes them more accurate than the Core model. CS model, also known as the Drude oscillator model, describes the electronic polarization by treating an atom as a two-particle system: a charged core (q_c) and a charged shell (q_s), connected by a harmonic spring (k). The magnitude of q_c and q_s are fixed. The atomic polarizability of atom i, α_i, is related to q_s and k, with the form of $\alpha_i = q_s{}^2/k$. The harmonic force constant k and short-range IP parameters were fitted.

The ID model describes an atom as a point charge plus a dipole (induced electronic polarization). In the ID model, the long-range electrostatic potential includes point charge with point charge, charge with dipole, and dipole with dipole. The polarization potential is described by[77]:

$$U_{ij}^{pol} = \sum_i \frac{1}{2\alpha_i} |\boldsymbol{\mu}_i| + \sum_{ij} \left[\left(q_i \boldsymbol{\mu}_j^\alpha g_{ij}(\boldsymbol{r}_{ij}) - q_j \boldsymbol{\mu}_i^\alpha g_{ji}(\boldsymbol{r}_{ij}) \right) \boldsymbol{T}_{ij}^\alpha - \boldsymbol{\mu}_i^\alpha \boldsymbol{\mu}_j^\beta \boldsymbol{T}_{ij}^{\alpha\beta} \right]$$

where α_i is the isotropic point polarizability of atom i, $\boldsymbol{\mu}_i$ the induced dipole moment at the ith site, which is treated as additional degrees of freedom and obtained at each MD step by minimizing the polarization energy. $\boldsymbol{T}_{ij}$ is the dipole-dipole interaction tensor. The short-range correction to atom i and atom j was in the form of Tang-Toennies damping function as [77, 78]

$$g_{ij}(\boldsymbol{r}_{ij}) = 1 - c_{ij} e^{-b_{ij} r_{ij}} \sum_{k=0}^{4} \frac{(b_{ij} r_{ij})^k}{k!}$$

In contrast to the IP models discussed above that with fixed charges, in the FQ model, the point charge is allowed to fluctuate and transfer between the atoms in response to the environment until the electronegativity becomes equalized.

2.3.4 Machine Learning Interatomic Potential

Unlike the traditional empirical IP models, machine learning interatomic potential (MLIP) does not use physically motivated functional forms, instead, it is built upon a purely mathematic technique. **Figure 8**a illustrated the high-dimensional neural network (HDNN) [79]. For a training system with N atoms, each line represents one atom with the atomic coordinates $\boldsymbol{R}_i$. First, the coordinates of each atom ($\boldsymbol{R}_i$) has to be transformed to a local atomic environment vector (AEV, also called descriptor $\boldsymbol{G}_i$), note that this step depends on the coordinates of all the atoms in the local environment, as shown in the dotted arrows. There are two categories of the descriptor, global

and local descriptors. Global descriptors predict the properties of the structure as a whole, like molecular energies and formation energies, including the coulomb matrix[80], the Ewald sum matrix[81], the sine matrix[81], and so on. Local descriptors predict localized properties, like atomic forces, including Atom-centered Symmetry functions (ACSFs)[79] and the Smooth Overlap of Atomic Positions (SOAP)[82]. Second, the descriptor $\boldsymbol{G}_i$ is transformed into atomic energy (E_i) through an element-dependent feed-forward neural network (NN), the details of which are illustrated in **Figure 8**b. Last, atomic energy (E_i) compromise the total energy of the system through:

$$E = \sum_i^N E_i$$
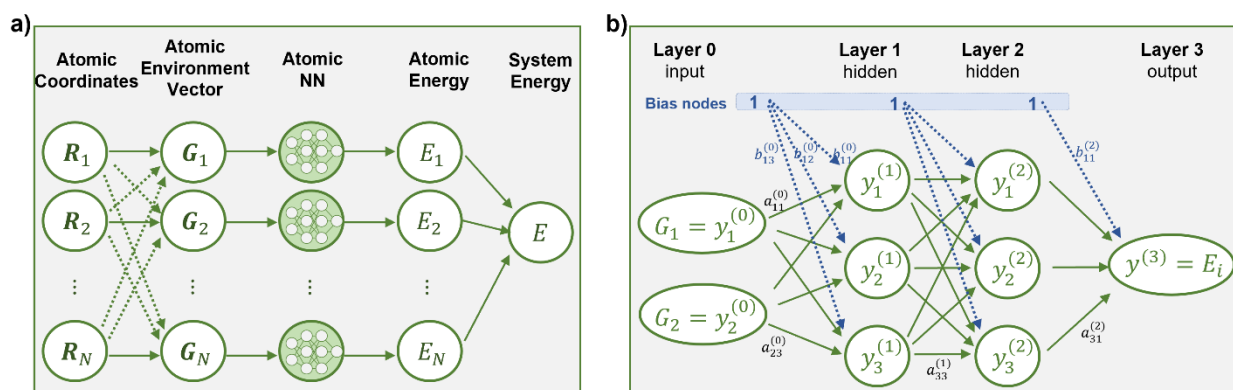
Figure 8 (a) Structure of a high-dimensional neural network, edited from the literature [79]. (b) Schematic illustration of a 2-3-3-1 neural network architecture. Green arrows represent the $a_{ij}^{(k)}$ in the weight matrix $\boldsymbol{a}^{(k)}$, i and j are the nodes in neighboring layer. The blue arrows represent the bias weight parameter $b_{ij}^{(k)}$ in the bias weight matrix $\boldsymbol{b}^{(k)}$[83].

In this work, the local descriptor ACSFs have been adopted. It is a description of the environment around the interested atom, hence only the local environment within the cutoff distance, R_c, is considered. The cutoff function is described as follows:

$$f_c(R_{ij}) = \begin{cases} 0.5 \cdot [\cos\left(\dfrac{\pi R_{ij}}{R_c}\right) + 1], & for\ R_{ij} \leq R_c \\ 0, & for\ R_{ij} > R_c \end{cases}$$

where R_{ij} is the distance between atoms i and j. The ACSFs in this work include the radial and angular functions with forms:

$$G_i^{radial} = \sum_j e^{-\eta(R_{ij}-R_s)^2} \cdot f_c(R_{ij})$$

$$G_i^{angular} = 2^{1-\xi} \sum_{j,k \neq i}^{all} (1 + \lambda\cos\theta_{ijk})^\xi \cdot e^{-\eta\left(R_{ij}^2 + R_{ik}^2 + R_{jk}^2\right)} \cdot f_c(R_{ij}) \cdot f_c(R_{ik}) \cdot f_c(R_{jk})$$

The radial function is a two-body potential, as a summation of Gaussian multiplied by the cutoff function. The parameters η and R_s determine the width and center shift of the Gaussian functions. In this work, η has eight values (listed in **Table 1**) and R_s was set to 0, hence there are eight radial SFs for each pair.

Table 1 Radial function parameters[84].

GNo.	η (Å^{-2})
1	0.003214
2	0.035711
3	0.071421
4	0.124987
5	0.214264
6	0.357106
7	0.714213
8	1.428426

The angular function is a three-body potential, a summation of the cosine function of the angle θ_{ijk} centered at atom i multiplied by three cutoff functions. The parameter η represents the distance from the central atom, the parameter ξ describes the angular resolution, and the parameter

λ shifts the maxima of the cosine function to $\theta_{ijk} = 0°$ and $\theta_{ijk} = 180°$. The parameter values are listed in **Table 2**, the combination of the three parameters yields 18 angular SFs for each triplet.

Table 2 Angular function parameters[84].

η (Å^{-2})	ξ	λ
0.000357	1	+1
0.028569	2	-1
0.089277	4	

Figure 8b is an architecture of a 2-3-3-1 neural network [83], which shows how NN describes the potential energy surface (PES) of each atom. There are four layers, which are the left input layer, the right output layer, and in between two hidden layers. The three nodes in each hidden layer have no physical meaning. The value of node i in layer k is noted as $y_i^{(k)}$ (i starts from 1 and k starts from 0). Therefore, the input $\boldsymbol{G} = (G_1, G_2)^T$ corresponds to $\boldsymbol{y}^{(0)} = \left(y_1^{(0)}, y_2^{(0)}\right)^T$, which are used to compute the first hidden layer values $\boldsymbol{y}^{(1)} = \left(y_1^{(1)}, y_2^{(1)}, y_3^{(1)}\right)^T$ and thereafter the second hidden layer values $\boldsymbol{y}^{(2)} = \left(y_1^{(2)}, y_2^{(2)}, y_3^{(2)}\right)^T$, in the end, output the energy, E. The vector of $\boldsymbol{y}^{(k)}$ ($k \geq 1$) are calculated through the intermediate vector $\boldsymbol{x}^{(k)}$,

$$\boldsymbol{x}^{(k)} = \left(\boldsymbol{a}^{(k-1)}\right)^T \boldsymbol{y}^{(k)} + \left(\boldsymbol{b}^{(k-1)}\right)^T$$

where $\boldsymbol{a}^{(k-1)}$ the weight matrix and $\boldsymbol{b}^{(k-1)}$ the bias weight matrix, the elements of which need to be optimized during the training process. And then the value $y_i^{(k)}$ is computed through

$$y_i^{(k)} = f^{(k)}\left(x_i^{(k)}\right)$$

where f is the activation function (also called transfer function) for the hidden layers, the effect of different activation functions will be discussed later in Chapter 4. For the output layer, a linear function is used.

25

2.3.5   Molecular dynamics simulation

Most of the work presented in this dissertation is the result of the molecular dynamics (MD) simulations. In classical MD, the atoms are treated as classical particles and the motions of the particles follow Newton's second law as in classical mechanics. The force is the derivative of the potential energy

$$\boldsymbol{F}_i = -\nabla U = m_i \frac{d^2 \boldsymbol{r}_i(t)}{dt^2}$$

where U is the potential energy, i represents the ith atom, and m_i, $\boldsymbol{F}_i$, and $\boldsymbol{r}_i$ are the mass, force, and coordinate of the ith atom at time t. Since $\boldsymbol{F}_i$ of each step can be calculated based on the coordinates and potential energy, the acceleration of each atom, $\boldsymbol{a}_i$, is $\boldsymbol{F}_i$ divided by m_i. With the initial assignment of coordinates and velocities, the coordinates of the first step with a short time Δt can be predicted. Combining the Verlet integration, the coordinates of the next step can always be predicted, and then the velocity can be calculated.

$$r(t + \Delta t) = r(t) + v(t)\Delta t + \frac{1}{2}a(t)\Delta t^2$$

$$v(t + \Delta t) = v(t) + \frac{a(t) + a(t + \Delta t)}{2}\Delta t$$

This process of calculating force, acceleration, coordinate, and velocity is repeated until the required steps are performed. Forces in classical MD simulations normally come from interatomic potentials. If the force comes from the electronic structure calculations based on quantum mechanics, the MD simulation is called ab initial MD (AIMD) or first principles MD (FPMD).

2.4 Training interatomic potentials

Potential parameters of IP models are obtained by fitting them to either experimental crystal structures or quantum mechanical training data. In this work, the potential parameters of Core and CS models were trained by fitting to lattice parameters and atomic positions of the

experimental structures in our previous work through the GULP package [85, 86]. Potential

parameters for the ID model were derived from the force-matching method[87, 88] which fits

interatomic potential forces to the first-principles forces of each atom. DFT-MD trajectories of

binary oxides Li_2O, ZrO_2, La_2O_3, and Ta_2O_5 together with the lithium garnet oxides were used

with the lattice parameters, atomic coordinates, and atomic forces included in the training, as

shown in **Figure 9**a. DFTB and MLIP models were trained from the DFT-MD trajectories of

lithium garnet oxides with energy, force, and cell-virial, see **Figure 9**b. The reliability of the

potential parameters was assessed by root mean squared error (RMSE) of atomic force and cell-

virial values from the trained potential against DFT.
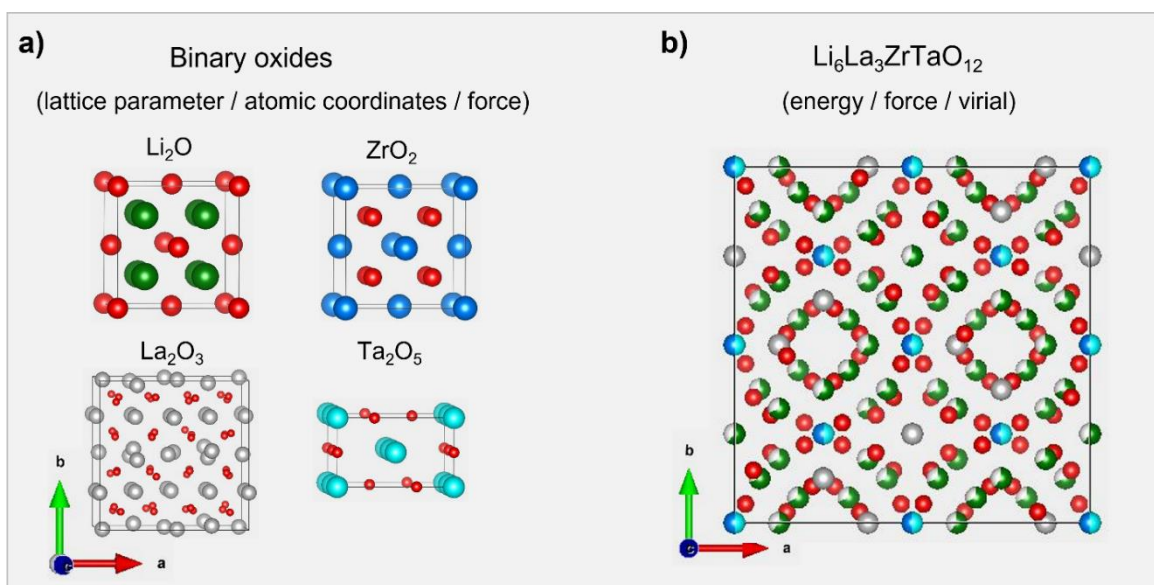
Figure 9 Structures of (a) binary oxides and (b) one member in lithium garnet oxide family $Li_6La_3ZrTaO_{12}$ used for performing DFT-MD to train ID model, DFTB, and MLIP models.

For the atomic charges, the average charge for each atom species of Core and ID models

was obtained using the Density Derived Electronic and Chemical (DDEC) approach [89-91], the

CS model used 80% of formal charge, the DFTB model used Mulliken atomic charge, and the

MLIP model is a mathematic model without charge. The details and values of potential parameters and atomic charges are listed in Chapters 3 and 4.

2.5 Methods for property calculations

2.5.1 Self-diffusivity

As MD simulations record the time evolution of atoms concerning coordinates and velocities, time correlation functions are important methods to extract the property information. There are two types of correlation functions. The first one is the incoherent (also called self-part) van Hove correlation function (VHCF), which is the probability density of finding a particle in the vicinity of r after traveling time t:

$$G_{inc}^{\alpha}(r, t) = \frac{1}{N_\alpha} \langle \sum_{i=1}^{N_\alpha} \delta[r + r_i^\alpha(0) - r_i^\alpha(t)] \rangle$$

where N_α the number of atoms of species α, and r_i^α is the position of ith atom of species α. The angle brackets represent the ensemble average.

The atomic diffusion was investigated by the spatial-Fourier transform of $G_{inc}^{\alpha}(r, t)$, called intermediate scattering function or incoherent density correlation function[92], which was calculated according to

$$F_{inc}^{\alpha}(k, t) = \langle \frac{1}{N_\alpha} \sum_{i=1}^{N_\alpha} e^{-ik \cdot r_i^\alpha(0)} e^{ik \cdot r_i^\alpha(t)} \rangle$$

where k is the wave vector of the simulation cell as

$$k_{n_x n_y n_z} = n_x a^* + n_y b^* + n_z c^*$$

where a^*, b^*, c^* are reciprocal unit vectors and n_x, n_y, and n_z are all integers. **Figure 10**a gives an example of the correlation time dependence of the function of a specific k. By fitting the curve with a (Kohlrausch-Williams-Watts) function[93]

$$I^{KWW}(k, t) = e^{-[\Gamma^{KWW}(k)]^{\beta(k)}}$$

where Γ^{KWW} is the relaxation rate and β is the stretching parameter conforming to $0 < \beta < 1$ [94]. $1 - \beta$ is called coupling parameter by Ngai[95], which depends on the intermolecular interaction. The mean relaxation rate, $\langle\Gamma\rangle$, was obtained from

$$\langle\Gamma\rangle = \frac{\Gamma^{KWW}(k)\beta}{G(\beta^{-1})}$$

where G is the Gamma function.

The k dependence of relaxation rate $\langle\Gamma\rangle$ is shown in **Figure 10**a. Two diffusion mechanisms can be used to analyze the Li-ion self-diffusivity. If Γ is linear dependence of k^2, it means that Li-ions diffuse continuously in the material and the Fickian diffusion model can be used to extract the self-diffusivity,

$$\Gamma(k) = Dk^2$$

where D is the self-diffusivity. Otherwise, the jump-diffusion models such as Chudley-Elliot (CE), Hall-Ross (HR), and Singwi-Sjolander (SS) models can be used to extrapolate the relation time, jump length, and self-diffusivity[96]. As shown in **Figure 10**a, the vertical arrows indicate vibrate and the horizontal arrows indicate diffuse/jump to the next site, the atoms (orange balls) vibrate for a residence time τ and then jump to the next site with jump length l. In this work, the SS jump-diffusion model[96, 97] was applied,

$$\Gamma^{SS}(k) = \frac{1}{\tau}\frac{k^2\langle l^2\rangle/6}{1 + k^2\langle l^2\rangle/6}$$

where τ is the residence time, $\langle l^2\rangle$ the mean square jump length square and the self-diffusivity can be calculated through

$$D = \langle l^2\rangle/(6\tau)$$
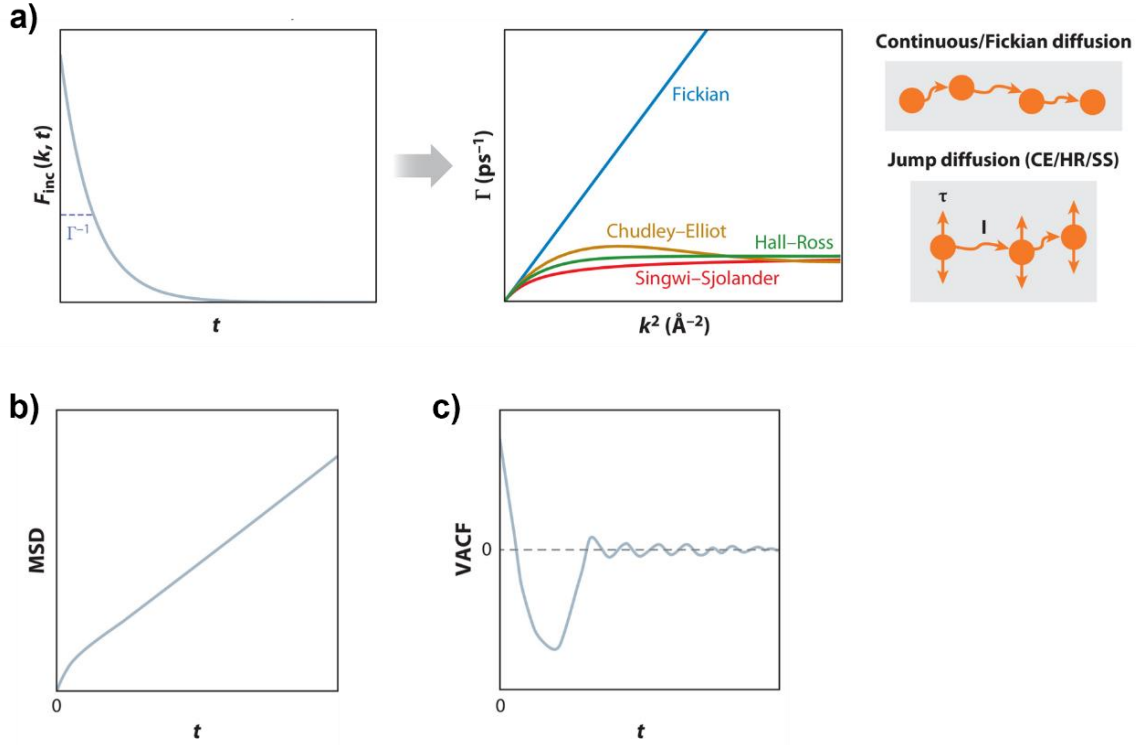
Figure 10 (a) Correlation time dependence of incoherent density correlation function. Relaxation rate as a function of k^2 and illustration of diffusion models. Correlation time dependence of (b) mean squared displacement (MSD) and (c) velocity autocorrelation function (VACF)[24].

The second group of the time correlation function is based on Einstein-Helfand (EH) formula[24, 92]

$$K_{EH} = \lim_{t \to \infty} \frac{1}{2t} \langle |A(t) - A(0)|^2 \rangle$$

where $A(t)$ could be incoherent or coherent versions of position or charge-weighted position. For example, the incoherent mean squared displacement (MSD) is the version of the position

$$\langle |\delta r_i^\alpha(t)|^2 \rangle = \frac{1}{N_\alpha} \sum_{i=1}^{N_\alpha} \langle |r_i^\alpha(t) - r_i^\alpha(0)|^2 \rangle$$

where N_α the number of atoms of species α, and r_i^α is the position of ith atom of species α. And therefore the self-diffusivity can be calculated from the slope of MSD vs. time plot as shown in **Figure 10**b

$$D = \lim_{t \to \infty} \frac{1}{6t} \langle |\delta \boldsymbol{r}_i^\alpha(t)|^2 \rangle$$

2.5.2   Ionic conductivity

Ionic conductivity is one of the most important properties of solid-state electrolytes. Here, we are introducing two methods, one is the coherent MSD of the charge-weighted EH equation[98]

$$\sigma = \frac{1}{3k_B TV} \lim_{t \to \infty} \frac{1}{2t} \langle \left(\sum_{i=1}^{N} z_i e r_i(t) - \sum_{i=1}^{N} z_i e r_i(0) \right)^2 \rangle$$

where k_B the Boltzmann constant, T the temperature, V the volume of the simulation cell, N the total number of atoms in the simulation cell, z_i and $\boldsymbol{r}_i$ the charge and coordinate of the ith atom, e the elementary electron charge, and t the time. This coherent ionic conductivity is directly related to experimental measurement.

The other method is based on the Green-Kubo (GK) formula

$$K_{GK} = \int_0^\infty \langle \dot{A}(0) \cdot \dot{A}(t) \rangle dt$$

which is mathematically equal to the K_{EH} formula[24]. **Figure 10**c illustrates the incoherent velocity autocorrelation function (VACF) as a GK formula, which yields the self-diffusivity of species α as

$$D = \frac{1}{3N_\alpha} \int_0^\infty \sum_{i=1}^{N_\alpha} \langle \boldsymbol{v}_i^\alpha(t) \cdot \boldsymbol{v}_i^\alpha(0) \rangle dt$$

where N_α the number of atoms of species α and $\boldsymbol{v}_i^\alpha$ is the velocity of the ith atom of species α. Similarly, the coherent charge current correlation function

$$\sigma = \frac{1}{3k_B TV} \int_0^\infty \langle \sum_{i=1}^{N} z_i e \boldsymbol{v}_i(t) \cdot \sum_{i=1}^{N} z_i e \boldsymbol{v}_i(0) \rangle dt$$

where N the number of total atoms in the simulation cell and $\boldsymbol{v}_i$ is the velocity of the ith atom. It can be separated into two parts: the longitudinal component

$$C^{L,c}(\boldsymbol{k},t) = \frac{e^2}{Vk_BT}\frac{1}{k^2}\langle(\boldsymbol{k}\cdot\boldsymbol{J}(\boldsymbol{k},0))(\boldsymbol{k}\cdot\boldsymbol{J}(-\boldsymbol{k},t))\rangle$$

and the transverse component

$$C^{T,c}(\boldsymbol{k},t) = \frac{e^2}{Vk_BT}\frac{1}{2k^2}\langle(\boldsymbol{k}\times\boldsymbol{J}(\boldsymbol{k},0))\cdot(\boldsymbol{k}\times\boldsymbol{J}(-\boldsymbol{k},t))\rangle$$

where

$$\boldsymbol{J}(\boldsymbol{k},t) = \sum_{i=1}^{N} z_i\boldsymbol{v}_i(t)e^{-i\boldsymbol{k}\cdot\boldsymbol{r}_i(t)}$$

is the collective charge current, e the elementary electron charge, V the volume of the simulation cell, k_B the Boltzmann constant, T the temperature, q_n and $\boldsymbol{v}_n$ are the charge and velocity of the nth atom, respectively. The coherent charge current correlation can be transformed to the frequency domain through the Fourier Transform (FT)

$$S^{L,T}(\boldsymbol{k},\omega) = \int_0^{\infty} C^{L,T}(\boldsymbol{k},t)e^{i\omega t}dt$$

where ω is the frequency. The ionic conductivity can be extrapolated at the long wavelength and zero frequency

$$\sigma = \lim_{\omega\to0} S_T(\boldsymbol{k},\omega)$$

Even though the ionic conductivity calculated through the GK formula is mathematically equivalent to that from the EH formula, it can be seen that GK starts with a strong oscillation and drop to 0 in a few picoseconds, which suggests that the MD trajectory should be saved more frequently to capture the oscillation features while eliminating or reducing the dependence of the saving frequency of integral.

In order to illustrate that the ionic motion is positively cooperated instead of uncorrelated, we also compared the coherent ionic conductivity with the Nernst-Einstein (NE) ionic conductivity that calculated from self-diffusivity

$$\sigma_{NE} = (z_{Li}e)^2 \frac{D_{Li}}{k_B T}(c_{Li})$$

where c_{Li} the lithium concentration. The ratio of σ_{NE} to σ is known as the Haven ratio:

$$H_R = \frac{\sigma_{NE}}{\sigma}$$

The Haven ratio is 1 for ideal solutions where the motion of ions is independent and uncorrelated.

2.5.3 Dielectric constant

Since the conductivity is related to dielectric function as

$$\omega\varepsilon_0\big[\varepsilon_{L,T}(\boldsymbol{k},\omega) - 1\big] = i\sigma_{L,T}(\boldsymbol{k},\omega)$$

where ε_0 is the vacuum permittivity, ω is the frequency, and $\varepsilon_{L,T}(\boldsymbol{k},\omega)$ is the dielectric constant. Therefore, the real part of the dielectric function can be obtained through the imaginary part of conductivity as

$$Re[\varepsilon_T(\boldsymbol{k},\omega) - 1] = -Im[\sigma_T(\boldsymbol{k},\omega)]/(\omega\varepsilon_0)$$

2.5.4 Elastic modulus

The elastic moduli were investigated by the momentum correlations that can be separated into the longitudinal and transverse components as

$$C^{L,m}(\boldsymbol{k},t) = \frac{1}{k^2}\langle(\boldsymbol{k}\cdot\boldsymbol{J}(\boldsymbol{k},0))(\boldsymbol{k}\cdot\boldsymbol{J}(-\boldsymbol{k},t))\rangle$$

$$C^{T,m}(\boldsymbol{k},t) = \frac{1}{2k^2}\langle(\boldsymbol{k}\times\boldsymbol{J}(\boldsymbol{k},0))\cdot(\boldsymbol{k}\times\boldsymbol{J}(-\boldsymbol{k},t))\rangle$$

where

$$J(\boldsymbol{k}, t) = \sum_{n=1}^{N} m_n \boldsymbol{v}_n e^{-i\boldsymbol{k}\cdot\boldsymbol{r}_n(t)}$$

is the collective momentum, m_n the atomic mass of the nth atom, $\boldsymbol{v}_n$ the velocity of the nth atom. The Fourier Transform (FT) of longitudinal and transverse forms are

$$S^{L,T}(\boldsymbol{k}, \omega) = \int_0^{\infty} C^{L,T}(\boldsymbol{k}, t) e^{i\omega t} dt$$

where ω is the frequency. **Figure 11** gives an example of the momentum correlations of both longitudinal and transverse components of $Li_7La_3Zr_2O_{12}$ using the induced dipole (ID) model at 1100 K.
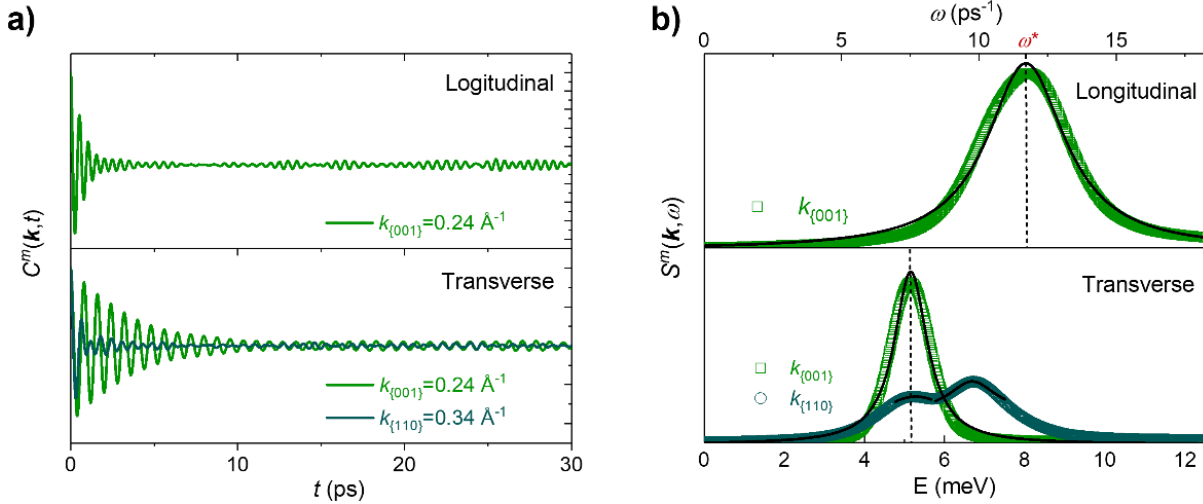
Figure 11 (a) Time domain and (b) frequency domain of momentum correlation function of the induced dipole (ID) model at 1100 K. Black lines are Lorentz fit to locate the peak position (dash lines).

We located the peaks (ω) of $S^{L,T}(\boldsymbol{k}, \omega)$ and assumed linear dispersion of ω on k to obtain longitudinal and transverse sound velocities v_L and v_T. For the cubic phase, the elastic constants C_{11}, C_{44} and C_{12} were calculated by the following formulas[99]:

$$(v_L^2 \rho)_{[100]} = C_{11}$$

$$(v_T^2 \rho)_{[001]} = C_{44}$$

$$(v_T^2 \rho)_{[110]} = \frac{1}{2}(C_{11} - C_{12})$$

Note that the $(v_T)_{[110]}$ was averaged from the two peaks. For the tetragonal phase, C_{11}, C_{44} and C_{12} were calculated in the same way as in the cubic phase, while C_{33} and C_{66} were calculated by the following formulas[99]:

$$(v_L^2 \rho)_{[001]} = C_{33}$$

$$(v_T^2 \rho)_{[100]} = C_{66}$$

We assumed that $C_{12} = C_{23}$ as they differ by only 2% from Deng et al[100]. The bulk and shear modulus were calculated according to [100]

$$B = \frac{1}{9}[(C_{11} + C_{22} + C_{33}) + 2(C_{12} + C_{23} + C_{31})]$$

$$G = \frac{1}{15}[(C_{11} + C_{22} + C_{33}) - (C_{12} + C_{23} + C_{31}) + 3(C_{44} + C_{55} + C_{66})]$$

In the cubic phase, $C_{11} = C_{22} = C_{33}$, $C_{12} = C_{23} = C_{31}$, and $C_{44} = C_{55} = C_{66}$. In the tetragonal phase, $C_{11} = C_{22}$, $C_{44} = C_{55}$, and $C_{23} = C_{31}$.

2.5.5 Grain boundary formation energy

Grain boundary (GB) formation energy, γ_{GB}, is the energy needed to form the grain boundary from the bulk material per unit area according to

$$\gamma_{GB} = \frac{1}{2A}(E_{GB} - nE_{bulk})$$

where A the area of GB plane, E_{GB} the total energy of the GB structure, n the number of a unit cell of the bulk material in the GB structure, and E_{bulk} is the energy of the unit cell of the bulk material.

CHAPTER 3 Model comparison

3.1 Motivation

As introduced in Chapter 2, $Li_7La_3Zr_2O_{12}$ (Li_7) is a special member of the lithium garnet family $Li_xLa_3Zr_{x-5}Ta_{7-x}O_{12}$ (x=5-7) due to the phase transition at high temperatures. Hence, it has been widely studied using interatomic potential (IP) models. For example, Adams et al.[101] performed MD simulation on Li_7 with the core model and Morse potential. Chen et al.[102] used the core model to study the diffusion characteristics of Li_7 based on the Buckingham potential. In the previous work of our group[85, 103], we used the core model to study the size effect on the MD simulation of Li_7 and used a polarizable core-shell (CS) model to study the local structure and dynamics of Li_7. Burbano et al.[104] used the polarizable induced dipole (ID) model to perform an MD simulation of Li_7 to study the mechanism of its low ionic conductivity. However, no work has been done to compare these models. In this chapter, we compared the accuracy of three models, i.e., Core, CS, and ID models in reproducing the phase transition, residence time, jump length, self-diffusivity, ionic conductivity, dielectric constant, and elastic moduli of fast ion conductor Li_7.

3.2 Computational details

3.2.1 Potential parameters

In the Core model, ionic interactions include the long-range Columbic potential and short-range Buckingham potential. The charges and potential parameters of the Core model were taken from our group's previous study[85]. CS model interactions include the long-range Columbic potential, short-range Buckingham and Morse potential, as well as the Dick-Overhauser core-shell polarizable potential for the O atom[105]. The harmonic spring constant between the oxygen core and shell is 19.64 eV $Å^{-2}$. The O shell (OS) mass was set to 0.2 a.u. The charges of each species were set as 80% of their formal charges.

In the ID model, we assigned the electronic polarizability to the O, La, and Zr species. Potential parameters were derived from the force-matching method. The force-matching was carried out using the FIST code as implemented in CP2K[106, 107]. The training set was from the first-principles MD simulations based on DFT, which were performed using the generalized gradient approximation (GGA-PBEsol)[108] and the projector augmented wave (PAW)[109] method as implemented in the Vienna Ab Initio Simulation Package (VASP)[110]. The unit cell was simulated using the NPT ensemble at 1200 K. The energy cutoff of 500 eV was used for the plane wave and the Brillouin zone was sampled at the Γ-point only. The production time was 3 ps with a time step of 1 fs. The trajectories after the first 0.15 ps were used to perform the force-matching. We extracted 190 configurations, i.e. one configuration every 15 fs. The obtained average structure was used for the subsequent static calculation. The average charge for each atom species was obtained using the Density Derived Electronic and Chemical (DDEC) approach [89-91]. The charge of each species and the potential parameters of the Core, CS, and ID model are listed in **Table 3**, **Table 4** and **Table 5**, respectively.

Table 3 Interatomic potential parameters for the Core model.

| Species | q (e) | Buckingham pair interaction with O | | |
		A (eV)	ρ (Å)	C (eV Å^6)
La	2.50	2075.26	0.326	23.25
Li	2.65	1087.29	0.260	0.00
O	1.00	4870.00	0.267	77.00
Zr	-1.65	1650.32	0.311	5.10

Table 4 Interatomic potential parameters for the CS model.

| Species | q (e) | Interaction pair | Buckingham potential | | | Morse potential | | |
			A (eV)	ρ (Å)	C (eV Å^6)	E_0 (eV)	k (Å^{-1})	r_0 (Å)
La	2.4	La-OS	1828	0.328	0	0.066	1.471	2.423
Zr	3.2	Zr-OS	2135	0.302	0	0.241	2.742	2.016
Li	0.8	Li-OS	370	0.291	0	0.081	0.870	1.937
O	-2.116	Li-Li	1470	0.239	0			
OS	0.516							

Table 5 Interatomic potential parameters for the ID model.

Species	q (e)	α (Å^3)	Ion-pair	b$_{ij}$ (Å^{-1})	c$_{ij}$ (Å^{-1})	A (eV)	ρ (Å)	C (eV Å^6)
			Polarization potential			Buckingham pair interaction with O		
La	2.54	1.71	La-O	3.344	2.315	2512.92	0.314	0
Zr	2.93	0.76	Zr-O	3.155	1.233	3034.17	0.282	0
Li	1	-	Li-O	3.772	1.729	507.79	0.298	0
O	-1.71	1.74						

3.2.2   Molecular Dynamics simulations

MD simulations were performed with the DL_POLY Classic package[111] for both Core and CS models, while for the ID model, it was carried out using the FIST code as implemented in CP2K[106, 107]. A 2×2×2 supercell of $Li_7La_3Zr_2O_{12}$ was used for all three models. There are 1536 atoms in the Core and ID model and 2304 atoms (including O shell) in the CS model.

For Core and CS modes, the velocity-Verlet integration was employed with a time step of 1 and 0.25 fs, respectively. The constant number, stress, and temperature (NσT) ensemble (Berendsen thermostat and barostat relaxation times were set to be 0.1 and 0.5 ps, respectively) simulations were performed for 75 ps and the last 35 ps were averaged to obtain the lattice parameters. The equilibration time of the constant number, volume, and energy (NVEe) ensemble was set to 100 ps with the atomic velocities rescaled every 0.1 ps. Subsequent NVE ensemble simulations were performed from 500 ps at high temperatures and to 70 ns in the case of low mobility of Li^+ in the tetragonal phase at 800 K.

For the ID model, the constant number, pressure, and temperature (NPT) ensemble was performed for 50 ps and the average lattice parameters were extracted from the last 40 ps. The Nose thermostat and barostat relaxation times were set to 0.05 and 0.25 ps, respectively. The NVE equilibrium (NVEe) process was 50 ps and the maximum accepted deviation of the temperature

38

from the desired target temperature was 50 K. The NVE process was set from 200 ps to 10 ns for different temperatures. The time step was 1fs for NPT, NVEe, and NVE process.

3.3 Results and discussion

3.3.1 Lattice parameters

First, we checked if all three IP models could reproduce the tetragonal to the cubic phase transition of Li_7 observed experimentally. A wide variety of transition temperatures were reported for Li_7 experimentally ranging from 373 to 923 K[23, 53, 112-114]. The difference could be resulting from the impurity/dopant (i.e., Al^{3+}) incorporation and/or H_2O or CO_2 exposure during material synthesis and characterization. For example, Matsuda et al.[53] found that the phase transition temperature of Li_7 decreases as the Al content increases and the reversible phase transition between the tetragonal phase and cubic phase occurs at 640 °C (913 K) for pure Li_7 without Al. Larraz et al.[115] reported that the presence of H_2O could induce the tetragonal to cubic phase transition due to the H^+/Li^+ exchange mechanism. On the other hand, undoped Li_7 not exposed to humidity at any moment undergoes a reversible tetragonal to cubic phase transition at about 645 °C (918 K). Given these observations, we only plotted the experimental values from Matsuda et al.[53] that applies to pure Li_7 in **Figure 12**, along with lattice parameters obtained from the Core, CS, and ID models. Lattice parameters of all three models increase with increasing temperature as expected in both tetragonal and cubic phases, with the phase transition occurring at about 900 to 1000 K. Both Core and ID models show thermal expansion and phase transition behaviors consistent with experiments while the CS model shows lower lattice parameters in a.
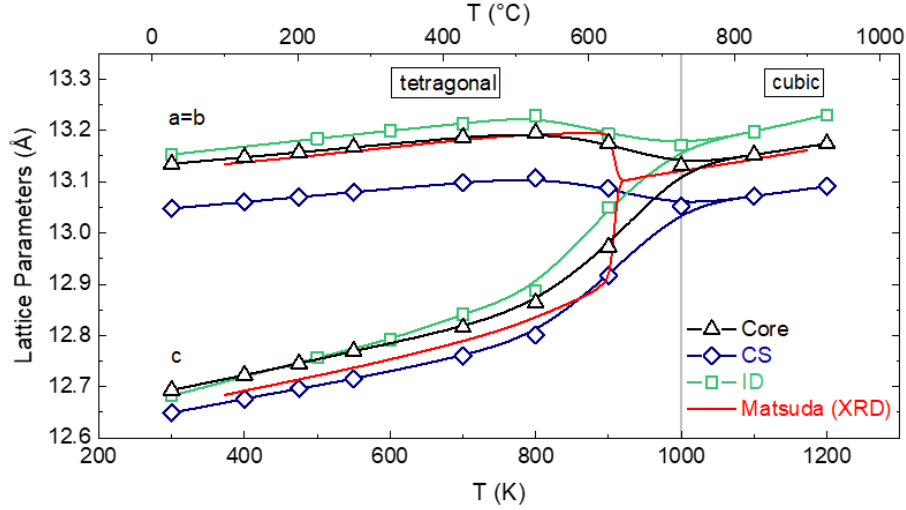
Figure 12 Lattice parameters from Core, CS, and ID models as a function of temperature. XRD experimental values from Matsuda et al. [33] are shown for comparison.

3.3.2 Self-diffusivity, jump length, and residence time

Next, we compared the long-range diffusion parameter, i.e., self-diffusivity, and short-range parameters such as jump length and residence time. **Figure 13** gives an example of the incoherent density correlation function of the ID model at 1100 K for selected k. It can be seen that for species La, Zr, and O, there is a rapid decrease in the ps range followed by a stable non-zero plateau, which suggests that these species only vibrate in their sites and provide a framework for Li atoms. In contrast, species Li exhibits an exponential decay from 1 to 0, especially faster at high k values, suggesting Li atoms diffuse in the structure. Ignoring data for the first 5 ps that undergo short-time dynamics, we fit the $I_{inc}^{\alpha}(k,t)$ curve of Li species using stretched exponential Kohlrausch-Williams-Watts function. **Figure 14** shows an example of the stretching parameters β and mean relaxation rate as a function of k^2 of ID model at 1100 K.

The behavior of β reveals that the Li transport in the material is a complex cooperative dynamic. As shown in **Figure 14**a, β decays from ~1 at small k values and converges at high k values. Similar behavior can also be found at all the other temperatures we studied. At small k

40

(longer distance), the interaction between any pair of atoms is weak so their motion is uncooperative or not coupled. At higher k (shorter distance), the interaction is cooperative or coupled. The plateau starts at k^2 ~2.0 Å^{-2}, corresponding to a cooperative length of ~4.4 Å, which is the approximate distance between octahedral sites across the tetrahedral site[44]. **Figure 14**b exhibits the fit of the Fickian diffusion model and Singwi-Sjolander (SS) jump-diffusion model to the MD data.
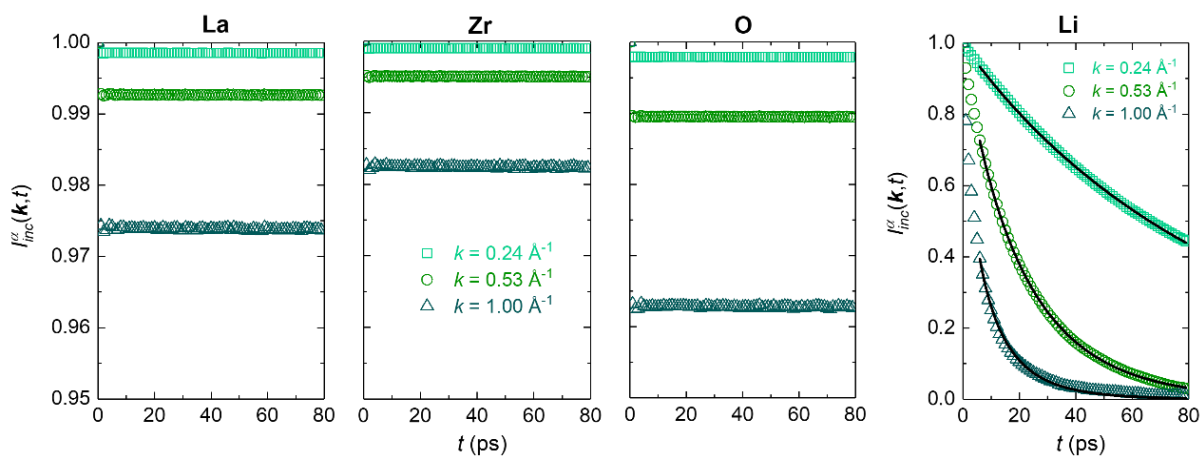

Figure 13 Incoherent density correlation function of species La, Zr, O, and Li for selected k values of the ID model at 1100 K.
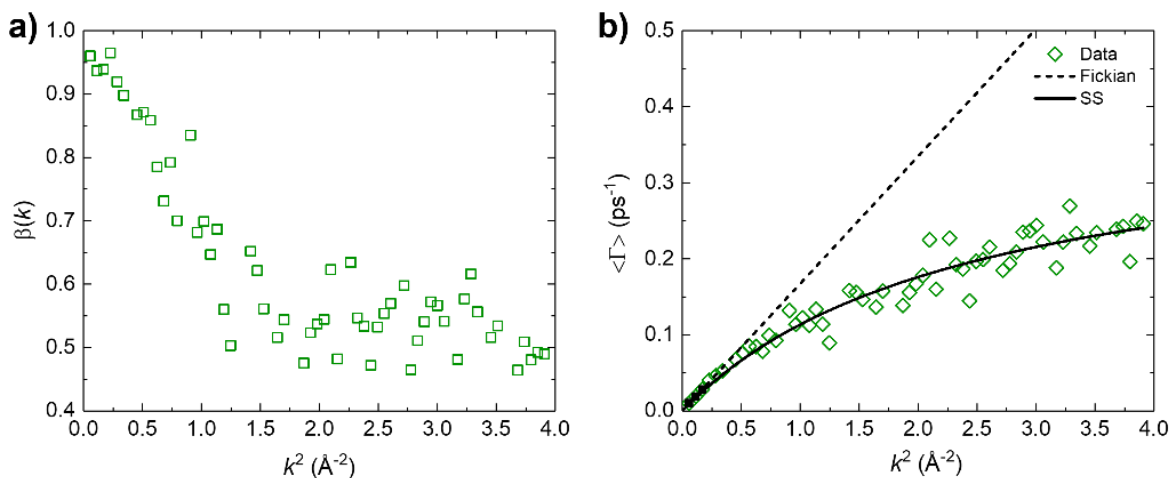

Figure 14 (a) The stretching parameter β and (b) the mean relaxation rate $\langle\Gamma\rangle$ as a function of k^2 of ID model at 1100 K.

The residence time (τ) and jump length (l) obtained from the SS model at different temperatures are shown in **Figure 15**. All Core, CS, and ID models show a sharp increase in residence time (**Figure 15**a) at the phase transition temperature. CS and ID models have close values in the cubic phase. Activation energies obtained from an Arrhenius fit for Core, CS, and ID models are 0.26, 0.26, and 0.31 eV, respectively. In the tetragonal phase, all three models show high activation energy values above 1.7 eV. The mean jump length (**Figure 15**b) obtained from Core, CS, and ID models at higher temperatures (cubic phase) are very close, i.e., 1.4~1.7 Å, which is roughly the distance between 24d (tetrahedral) and 48g (octahedral) sites in the cubic phase[103]. The jump length exhibits a significant increase at the phase transition temperature. In the tetragonal phase (800 K), the jump lengths for CS and ID models are about 2~2.5 Å, which is roughly the distance between 8a (tetrahedral) and 32g (octahedral) sites[45, 103].
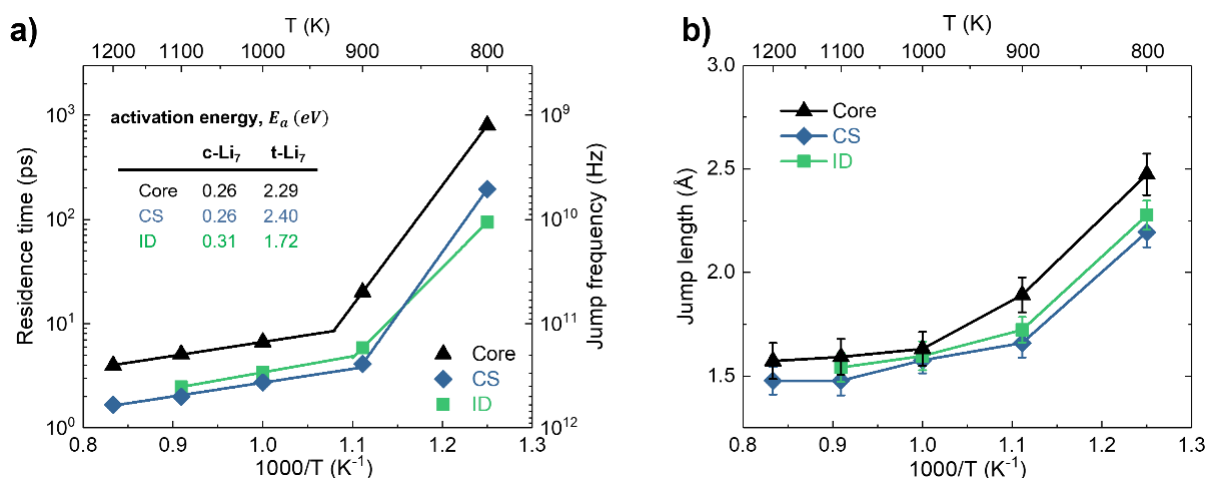

Figure 15 (a) Mean residence time (τ) of Li diffusion in LLZO obtained from Core, CS, and ID models in both cubic (c-Li$_7$) and tetragonal (t-Li$_7$) phases. Solid lines are an Arrhenius fit. (b) Mean jump length of Li diffusion obtained from Core, CS, and ID models.

Figure 16 compares Li-ion self-diffusivity in Li$_7$ of the Core, CS, and ID models along with other MD simulation results from the literatures. Our calculated values from the Core model are close to those from Jalem et al. using first-principles molecular dynamics (FPMD) simulation

with $1 \times 1 \times 1$ cell size[116], while values from the CS and ID models are a few times higher. The

activation energy of the Core model for the cubic phase is 0.24 eV, which is also close to that from

Jalem et al. at the temperature range of 873 to 1473 K, 0.26 eV. The activation energy of CS and

ID models for the cubic phase are 0.18 and 0.20 eV, respectively. The self-diffusivity obtained

from the CS model at high temperatures is close to that from Burbano et al. also using an ID model

but with a smaller activation energy of 0.14 eV[104]. The difference is likely to result from the

lower phase transition temperature of 623 K, as opposed to 900-1000 K, in their work.

Experimentally, the Li self-diffusivity at ambient temperature from Kuhn et al. using the spin-

lattice relation Nuclear Magnetic Resonance (NMR) measurement is on the order of 10^{-14}

cm^2/s[117]. Although our simulation was unable to calculate Li self-diffusivity at room

temperature, extrapolation of our data to the room temperature yields values on the order of 10^{-25}

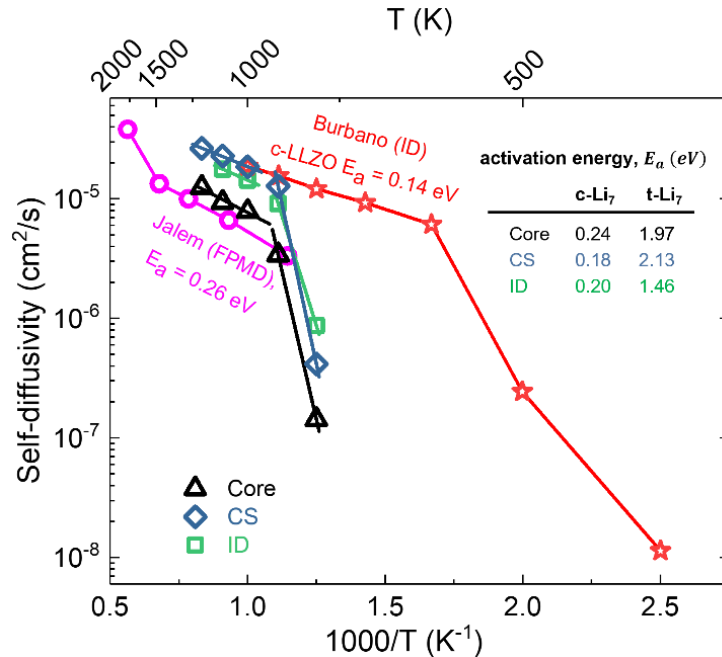$\sim 10^{-20}$ cm^2/s, which are much lower than the experimental result.

Figure 16 Self-diffusivity as a function of temperature for Core, CS, and ID models in both cubic (c-Li$_7$) and tetragonal (t-Li$_7$) phases. Solid lines are Arrhenius fit. The FPMD simulation data by Jalem et al.[116] and classic MD simulation data by Burbano et al.[104] are shown for comparison.

3.3.3 Ionic conductivity and dielectric constant

Figure 17a gives an example of the transverse component of coherent charge current density correlation function $C^{T,c}(\boldsymbol{k}, t)$ of the ID model at 1000 K for the three smallest k. It was found that the Fourier transform of the longitudinal component is a peak that goes to zero at zero frequency (not shown) but the transverse component, $S^T(\boldsymbol{k}, \omega)$ shown in **Figure 17**b, has a non-zero intercept suggesting that Li$_7$ is an ionic conducting material. The ionic conductivity was extrapolated from the transverse component. To manifest that $S^T(\boldsymbol{k}, \omega)$ is k independent, it is important to separate out all transverse outputs as shown in **Figure 17**c. The first number in the legend denotes the k value in Å^{-1} while the second and third series of three digits denote the k direction and its transverse direction. For example, the transverse polarization of vector [100] has two directions, i.e., [010] and [001]. It is apparent that the outputs of the two k vectors are similar to each other, which indicates that $S^T(\boldsymbol{k}, \omega)$ is independent of k vector. Thus, we averaged all six values of the first k vector and took the result of the smallest frequency as the ionic conductivity.
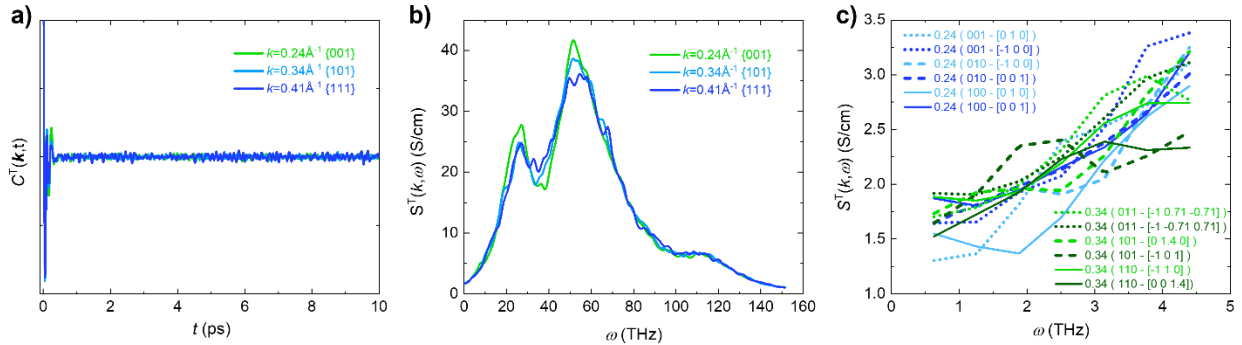

Figure 17 (a) Time and (b) frequency domain of the transverse coherent charge current density correlation function for the first three k values of the ID model at 1000 K. (c) All transverse outputs for first two k vectors at low frequencies.

Figure 18 compares the ionic conductivities of Core, CS, and ID models at different temperatures along with the experimental results from the literatures. It is obvious that all three models have a kink at about 900 K corresponding to the phase transition temperature. The

44

experimental measured ionic conductivities from Wang et al.[23] and Matsui et al.[118] also exhibit a sharp decrease at phase transition temperature between 600 °C (873 K) and 650 °C (925 K). Activation energies of the cubic phase for Core, CS, and ID models, i.e., Core-c, CS-c, ID-c, are 0.28, 0.13, and 0.17 eV, respectively, while values from Wang et al.[23] and Matsui et al.[118] are 0.13 and 0.12 eV, respectively. For the tetragonal phase, our simulations are unable to reliably calculate the ionic conductivities at lower temperatures due to the low Li$^+$ mobility. A simple extrapolation of our data will yield lower values than those from Wang et al.[23], Matsui et al.[118], and J. Awaka et al.[45].
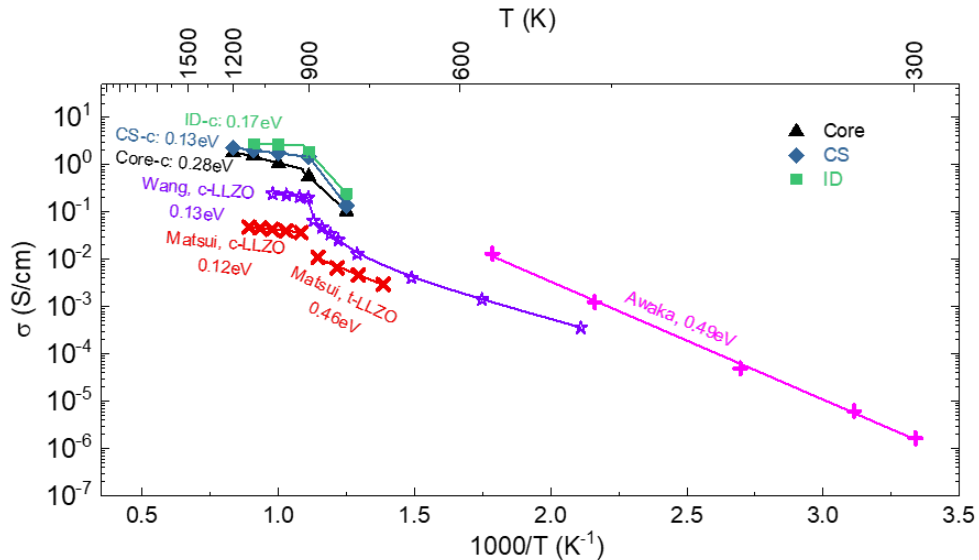

Figure 18 Ionic conductivity as a function of temperature for Core, CS, and ID models. Literature data from experimental measurements by Wang et al. [4], Matsui et al. [37], and Awaka et al. [6] are shown for comparison.

Figure 19a gives an example of the imaginary part of transverse conductivity $\sigma_T(\boldsymbol{k}, \omega)$ over ε_0 for the first k value (0.24 Å^{-1}) as a function of frequency for the ID model at 800 K. The linear fit (inset of **Figure 19**a) yields a slope of $\varepsilon_r(0) - 1$ where $\varepsilon_r(0)$ is the static (zero frequency) dielectric constant. The results of $\varepsilon_r(0)$ of all three models at different temperatures are summarized in **Figure 19**b. In the tetragonal phase, the dielectric constants of the three models

decrease with increasing temperatures, as expected for typical materials due to thermal agitation. On the other hand, the dielectric constants of the three models increase with increasing temperatures and we believe this is due to mobile Li ions. The dielectric constant of tetragonal and cubic Li_7 is not known but S. Narayanan et al.[119] reported that $Li_{5+2x}La_3Nb_{2-x}Y_xO_{12}$ (x=0.25, 0.5, and 0.75) have dielectric constants around 60 below room temperature.
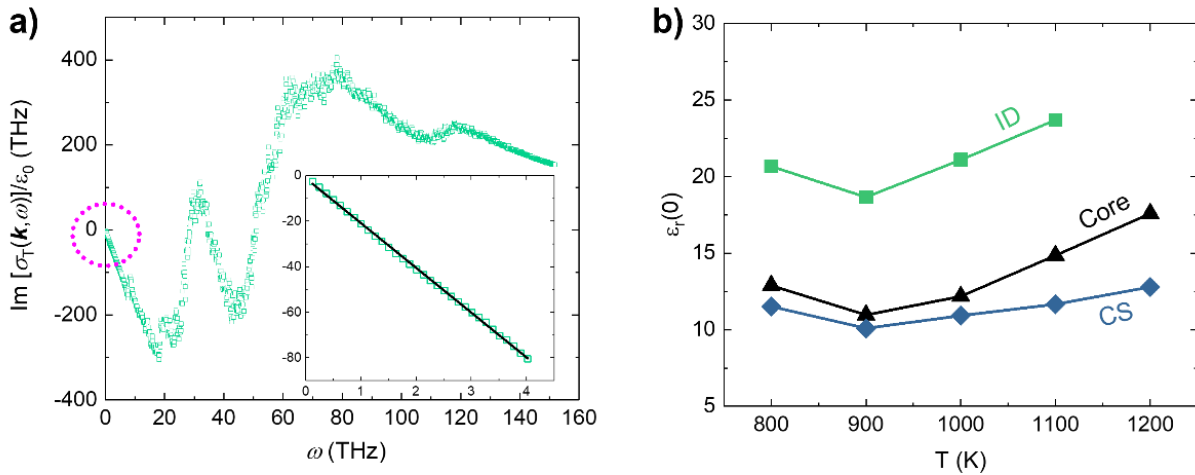

Figure 19 (a) The imaginary part of transverse conductivity $\sigma_T(\boldsymbol{k}, \omega)$ over ε_0 as a function of frequency for the ID model at 800 K. The inset shows details at low frequencies, and the solid line is a linear fit. (b) The dielectric constant at zero frequency $\varepsilon_r(0)$ as a function of temperature for Core, CS, and ID models.

3.3.4 Bulk modulus and shear modulus

Last but not the least, the mechanical properties of solid-state electrolytes (SSEs) also play an important role in the fabrication and operation process of all-solid-sate LiBs. According to Monroe and Newman, the shear modulus of SSEs that are two times higher than that of Li metal would suppress Li dendrite growth in the SE/Li metal interface[120]. For this reason, we also calculated and compared the bulk modulus (B) and the shear modulus (G) of the three models, as shown in **Figure 20**. It can be seen that Li_7 exhibits a high shear modulus, which is way higher than that of Li metal (~8.5 GPa). Both B and G decreases with increasing temperature, suggesting

the material softens upon heating. The Core model has the highest values of both B and G, while

the CS and ID models have similar elastic moduli. Experimental values at 300 K from Ni. et al.[121]

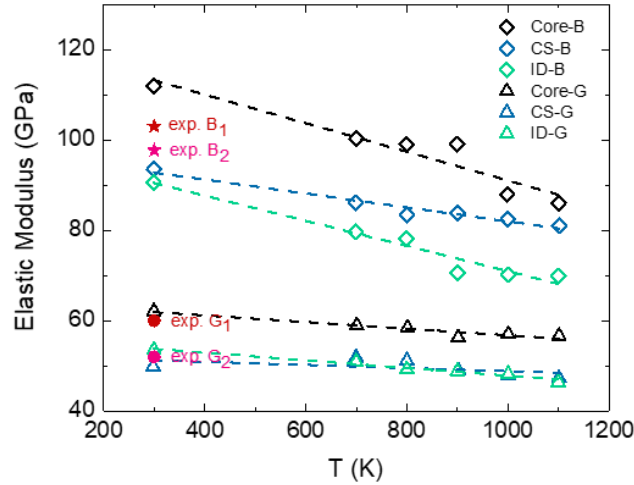are presented in **Figure 20** and they are similar to our computational values.

Figure 20 Elastic modulus as a function of temperature for Core, CS, and ID models. Experimental values from Ni et al. [39] are shown for comparison.

3.4 Conclusions

In this chapter, we compared one non-polarizable (core/Core) and two polarizable (core-

shell/CS and induced-dipole/ID) models for the molecular dynamics simulation of a fast-ion

conductor, $Li_7La_3Zr_2O_{12}$ (Li_7). Overall, we think it is difficult to explicitly point out which model

is the best, as all three models can reproduce various structural and dynamic properties (lattice

parameters, diffusivity, conductivity, dielectric constants, and elastic moduli) of Li_7 reasonably

well. Due to various limitations of existing codes, we used different methods to obtain potential

parameters, e.g., arbitrary vs first-principles charge, Buckingham vs Buckingham+Morse short-

range interaction, empirical fit vs force-matching, etc. We believe this also complicates the direct

comparison of different potential models. On the other hand, we think the ID model combined

with the force-matching approach is the most advanced one as it includes the polarization through

atomic polarizability and takes from first-principles results as the input. The CS model includes the polarization through a spring-connected shell where parameters of shell charge and spring constant are almost entirely empirical. Looking forward, we think that the ID model can be improved by incorporating the anisotropy in the atomic polarizability and fluctuating charges, where the charge will vary with the local chemical environment. Furthermore, only pair potentials were considered in these three models while many-body potentials will be more accurate to describe the mixed metallic/covalent nature of the bonding.

CHAPTER 4 Study of diffusion and conduction in lithium garnet oxides Li$_x$La$_3$Zr$_{x-5}$Ta$_{7-x}$O$_{12}$ (x=5-7) by machine learning interatomic potential

4.1 Motivation

As ionic conductivity is one of the most important properties of solid electrolytes, many experimental results have been reported for various compositions of Li$_x$La$_3$Zr$_{x-5}$Ta$_{7-x}$O$_{12}$ (x=5-7), including both Al contaminated (through alumina crucibles), Al-doped, and nominally Al-free phases. **Figure 21** summarized some work of Al-free and Al-contaminated experiments. For example, Wang et al.[22] and Li et al.[52] used alumina crucibles and found that ionic conductivity reaches a maximum at x=6.7 (0.96×10^{-3} S/cm) and x=6.4 (1.0×10^{-3} S/cm), respectively. The difference between these two is that the former is for the bulk and the latter for the total. On the other hand, Buschmann et al.[46], Inada et al. [48], Matsuda et al. [54] and Yi et al.[51] synthesized Al-free compositions of Li$_x$La$_3$Zr$_{x-5}$Ta$_{7-x}$O$_{12}$ and found that ionic conductivity reaches a maximum at x=6 (2.6×10^{-4} S/cm), x=6.5 (6.1×10^{-4} S/cm), x=6.6 (4.7×10^{-4} S/cm), and x=6.7 (1.03×10^{-3} S/cm), respectively. Furthermore, Kataoka et al.[19] synthesized single crystals and found x=6.6 has the highest ionic conductivity of 1.1×10^{-3} S/cm. Thus, it appears that it is controversial as to what is the composition for the maximum conductivity in Li$_x$La$_3$Zr$_{x-5}$Ta$_{7-x}$O$_{12}$ even in Al-free samples.

In recent years, the machine learning interatomic potentials (MLIP) based on the artificial neural network (NN) model has received considerable attention as they show a combination of DFT accuracy and IP efficiency[79, 122-124]. In this chapter, we applied MLIP-based MD simulations to investigate lithium garnet series Li$_x$La$_3$Zr$_{x-5}$Ta$_{7-x}$O$_{12}$ (x=5, 6, 6.5, 6.75, and 7), named Li$_5$, Li$_6$, Li$_{6.5}$, Li$_{6.75}$, and Li$_7$ afterward. First, we compare the force/virial errors of MLIP, along with other commonly applied methods such as Core, ID, and DFTB, and check how well they can reproduce the self-diffusivity and ionic conductivity of Li$_6$. Second, we present the MLIP

error against DFT for all compositions of Li_5, Li_6, $Li_{6.5}$, $Li_{6.75}$, and Li_7 and show how this MLIP is approaching DFT accuracy. Third, we examine the temperature dependence of diffusion and conduction of various compositions including the defect structure. Finally, we turn to composition dependence and focus on the question of what composition gives the highest ionic conductivity, by considering both experimental literature and present computational results.
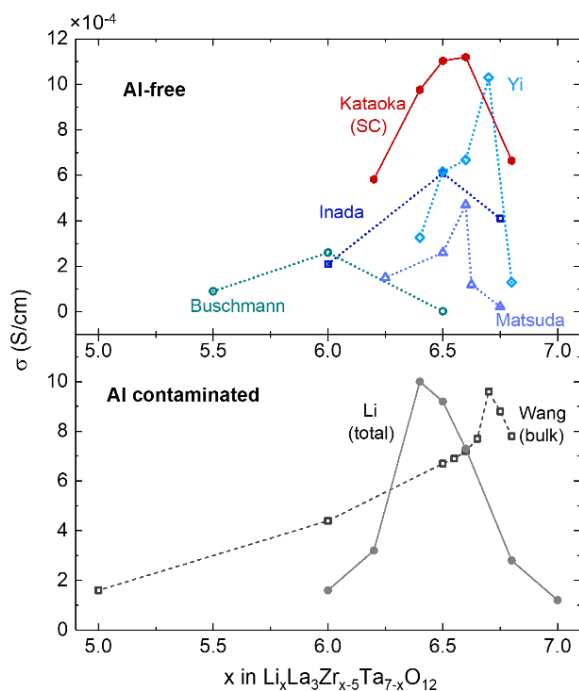

Figure 21 Summary of composition dependence of ionic conductivity of $Li_xLa_3Zr_{x-5}Ta_{7-x}O_{12}$ (x=5-7) from the literature [19, 22, 46, 48, 51, 52, 54]. SC: single crystal.

4.2 Construction of MLIP, Core, ID, and DFTB potentials

4.2.1   Construction of machine learning interatomic potential

The MLIP potential of lithium garnet series $Li_xLa_3Zr_{x-5}Ta_{7-x}O_{12}$ was trained with the DFT-MD trajectories of Li_5, Li_6, and Li_7 with energy, force, and cell-virial included in the training. DFT-MD simulations for all compositions were performed using the Vienna ab initio simulation package (VASP)[110] within the projector augmented-wave (PAW)[109] approach using the PBEsol[108] exchange-correlation functional. The plane-wave energy cutoff was 500 eV and a

single Γ point was sampled. First, we performed MD simulations, using an NPT ensemble, at 1200 K for 3 ps with a 1fs time step. For each composition, configurations were sampled every 4 fs after skipping the first 100 fs. 90% of this DFT dataset was used for training and 10% was used for validation. In the meanwhile, we used the average structure of the DFT-MD trajectory to obtain the atomic charges in the DDEC6 scheme[91], which are listed in **Table 6**, to be used in the calculation of the ionic conductivity for the MLIP model.

Table 6 DDEC6 charge of each composition.

	Li_5	Li_6	$Li_{6.5}$	$Li_{6.75}$	Li_7
La	1.87	1.88	1.88	1.84	1.89
Ta	2.32	2.33	2.33	2.23	—
Zr	—	2.23	2.23	2.18	2.25
O	-1.20	-1.26	-1.29	-1.28	-1.32
Li	0.83	0.82	0.82	0.81	0.81

MLIP potential was trained with the SNU Interatomic Machine-learning PotentiaL packagE-version Neural Network (SIMPLE-NN) package[122], with atom-centered symmetry functions (ACSF)[79] as a descriptor and neural network (NN) (two hidden layers with 30 nodes in each layer) as the regressor. To develop the ideal potential for the Li garnet series $Li_xLa_3Zr_{x-5}Ta_{7-x}O_{12}$, we started by studying the potential parameter effect on Li_5, weighting factors, learning rate, and transfer functions. The criterion of the fitting is based on the loss function or the root mean square error for energy, force, and stress, which can be defined as (angle bracket represents the average over all frames):

$$F_{Loss} = w_E \left\langle \left(\frac{E_{DFT}-E_{IP}}{N}\right)^2 \right\rangle + w_f \left\langle \frac{(f_{DFT}-f_{IP})^2}{3N} \right\rangle + w_S \left\langle \frac{(S_{DFT}-S_{IP})^2}{6} \right\rangle,$$

where w_E, w_f, and w_S are the weighting factors of energy, force, and stress. In simple-NN, the weighting factors of energy and force were set as default, i.e., $w_E = 1$ and $w_S = 0.00001$. In other words, the goal of the fitting is to minimize the force term,

51

$$\frac{(f_{DFT} - f_{IP})^2}{3N} = \frac{1}{3N} \sum_{i=1}^{N} \sum_{k=1}^{3} [f_{DFT}(i,k) - f_{IP}(i,k)]^2$$

where N is the number of atoms, and 3 means x, y, and z in three directions. First, we compared different values of w_f (i.e., 0.05, 0.1, and 0.5) and finally decided to set w_f to 0.1.

We also compared two different activation functions used in the hidden layers, i.e., the hyperbolic tangent $f(x) = tanh(x)$ and the sigmoid function $f(x) = \frac{1}{1+exp(-x)}$. **Figure 22** shows the root mean squared error (RMSE) of atomic forces and cell virials. It is found that the sigmoid function has a smaller RMSE compared to tanh function.
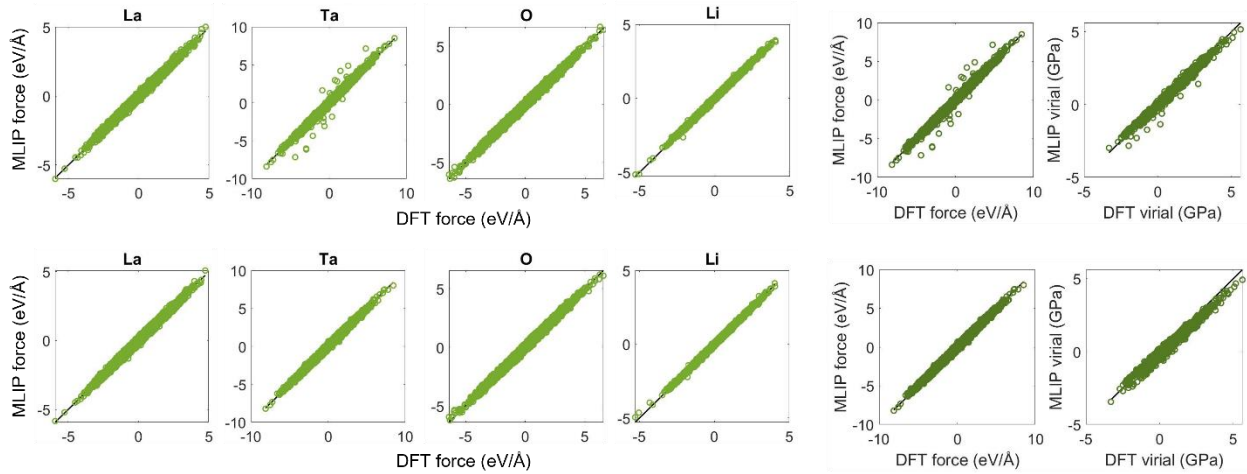

Figure 22 The comparison of atomic forces and cell virials between MLIP (scatter points) against DFT (black lines) for $Li_5La_3Ta_2O_{12}$ using tanh (top) and sigmoid (bottom) activation functions with the same learning rate and w_f.

The NN potential parameters were optimized through the loss function for the training set i.e., configurations of DFT-MD). However, these structures contain various deformations, surfaces, and defects, meaning the descriptor is highly inhomogeneous and biased. This unbalanced training could significantly undermine the accuracy and reliability of NN potential, and therefore the Gaussian density function (gdf) has been added to cure the training bias and increase the

transferability of the potential[122, 125]. **Figure 23** compared the lattice parameters of Li_5 from MLIP-MD using sigmoid and sigmoid+gdf activation functions in the training, it can be seen that the lattice parameters calculated from sigmoid+gdf exhibit a linear dependence of temperature.
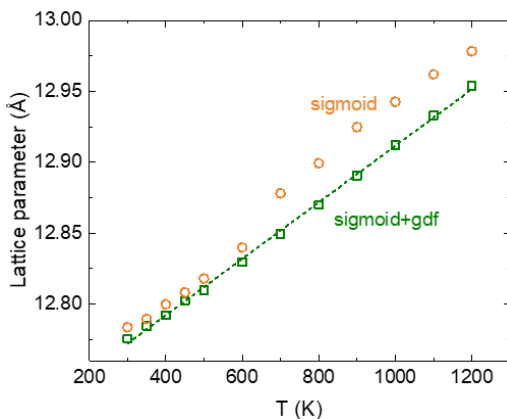

Figure 23 Lattice parameter of $Li_5La_3Ta_2O_{12}$ using different activation functions, i.e., sigmoid and sigmoid+gdf.

4.2.2 Construction of Core, ID, and DFTB potentials

The Core model potentials were taken from the work of Chen et al.[126], which was fitting from the experimental data. ID model (80 % of formal charge) of Li_6 was trained with CP2K[106, 107] on the DFT-MD trajectory including only forces but all configurations, as we did previously in Chapter 3 for Li_7. DFTB parameterization for the Li-La-Zr-Ta-O chemical space was obtained with the Tight-binding Approximation-enhanced Global Optimization (TANGO) method[127] with CP2K as the DFT package including both energy and force.

4.3 Computational and experimental details

4.3.1 Molecular Dynamic Simulations

As mentioned in the Motivation, there was Li loss during the high-temperature synthesis and arbitrary amounts of lithium precursor were often added to compensate for this. It is thus worthwhile comparing the normal (nominal composition) to defect structures with Li loss. In this

work, in addition to Li_5, Li_6, $Li_{6.5}$, $Li_{6.75}$, and Li_7, we also added the $Li_{5.88}La_3Zr_{1.5}Ta_{0.5}O_{11.69}$ (10 mol% Li_2O off of $Li_{6.5}$, named $Li_{6.5}$defect afterward).

MD simulations of the Core and MLIP models were performed using Large Scale Atomic/Molecular Massively Parallel Simulator (LAMMPS)[128] with $2\times2\times2$ supercells. MD simulations of the ID and DFTB models were performed using CP2K with $2\times2\times2$ and $1\times1\times1$ supercells, respectively. Details of MD simulations including the ensemble, thermostat, barostat, etc. are listed in **Table 7**, along with the approximate simulation cost. DFT-MD simulation of $2\times2\times2$ supercells is expected to be 5 or 6 orders of magnitude slower than MLIP.

Table 7 MD simulation details. The approximate simulation time of four models for 1 ns of trajectory is shown (Core, ID, and MLIP models were using 64 CPUs while the DFTB model was using 28 CPUs). It is worth noting that the DFTB model is using $1\times1\times1$ while other models are using $2\times2\times2$ supercells.

Ensemble	Parameters	Core	ID	DFTB	MLIP
NPT	thermostat (ps)	0.05	0.1	0.1	0.1
	barostat (ps)	0.25	0.5	0.5	0.5
	timestep (fs)	1	1	1	1
	lattice parameter average range (ps)	30 – 50	30 – 50	30 – 75	30 – 50
NVT	thermostat (ps)	—	—	1	—
	timestep (fs)	—	—	1	—
	trajectory length (ns)	—	—	0.5 – 3	—
NVE equilibration	thermostat (ps)	0.1	0.1	—	0.1
	trajectory length (ps)	50	50	—	50
NVE	timestep (fs)	1	1	—	1
	trajectory length (ns)	0.5 – 300	0.5 – 8	—	0.5 – 40
NVT/NVE	approximate simulation time per ns trajectory (h)	0.3	40	170	20

4.3.2 Experiments

Powders of Li_6 and $Li_{6.5}$ were prepared with a solid-state reaction where stoichiometric quantities of $LiOH\cdot H_2O$ (Alfa Aesar, 98%), La_2O_3 (Alfa Aesar, 99.9%), ZrO_2 (Alfa Aesar, 99.7%) and Ta_2O_5 (Alfa Aesar, 99.85%) were used as raw materials. La_2O_3 powders were heated at 900 °C for 12 h in a MgO crucible (all crucibles and lids used in this work were MgO to avoid Al

contamination). An extra 10 wt% LiOH·H$_2$O was added to compensate for lithium loss during calcination. The powders were wet-milled in a roller mixer for 12 h in polyethylene jars filled with 2-propanol and then the slurry was dried by infrared heating. The mixed powders were calcined at 1000 °C for 12 h with a heating and cooling rate of 2 °C/min in MgO crucibles covered by MgO lids. Afterward, another extra 10 wt% or 5 wt% LiOH·H$_2$O were added into the calcined powders of Li$_6$ and Li$_{6.5}$, respectively and ball-milled again, and finally pressed into 13mm diameter pellets and sintered at 1150 °C for 12 h. The silver paste was applied to both sides of the pellets as blocking electrodes and heated at 700 °C. Impedance tests at a temperature range of 22 – 700 °C were performed using the same setup as in our previous work[23] with airflow. A sinusoidal voltage with an amplitude of 10 mV was applied for the frequency range of 3 MHz to 1 Hz.

4.4 Results and discussion

4.4.1   Comparing Different Models for Li$_6$

Before studying the whole series of Li$_5$, Li$_6$, Li$_{6.5}$, Li$_{6.75}$, Li$_7$, and Li$_{6.5}$defect, we want to compare the results of MLIP vs other commonly utilized models, using a representative composition of Li$_6$. We will compare the model force/virial against DFT values, and lattice parameters, self-diffusivity, and ionic conductivity against experimental values.

4.4.1.1 Force and virial

Atomic force (3 for each atom) and cell-virial (6 for each structure) values from the trained MLIP, ID, and DFTB models against DFT values out of 145 structures are shown in **Figure 24**. Deviation from DFT results is assessed by the root mean squared error (RMSE). RMSE of force and virial for the MLIP model are 0.14 eV/Å and 0.20 GPa, respectively, which are lower than that of Core, DFTB, and ID models.
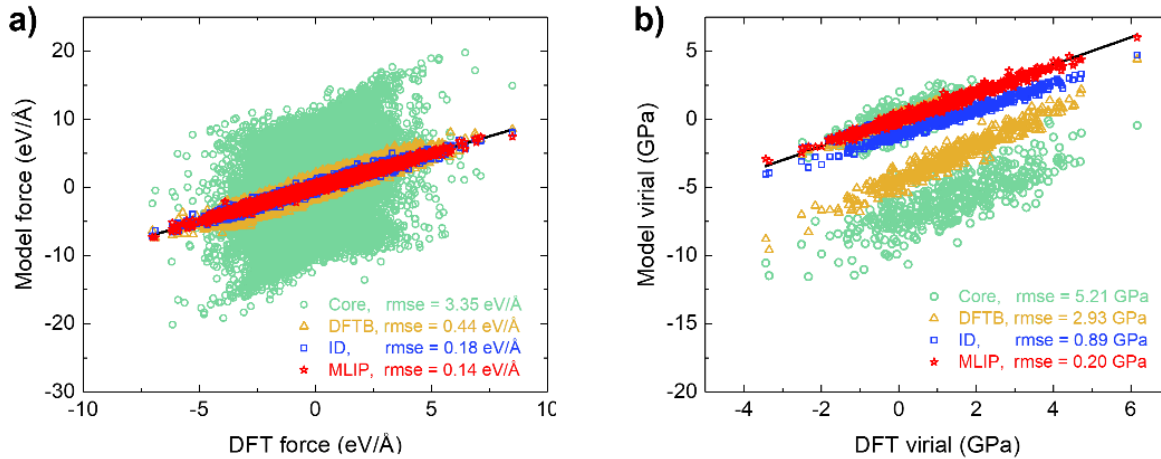
Figure 24 The comparison of (a) atomic forces and (b) cell virials of Core, DFTB, ID, and MLIP (scatter points) against DFT (black lines) for $Li_6La_3ZrTaO_{12}$.

4.4.1.2 Lattice parameters of $Li_6La_3ZrTaO_{12}$ using different models

We first checked the temperature dependence of lattice parameters, shown in **Figure 25** to see if these four models could reasonably predict the thermal expansion of $Li_6La_3ZrTaO_{12}$ (Li_6). We include diffraction results from various works of literature [46, 54, 86, 129] in the figure for comparison. Most experimental measurements of lattice parameters were performed at room temperature. At room temperature, the lattice parameters of MLIP, Core, and ID models have an error between 0.1 - 0.3 %, while the DFTB model's error is ~0.6 %. If we use the 10 K and 300 K measurement results from Wang et al.[86] as a reference, we see that all four models predict a nearly constant thermal expansion and similar expansion coefficients. Specifically, the thermal expansion coefficients for the MLIP, Core, ID, and DFTB models are 1.74×10^{-5}, 1.51×10^{-5}, 1.57×10^{-5}, and 1.91×10^{-5} K^{-1}, respectively.
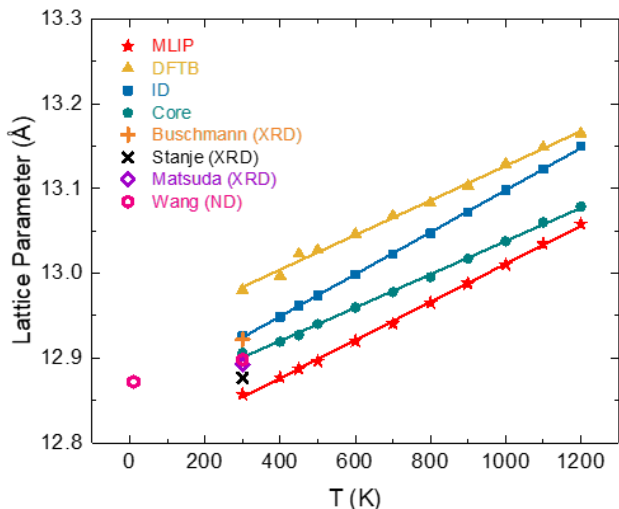
56

Figure 25 Lattice parameter as a function of the temperature of $Li_6La_3ZrTaO_{12}$ from different models. Literature values of Al-free samples at room temperature[46, 54, 86, 129] are shown for comparison. XRD: X-ray diffraction; ND: neutron diffraction. Solid lines are linear fit.

4.4.1.3 Diffusion and conduction properties comparison among different models

Self-diffusivity and ionic conductivity from the four models are plotted in **Figure 26**, along with experimental results from single crystal measurements. All four models predict similar self-diffusivity and conductivity at high temperatures. However, if we examine the whole temperature, the MLIP model agrees with experiments the best, while the ID and Core models significantly over- and under-estimates, respectively, the low-temperature diffusion and conduction. While it is understandable that the Core model did not perform well due to the very large force error (**Figure 24**), it is surprising to see the prediction from the ID model, as its force error is comparable to that of MLIP. We believe that this indicates that the ID model lacks transferability. The DFTB model predicts diffusion and conduction similar to those of MLIP, but its force error is much higher. Thus, it is possible some self-cancellation leads to its reasonable performance. In addition, the DFTB model is much more computationally expensive compared with other three models. As shown in **Table 7**, the simulation time for a 1 ns trajectory is approximately 170 hours for a 1×1×1 supercell, while the other models take less than 40 hours for supercells that are 8 times bigger.
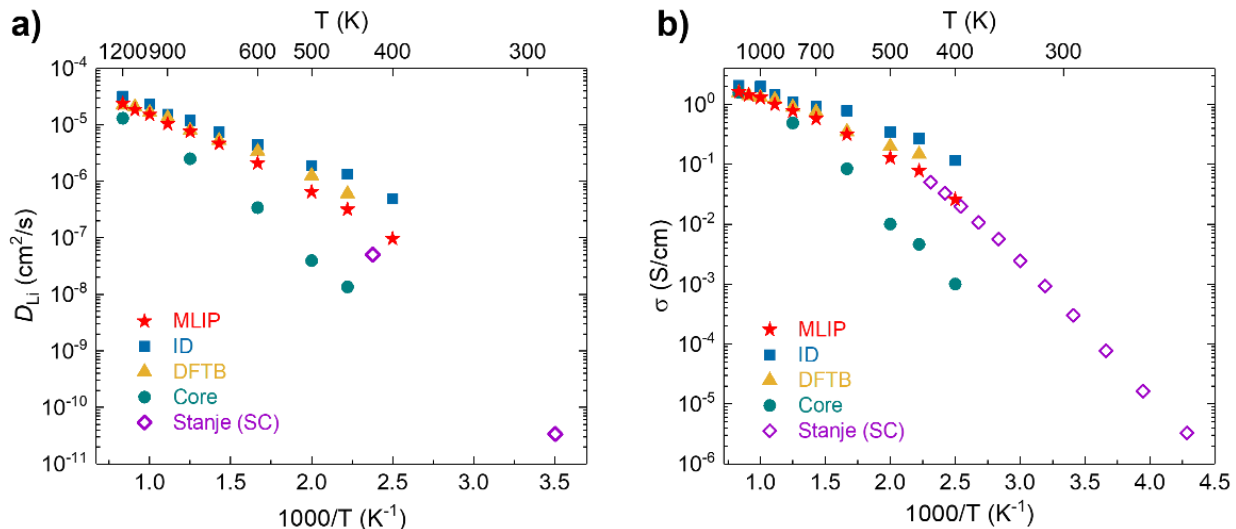
57

Figure 26 (a)Self-diffusivity and (b) ionic conductivity of $Li_6La_3ZrTaO_{12}$ as a function of inverse temperature from different models. Single crystal (SC) data from Stanje et al.[129] are shown for comparison.

Self-diffusivity from MLIP is slightly higher than experimental values at low temperatures. It is worth noting that the work of Stanje et al.[129] only measured the relaxation time from nuclear magnetic resonance experiments and assumed a jump length of 2 Å. As will be shown later in **Figure 28**b, we found the jump length is 2.3 Å at 400 K. If 2.3 instead of 2 Å was used, the agreement of MLIP to experiment will be even better.

4.4.2 Force/virial Error and Lattice Parameter

Force and virial error against DFT (i.e., PBEsol) for the whole series studied in the present work are shown in **Table 8**. To understand the meaning of these numbers, we also compared the error between two different exchange-correlation functional, i.e., PBE vs PBEsol, and found the force error was about 0.1 eV/Å. In other words, we can argue the DFT error might be around 0.1 eV/Å and our MLIP model is approaching DFT accuracy but much faster (DFT will be 5 to 6 orders of magnitude slower based on our estimate). Furthermore, it is transferable as it shows similar errors for different compositions, i.e., Li_5 to Li_7.

58

Table 8 The root mean squared error (RMSE) values of atomic forces, and cell virials between MLIP and DFT for all the compositions studied. RMSE between PBE and PBEsol are shown for comparison.

	Force (eV/Å)	Virial (GPa)
Li_5 PBE vs Li_5 PBEsol	0.10	2.57
MLIP vs Li_5 PBEsol	0.15	0.23
MLIP vs Li_6 PBEsol	0.14	0.20
MLIP vs $Li_{6.5}$ PBEsol	0.12	0.21
MLIP vs $Li_{6.75}$ PBEsol	0.12	0.22
MLIP vs Li_7 PBEsol	0.11	0.22

Before applying this MLIP model to study the diffusion and conduction properties, we want to check if it can reproduce the structure of different compositions in terms of lattice parameters. The temperature dependence of lattice parameters is shown in **Figure 27**a. For cubic phases such as Li_5, Li_6, $Li_{6.5}$, and $Li_{6.5}$defect, lattice parameters increase linearly with increasing temperatures with similar thermal expansion coefficients. The lattice parameter of $Li_{6.5}$ and $Li_{6.5}$defect are almost the same. For Li_7, the tetragonal to cubic phase transition takes place at a temperature range between 1000 and 1100 K, which is slightly higher than the experimental value of 913 K[53]. For $Li_{6.75}$, the tetragonal to the cubic phase transition is around 700-800 K.

Figure 27b shows calculated lattice parameters at room temperature as a function of x (Li content) in $Li_xLa_3Zr_{x-5}Ta_{7-x}O_{12}$. Experimental data of single crystals from Kataoka et al.[19], Al-free powder samples from Buschmann et al.[45], Matsuda et al.[46], Awaka et al.[54], and Thompson et al.[130] are shown in the plot for comparison. For cubic phases, the lattice parameter increases linearly with increasing Li content. Our simulation data agree very well with experimental values reported in the literatures. Both simulation and experimental results suggest that the cubic to tetragonal transition takes place at around x=6.6 at room temperature, except for Kataoka et al.[19] where it was cubic even at x=6.8.
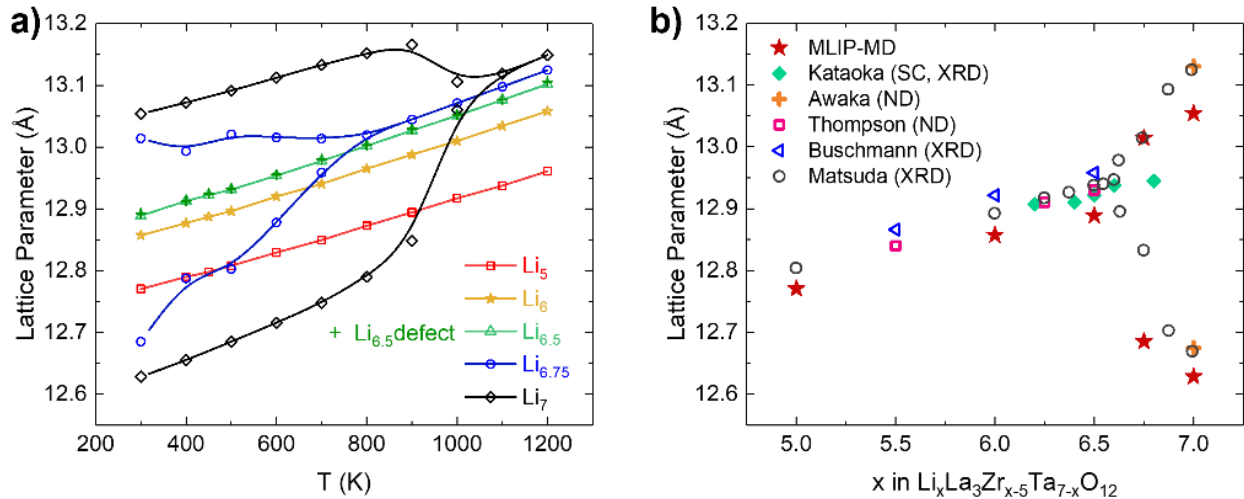
Figure 27 (a) Lattice Parameters as a function of the temperature of $Li_5La_3Ta_2O_{12}$ (Li_5), $Li_6La_3ZrTaO_{12}$ (Li_6), $Li_{6.5}La_3Zr_{1.5}Ta_{0.5}O_{12}$ ($Li_{6.5}$), $Li_{6.75}La_3Zr_{1.75}Ta_{0.25}O_{12}$ ($Li_{6.75}$), $Li_7La_3Zr_2O_{12}$ (Li_7), and $Li_{5.88}La_3Zr_{1.5}Ta_{0.5}O_{11.69}$ ($Li_{6.5}$defect). Solid lines are a guide to the eye. (b) Lattice parameters from MLIP-MD at room temperature versus x (Li content). Literature values of single crystals (SC)[19] and Al-free powders[45, 46, 54, 130] are shown for comparison.

4.4.3 Temperature Dependence of Self-diffusion

Li diffusion was investigated by the incoherent density correlation function as introduced in Chapter 2.2, from which the residence time, jump length, and self-diffusivity (D_{Li}) could be extracted. **Figure 28**a-c summarizes the residence time, jump length, and self-diffusivity of Li_5, Li_6, $Li_{6.5}$, $Li_{6.75}$, and Li_7 at the temperature range of 400 – 1200 K. In terms of self-diffusivity (**Figure 28**c), temperature dependence is roughly Arrhenius with activation energies (0.26 - 0.33 eV), except for Li_7, where the cubic (0.27 eV) and tetragonal (1.33 eV) phase have very different activation energies. Li_5 has the highest diffusivity at high temperatures while $Li_{6.5}$ has the highest diffusivity at low temperatures. Self-diffusivity is related to residence time (t) and jump length (l) as $l^2/(6t)$. **Figure 28**b indicates that jump lengths have a narrow range of 1-3.5 Å, with shorter jumps at higher temperatures. The nearest neighbor tetrahedral and octahedral sites in lithium garnets are 1.5-2.5 Å[44]. The plot of residence time, the average time a Li spends on a site before

jumping to the next site, largely follows **Figure 28**c, as the jump length is relatively temperature insensitive.
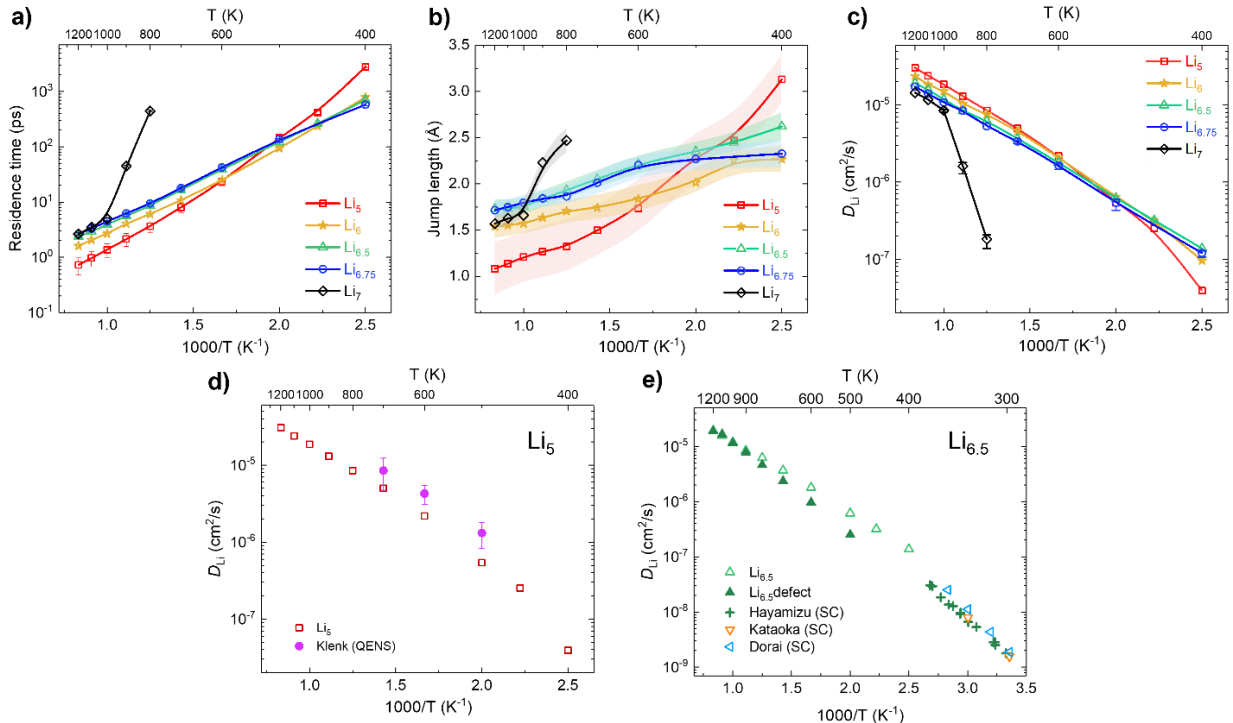

Figure 28 Inverse temperature dependence of (a) residence time, (b) jump length, and (c) self-diffusivity of Li of $Li_5La_3Ta_2O_{12}$ (Li_5), $Li_6La_3ZrTaO_{12}$ (Li_6), $Li_{6.5}La_3Zr_{1.5}Ta_{0.5}O_{12}$ ($Li_{6.5}$), $Li_{6.75}La_3Zr_{1.75}Ta_{0.25}O_{12}$ ($Li_{6.75}$), and $Li_7La_3Zr_2O_{12}$ (Li_7). Solid lines are a guide to the eye and shades in (b) are the range of error. (d-e) Self-diffusivity as a function of inverse temperature for Li_5 and $Li_{6.5}$. Experimental data from pulse-field gradient NMR measurements of single crystal (SC)[21, 131, 132] and QENS measurements [44] are shown for comparison.

To show a comparison of self-diffusivities between the results calculated from our MD simulations and that from the experiments, we plotted the results of Li_5 and $Li_{6.5}$ separately in **Figure 28**(d-e). A comparison for Li_6 was shown previously in **Figure 26**a. Computed self-diffusivity values are slightly lower than those from quasi-elastic neutron scattering (QENS) measurements[44] for Li_5, while they are slightly higher than those from pulse-field NMR measurements[21, 131, 132] for single crystals of $Li_{6.5}$. In **Figure 28**e, we also compared the normal and defect structure of $Li_{6.5}$. Self-diffusivities of these two structures are almost the same

at high temperatures, e.g., 900 -1200 K, while the defect structure has noticeably lower diffusivity at low temperatures.

4.4.4 Temperature Dependence of Ionic Conductivity

Similar to the self-diffusivity plot, we present in **Figure 29**a the ionic conductivity of Li_5, Li_6, $Li_{6.5}$, $Li_{6.75}$ and Li_7, and in **Figure 29**d-f the comparison to experiments. It is usually assumed an Arrhenius relation between ionic conductivity and reverse temperature from a limited temperature range, however, examination of our wide-temperature experimental measurement of ionic conductivities of Li_6 and $Li_{6.5}$ from this work, along with that from Stanje et al.[129] and Jin et al.[133] as in **Figure 29**d/e, clearly suggests a non-Arrhenius behavior. Given this, we chose a common non-Arrhenius model, Vogel-Tammann-Fulcher (VTF) equation[134-136] with $\sigma = A \cdot exp\left[-\frac{B}{T-T_0}\right]$, where A is a pre-exponential factor, B the artificial activation energy, T_0 the Vogel temperature below which ions are not mobile. We applied the VTF fit to our MD data, except for Li_7 where we applied the Arrhenius fit for the cubic (0.13 eV) and tetragonal (1.15 eV) phase separately. The transition temperature T_0 is plotted in **Figure 29**b. Its values are below 200 K and decrease with increasing Li content, which suggests that higher Li content might lead to higher conductivity at low temperatures. If we extrapolate MD data through the VTF fit to lower temperatures, we can see they agree well with single crystal data from experiments, except for $Li_{6.75}$.
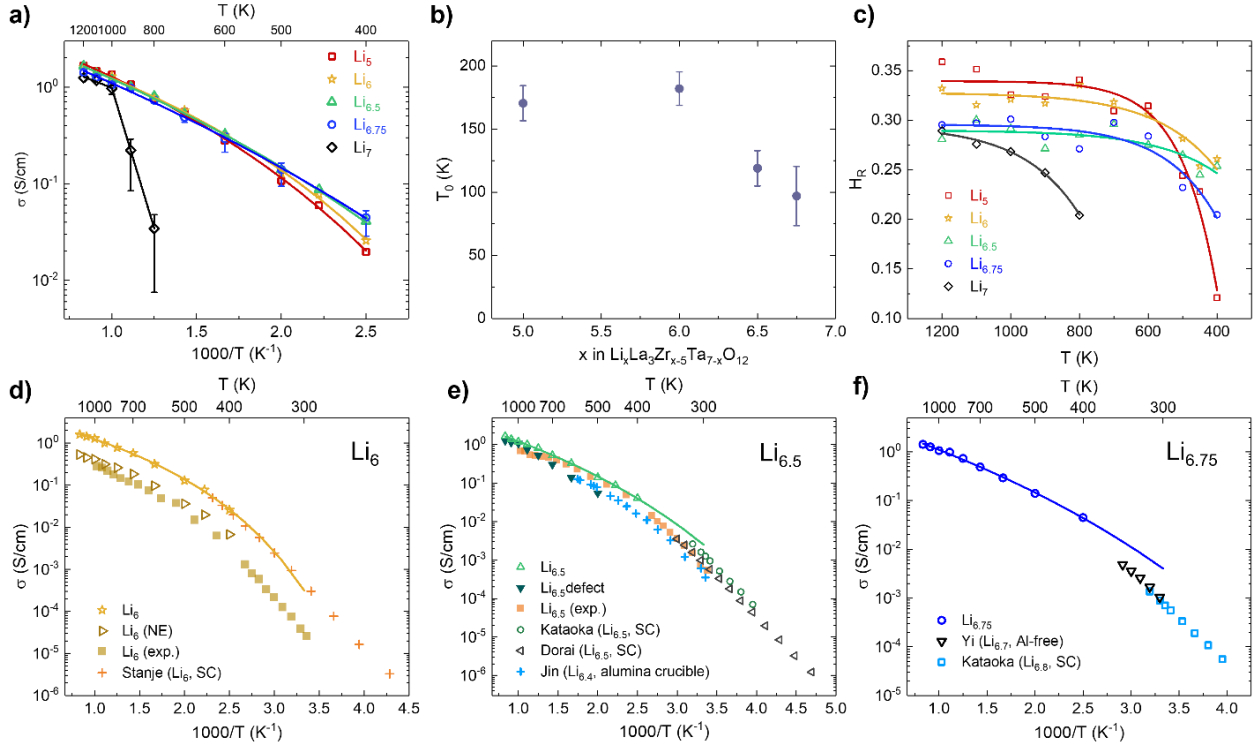
Figure 29 (a) Ionic conductivity as a function of inverse temperature for $Li_5La_3Ta_2O_{12}$ (Li_5), $Li_6La_3ZrTaO_{12}$ (Li_6), $Li_{6.5}La_3Zr_{1.5}Ta_{0.5}O_{12}$ ($Li_{6.5}$), $Li_{6.75}La_3Zr_{1.75}Ta_{0.25}O_{12}$ ($Li_{6.75}$), and $Li_7La_3Zr_2O_{12}$ (Li_7). Solid lines are fitted to the VTF equation (except for Li_7 where two Arrhenius fits are applied to the high and low temperatures). Error bars of $Li_{6.75}$ and Li_7 represent the ionic conductivity in the *ab* and *c* directions. (b) Vogel temperature (T_0) of different Li content. (c) H_R for the composition series. Solid lines are a guide to the eye. (d-f) Comparison of results from (a) and experimental values for Li_6, $Li_{6.5}$/$Li_{6.5}$defect ($Li_{5.88}La_3Zr_{1.5}Ta_{0.5}O_{11.69}$), $Li_{6.75}$. Experimental values include single crystal (SC)[19, 21, 129, 131], Al-free[51], and Al contaminated powders (through alumina crucibles)[133].

In **Figure 29**d, we also compared the Nernst-Einstein conductivity (σ_{NE}) and (coherent) ionic conductivity of Li_6. It shows that the coherent ionic conductivity is higher than the Nernst-Einstein conductivity, which indicates the ionic motion is positively cooperated, i.e., ions moving together is faster than moving alone. This positive cooperation was called concerted in the studies of Li_7[116, 137]. The Haven ratio is plotted in **Figure 29**c for all compositions, with values between 0.1 and 0.4. A Haven ratio of ~0.3 was reported by He et al.[137] (900 K) and Mottet et al.[138]. Temperature dependence of Haven ratio indicates a higher value (less cooperation) at higher temperatures. This is intuitive as it is expected that the thermal agitation tends to break the

atomic cooperation, which makes the atomic motion more independent. In **Figure 29**e, we compared the ionic conductivity of $Li_{6.5}$ and $Li_{6.5}$defect. Similar to the self-diffusivity comparison in **Figure 28**e, the ionic conductivity of normal structure is higher.

4.4.5   Finite-size effects on Li-ion transport

We further investigated the finite-size effect on self-diffusivity and ionic conductivity of $Li_{6.5}La_3Zr_{1.5}Ta_{0.5}O_{12}$ at a temperature range of 800 -1200 K to examine if the results converged with respect to the supercell size. The initial cells of $1\times1\times1$ (188 atoms) and $3\times3\times3$ (5076 atoms) were adopted to compare with the current $2\times2\times2$ (1504 atoms) structures. The comparison of the finite-size effect is displayed in **Figure 30**. It is found that $1\times1\times1$ cell has higher values of ionic conductivity at 900 and 1200 K. The difference between $2\times2\times2$ and $3\times3\times3$ supercells at high temperatures is ignorable. Note that, the simulation time of $3\times3\times3$ supercells are more than three times of $2\times2\times2$ supercells, hence, considering the computational cost, we believe that the $2\times2\times2$ supercell is the best option.
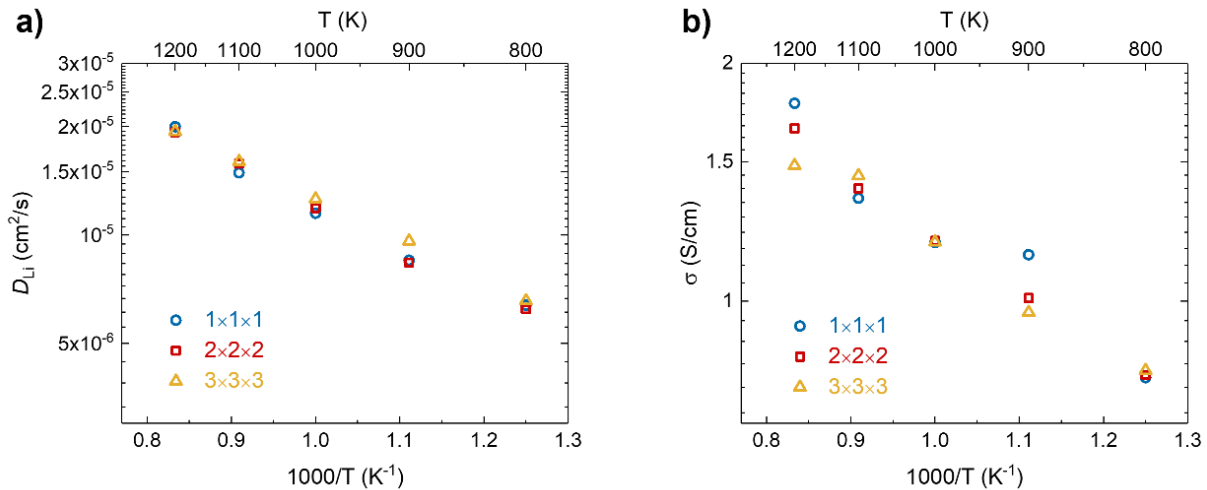

Figure 30 Finite-size effect on (a) self-diffusivity and (b) ionic conductivity for $1\times1\times1$, $2\times2\times2$, and $3\times3\times3$ cells of $Li_{6.5}La_3Zr_{1.5}Ta_{0.5}O_{12}$.

4.4.6 Composition Dependence

To examine the composition dependence of diffusion, we plotted in **Figure 31**a the self-diffusivity at 1200 K and 400 K to represent high and low temperatures, respectively. At 1200 K, the self-diffusivity decreases with increasing Li content, suggesting a vacancy mechanism. At high temperatures, each Li-ion has enough thermal energy to move around. However, as Li ions must move through a network of interconnected tetrahedral and octahedral sites, they will be competing for the vacant sites. At low temperatures, e.g., 400 K, Li ions do not have sufficient thermal energy so only some of them are moving around. Adding more Li will increase the overall Li-Li repulsion and initiate more Li to move, leading to overall increasing diffusivity with increasing composition.

The composition dependence of ionic conductivity is shown in **Figure 31**b. It is worth noting that we could not detect Li conduction at 400 K for Li_7 so MD simulation suggests the maximum conductivity at 400 K occurs at $Li_{6.75}$. If we compare **Figure 31**b with **Figure 21** presented in the motivation for room temperature experimental values from various works of literature, we can see the overall composition dependence looks similar. The difference is the peak composition. For example, results from Buschmann et al.[46] indicate the peak composition is Li_6. Yi et al.[51] showed that $Li_{6.7}$ has the highest ionic conductivity. Inada et al.[48] found $Li_{6.75}$ to be cubic and its ionic conductivity is lower than that of $Li_{6.5}$. Matsuda et al.[54] reported the peak at $Li_{6.6}$ and Li content 6.625 to 7 to be tetragonal. While these reports are all on polycrystalline samples, Kataoka et al.[19] synthesized single crystals and found $Li_{6.2}$ to $Li_{6.8}$ to be cubic with a peak conductivity at $Li_{6.6}$. From the perspective of experiments, single crystals are probably preferred over polycrystals as they are less susceptible to the influence of density and grain boundary segregation (e.g., space charge layer). However, an arbitrary amount of Li excess had to be added to all these samples, which makes the composition used for conductivity measurement a

little ambiguous after an arbitrary amount of Li loss during the high-temperature processing. Our

MD results suggest that Li loss, e.g., $Li_{6.5}$defect, will decrease the ionic conductivity. Finally,

experimental samples are also subjected to H_2O and CO_2 contamination to form LiOH and Li_2CO_3

and it is reasonable to expect such contamination will be more severe when Li is more mobile, i.e.,

high Li content. Nonetheless, it is probably reasonable to argue the maximum conductivity occurs

somewhere between 6.6 and 6.8 based on combined experimental and computational results.
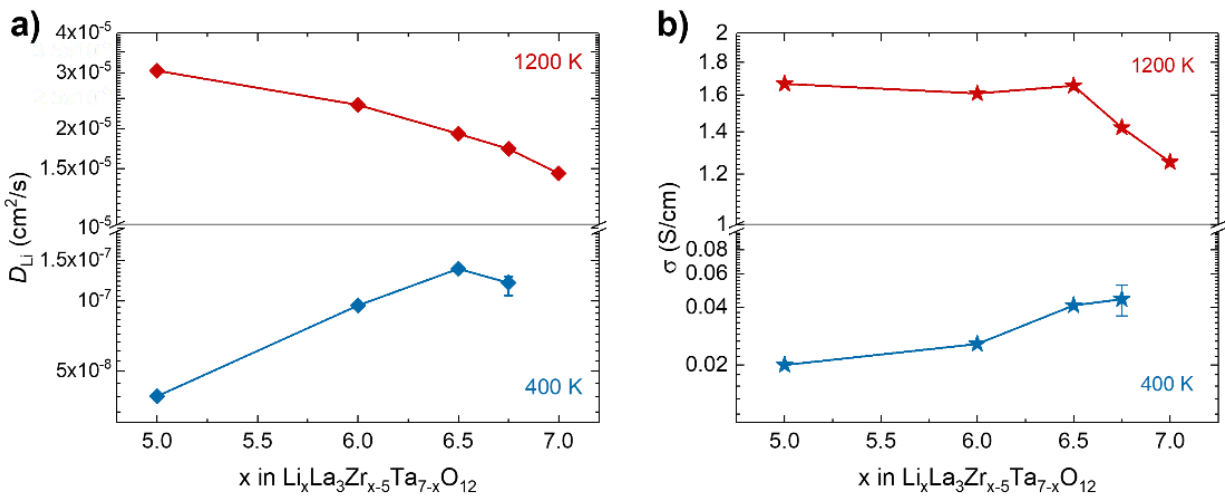

Figure 31 Composition dependence of (a) self-diffusivity and (b) ionic conductivity at 1200 and 400 K.

4.5 Conclusions

In this chapter, we studied the diffusion and conduction of lithium garnet oxides $Li_xLa_3Zr_{x-5}Ta_{7-x}O_{12}$ (x = 5, 6, 6.5, 6.75, and 7) with MD simulations based on a machine learning interatomic

potential (MLIP). We found that this MLIP is approaching DFT accuracy in force error. It is more

accurate than other commonly applied models such as Core, induced dipole (ID), and DFTB and

predicts diffusion and conduction properties that agree with single crystal experimental data much

better than the other three models, when using $Li_6La_3ZrTaO_{12}$ as a model material. This MLIP also

produces self-diffusivity and ionic conductivity values agreeing with experimental data across the

x composition range. Examination of computational and experimental ionic conductivities suggest that the temperature dependence is non-Arrhenius which can be fitted to a Vogel-Tammann-Fulcher equation with Vogel temperature below room temperature. Examination of computational and experimental values together also suggests that the maximum room-temperature conductivity occurs between x=6.6 to 6.8 with the precise composition depending on $Al/H_2O/CO_2$ contamination, Li loss, grain boundary, density, etc.

CHAPTER 5 Grain boundary contributions to Li-ion transport in Li$_7$La$_3$Zr$_2$O$_{12}$

5.1 Motivation

Like other oxide-based solid electrolytes, most of the synthesized lithium garnet samples are generally polycrystalline consisting of a large number of grains separated by grain boundaries (GBs). Although Li garnet oxides have been considered as one of the most promising solid electrolytes due to their chemical stability and high ionic conductivity, their practical application has been hindered by the GBs. After the first report of lithium garnet oxide Li$_5$La$_3$M$_2$O$_{12}$ (M=Nb, Ta)[39], there has been extensive research to improve its ionic conductivity.

Experimentally, the ionic conductivity of Li garnet oxides is commonly measured using electrochemical impedance spectroscopy (EIS). **Figure 32** shows a typical Nyquist plot of Li$_7$La$_3$Zr$_2$O$_{12}$ (named Li$_7$ afterward) at 18 °C[139]. The left depressed semicircle in high frequency represents the bulk resistance (R_b), the right one represents the GB resistance (R_{gb}), and the slope line represents the blocking effect of Au paste on the Li$^+$ motion. The solid line represents the fitted data based on an equivalent circuit model of $(R_b Q_b)(R_{gb} Q_{gb})(Q_{et})$, where Q_b, Q_{gb}, and Q_{et} are the constant phase element (CPE) contributions of R_b, R_{gb}, and electrode. It is observed that the contribution of GB to the ionic conductivity is about 44 %, which highly reduces the total ionic conductivity of the material. This characteristic has also been found in some other oxide SEs[140-143].

Even though only a few works have been done to study the effect of the GBs on the transport in Li$_7$, there are some conflicting conclusions. Yu et.al. first performed MD simulations of three symmetric tilt GB structures using a Core model with IP based on Morse-type interactions derived from softBV bond valence[144]. Shiiba et al. also performed Core model MD simulations using Buckingham potential with partial charge[145]. In addition to the symmetric GBs, they also

studied GBs with mixed GB planes. Both of these two research groups found that GBs retard the Li$^+$ diffusion. The difference is Yu et al. et al believe that higher energy GBs penalize the ionic conductivity to a greater degree whereas Shiiba et al. proposed the opposite conclusion. Recently, Gao et al. studied the GB effects via DFT-MD[146]. In contrast to both Yu and Shiiba et al., Gao et al. found that GB can also increase ionic conductivity. Based on the discrepancy, it is important and meaningful to employ our newly developed MLIP to study the GB contribution in the transport of lithium garnet oxides.
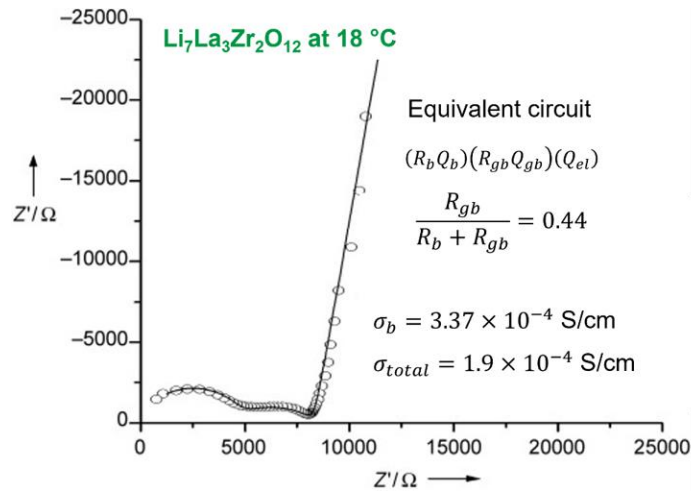

Figure 32 Impedance plot of Li$_7$La$_3$Zr$_2$O$_{12}$ measured in air at 18 °C. The open circles are experimental values and the solid line represents the fitted data based on the equivalent circuit of $(R_bQ_b)(R_{gb}Q_{gb})(Q_{el})$[139].

5.2 Computational details

5.2.1 MLIP potential

After comparing our MLIP-MD results with the experiments from the works of literature in Chapter 4, we have found that our newly developed MLIP provides reliable predictions for the properties of lithium garnet oxides, making it a valuable tool for further research, e.g., GB effect in lithium garnet oxides. It should be mentioned that the MLIP used in this chapter was trained from Li$_7$ to study the GBs of Li$_7$, named MLIP-Li$_7$. The force error of MLIP-Li$_7$ for each species

and all the atoms and virial error for all the atoms against DFT are shown in **Figure 33**. The force error of La, Zr, O, and Li is 0.11, 0.17, 0.10, and 0.05 eV/Å, respectively, with an overall error of 0.10 eV/Å. The virial error is 0.19 GPa. The force and virial error are slightly smaller than the values of MLIP (0.11 eV/Å and 0.22 GPa, see **Table 8**) obtained from the training set of Li_5, Li_6, and Li_7, suggesting the potential is reliable.
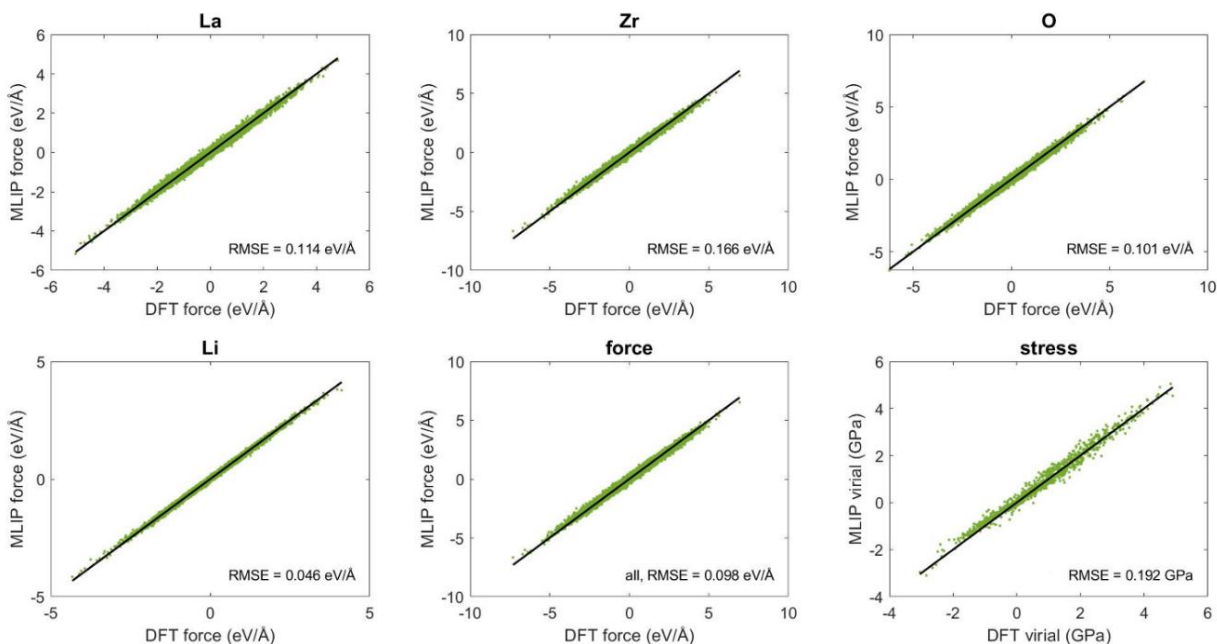

Figure 33 The comparison of atomic forces and cell virials between MLIP-Li_7 (scatter points) against DFT (black lines) for $Li_7La_3Zr_2O_{12}$.

To test the performance of MLIP-Li_7, we used it to run MD simulations of Li_7 within NPT ensembles and compared the lattice parameters with the results obtained from MLIP presented in Chapter 4, as shown in **Figure 34**a. There is a negligible difference in the values and the same tetragonal-cubic phase transition temperature, which is around 1000 K. Note that, in Chapter 4, we performed NVE instead of NVT ensemble, therefore we conduct NVT ensemble using both potentials and extracted the ionic conductivity of Li_7, as shown in **Figure 34**b. It can be seen that the values are almost identical, the ionic conductivity decreases dramatically as a tetragonal phase,

and the activation energy of MLIP-Li7 is 1.24 and 0.15 for the tetragonal and cubic phases, respectively, which are very close to the values of MLIP. This confirms that MLIP-Li7 is reliable and appropriate to be applied to study the GB effect on the transport of Li7.
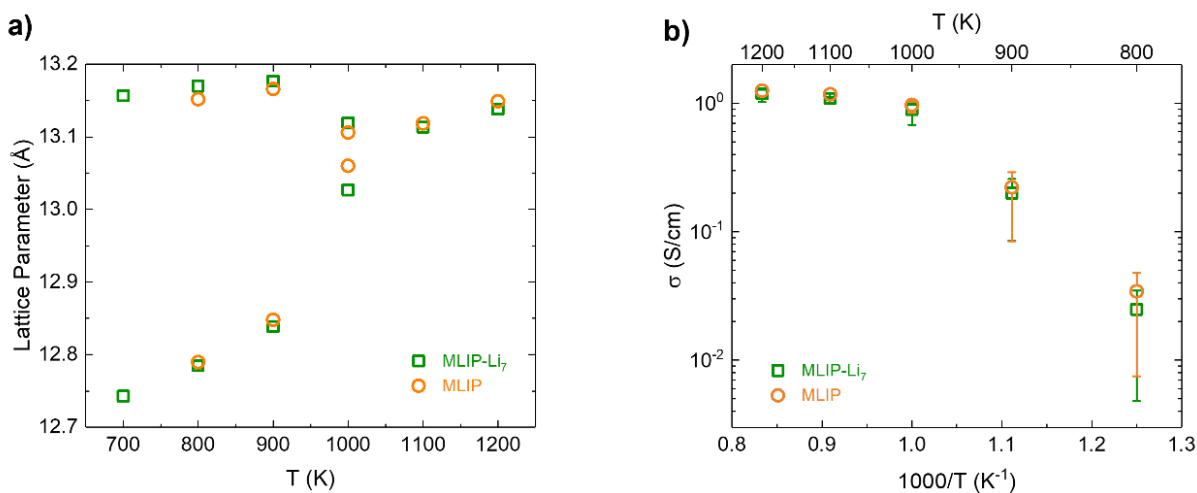

Figure 34 (a) Lattice parameter and (b) ionic conductivity of $Li_7La_3Zr_2O_{12}$ extracted from MLIP and MLIP-Li7 based MD trajectories.

5.2.2 GB structure construction

The initial GB structures were constructed using the software Materials Studio. Three symmetric tilt grain boundary geometries with low-order coincidence site lattices (CSL), i.e., Σ 1(110), Σ3(112), and Σ5(310), have been studied for Li7. The selection of symmetric tilt GBs studied in this work was based on the low-energy GB orientation in BCC metals [147, 148]. As symmetric GB is a special case in the plane defect, for comparison, we have also studied the mixed GB structure formed by planes (110) and plane (211) (named mixGB(110)(211) afterward). The structural parameters of all the GB structures studied in this chapter are listed in **Table 9**. **Figure 35** illustrates the initial structures of the GB models using relatively smaller structures. As Zr occupies the BCC-type sublattice, each model was provided with a structure that only contains Zr atoms to illustrate the coincident-site nature of the GB model. It can be seen that there are two GB

planes in each GB structure, one is in the center of the structure along the *a*-axis, and the other one

is at the *a*-axis's boundary.

Table 9 Lattice parameters, number of atoms, and number of formula units of each GB structure.

| Structure model	a (Å)	b (Å)	c (Å)	No. of atoms	No. of unit cells of Li_7
Σ1(110)-4nm	73.95	26.21	18.54	3072	16
Σ3(112)-3nm	64.13	37.07	22.70	4608	24
Σ5(310)-4nm	84.94	26.21	41.44	7680	40
mixGB(110)(211)-3nm	69.70	24.46	37.07	5376	28
Σ3(112)-5nm	96.23	37.07	22.70	6912	36
Σ3(112)-10nm	192.54	37.07	22.70	13824	72
Σ1(110)-9nm	185.16	26.21	37.07	15360	80
Σ5(310)-8nm	165.77	26.21	41.45	15360	80
mixGB(110)(211)-9nm	191.00	24.46	37.07	14592	76
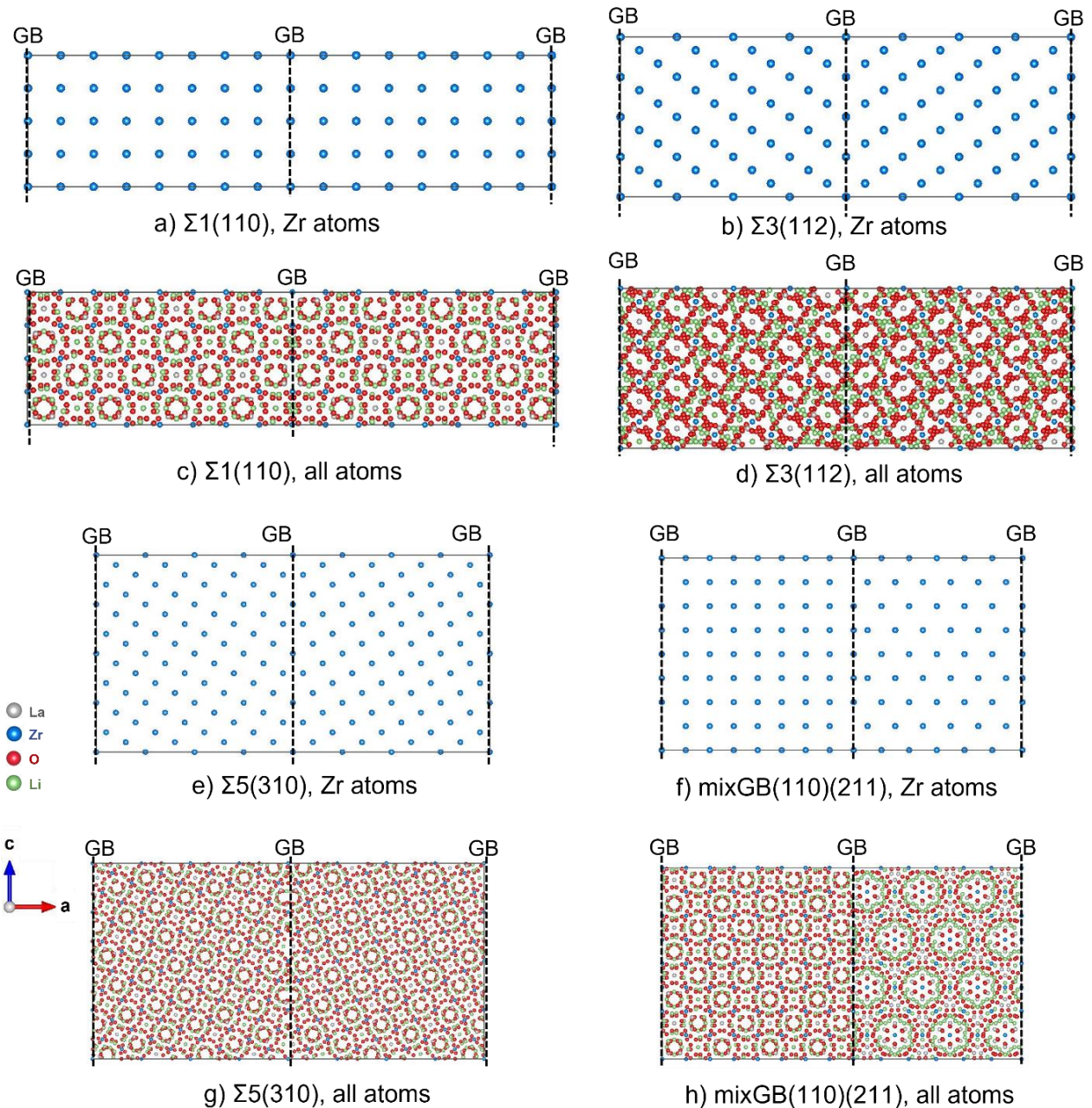
Figure 35 Initial structures of three symmetric tilt GBs, i.e., (a, c) Σ1(110), (b, d) Σ3(112), and (e, g) Σ5(310), and one mixed GB structure, i.e., (f, h) mixGB(110)(211). As Zr occupies the BCC-type sublattice in $Li_7La_3Zr_2O_{12}$, (a, b, e, and f) show the GBs with only Zr atoms. The GB interfaces are guided by the dotted lines. There are two GB planes in each GB structure, one is in the center of the structure along the a-axis and one at the *a*-axis's boundary.

5.2.3 MD simulations

The training data is collected from DFT-MD trajectories of Li_7 with energy, force, and cell-virial, therefore the potential will be named MLIP-Li_7 afterward to differentiate from the MLIP trained from the reference data set of Li_5, Li_6, and Li_7 in Chapter 3. Details of training can be found in Chapter 4. Geometry optimization and MD simulations were both performed using LAMMPS. MD simulations were conducted in the temperature range of 700 - 1200 K. NPT ensemble simulation was performed to obtain the lattice parameters. The timestep was 1 fs, thermostat and barostat relaxation time were set to 0.1 and 0.5 ps, respectively. The NVT ensemble was performed to extract the transport behavior. The trajectory length is from 100 ps – 20 ns depending on the temperature.

5.3 Results and discussions

5.3.1 Grain boundary energy

After the geometry optimization, we performed NPT of GB structures at a temperature range of 700 – 1200 K and calculate the GB formation energy. The evolution of the total energy of each GB structure at different temperatures is shown in **Figure 36**. The average of the equilibrate states was used to calculate the GB formation energy at this temperature.

Figure 37 summarized the GB formation energies as a function of temperature for both symmetric and asymmetric GB structures. It can be seen that the fluctuation of each GB structure at different temperatures is very small. The mixed GB structures exhibit 2 – 3 times higher GB formation energy than the symmetric GB structures. For symmetric GBs, $\Sigma3(112)$ has the lowest GB energy while $\Sigma5(310)$ has the highest GB energy, which is consistent with the results from the classic IP model simulations[144, 145].
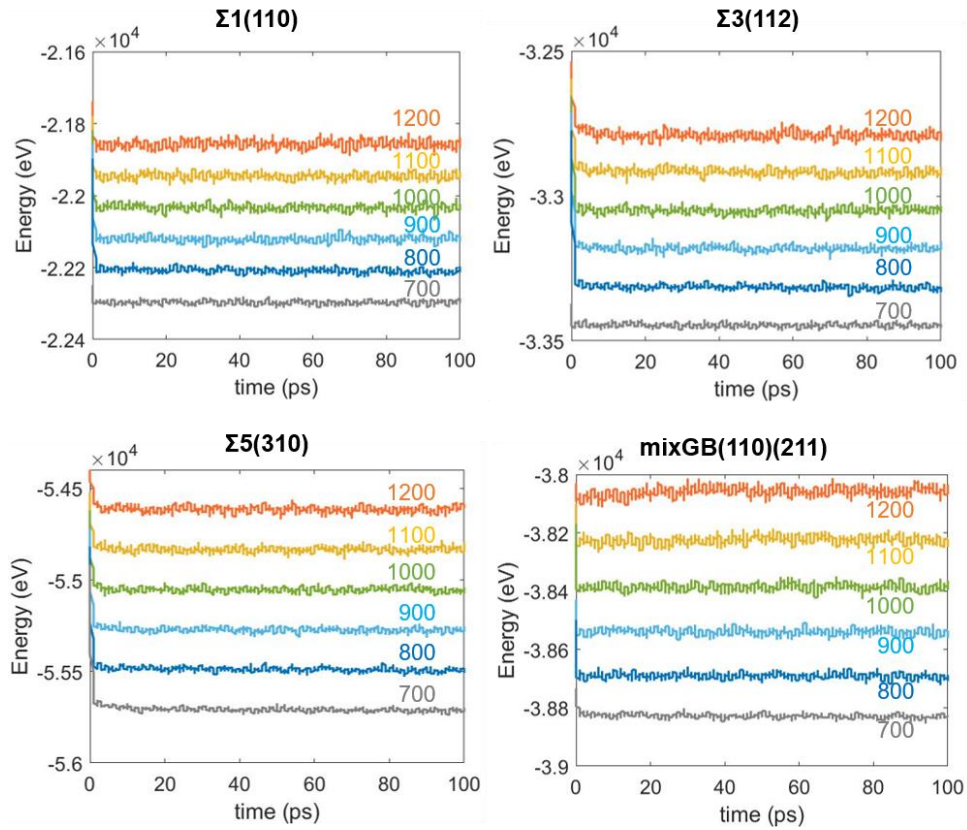
74

Figure 36 Total energy evolution of GB structures Σ1(110), Σ3(112), Σ5(310) and mixGB(110)(211) at a temperature range of 700 - 1200 K.
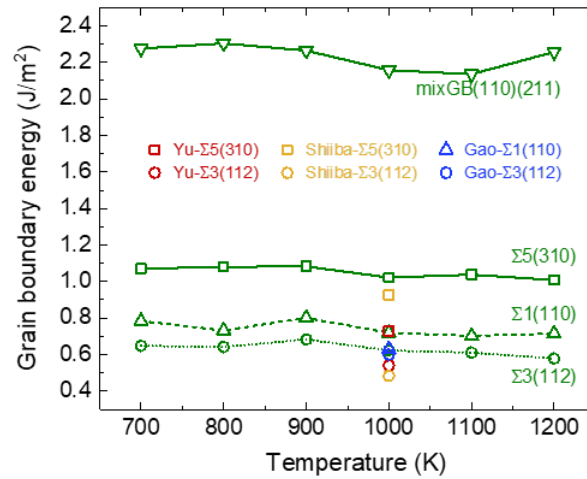

Figure 37 GB energy as a function of the temperature for both symmetric and mixed GB structures. The literature values from Yu[144], Shiiba[145], and Gao[146] are shown for comparison.

5.3.2 Grain boundary composition

In order to compare the properties between the GB and the bulk regions in the GB structures, we performed MD simulations using the larger cell for each GB structure shown in **Table 9**. **Figure 38** compares the nominal composition and the average composition from NVT 800 K for each GB structure. We divided the supercells into several bins along the a-axis (normal to the GB plane) and calculated the number of each species in each bin. For symmetric GBs, the average number of Zr in each bin is still the same, whereas the average composition of La is different in different GBs, i.e., uniform in $\Sigma3(112)$ but reduced in the GB region of $\Sigma1(110)$ and $\Sigma5(310)$. In addition, the number of Li and O reduces in the vicinity of the GB compared to the bulk region for all the GBs, forming an 'M', suggesting that there is a reduction of Li and O at the GBs. The reduction of Li population at the GBs suggests that Li deficient sites formed at the GB. This is consistent with the observation from Shiiba et al. [145] who also calculated the population of Li atoms at the GB and believed that the trapping Li vacancies formed at the GB[145]. However, it is different from the calculation from Yu et al.[144] as they found there is Li and O accumulation at the GBs and suggested that the cosegregation of Li and O forms a new phase of Li_2O[144]. Gao et al. calculated the Li interstitial formation energy using DFT-MD and also found there is Li accumulation at the GBs[146]. On the other hand, for mixed GB structure mixGB(110)(211), Li and O atoms tend to accumulate in the bulk of grain (211).
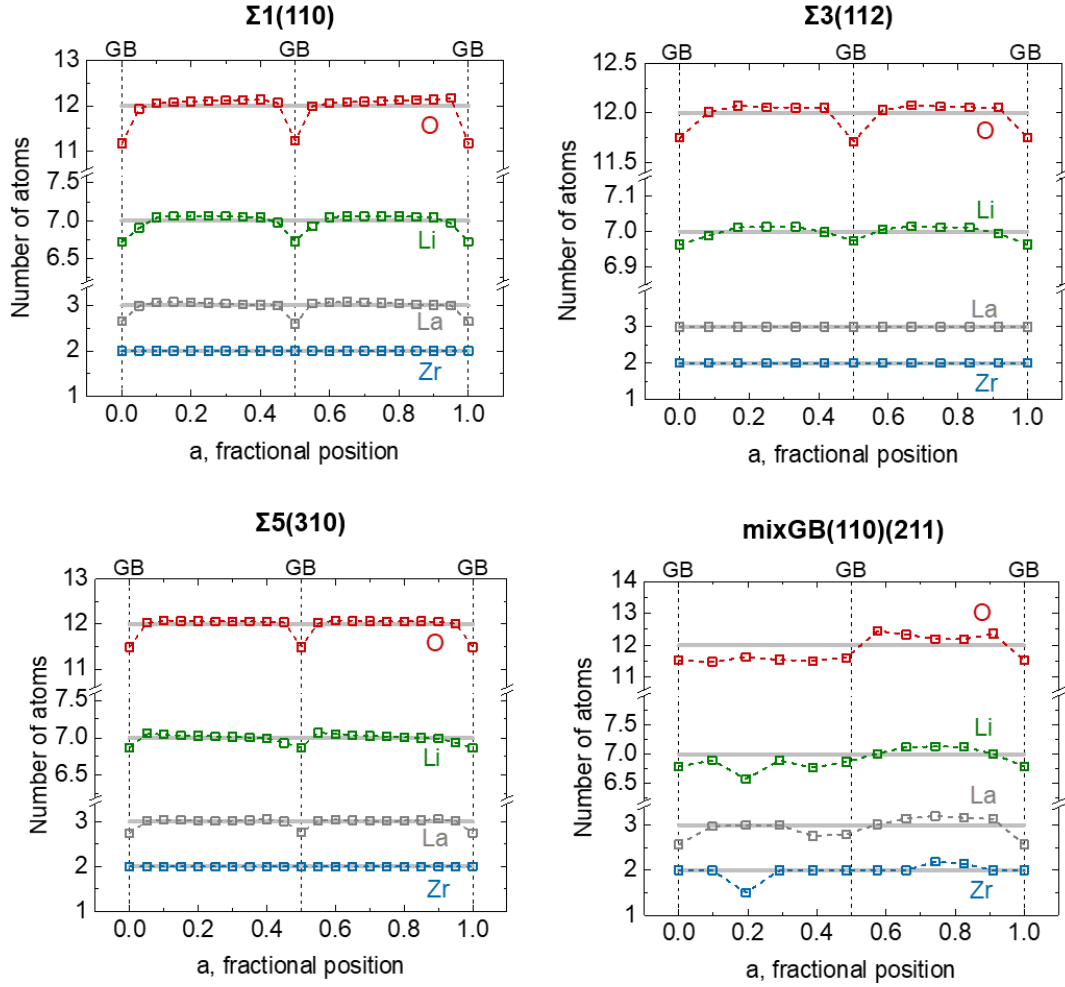
Figure 38 Atom numbers of Li, La, Zr, and O as a function of position normal to the GB plane (a-axis). The light solid gray lines represent the nominal composition and the colorful dashed lines with symbols represent average structures at 800 K.

5.3.3 Charge

With the obtained composition in **Figure 38** and the DDEC6 charge in **Table 6**, we calculated the average charge in each bin for GB structures at 800 K. Both Σ3(112) and Σ5(310) exhibit charge accumulation at the GBs, the width of this space charge area is around 3 nm. However, this characteristic has not been found in Σ1(110) and mixGB(110)(211), where the space charge region spans the whole cell.
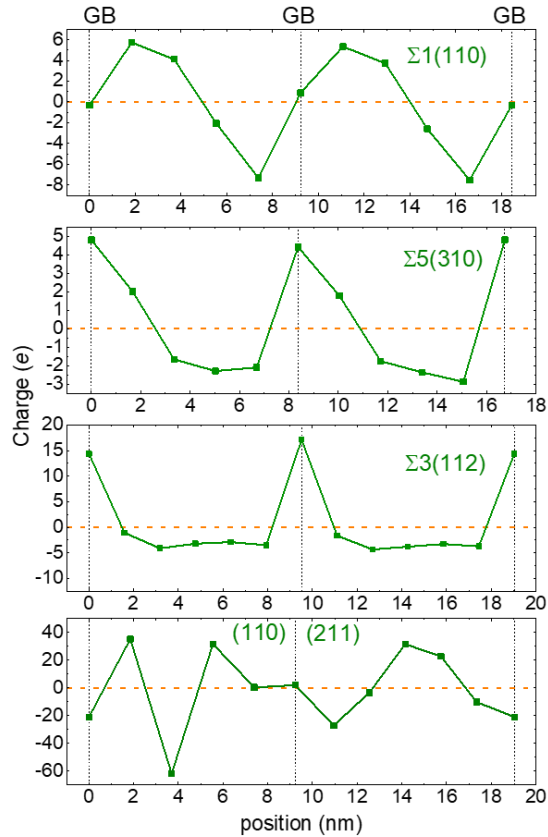
Figure 39 Average charge as a function of position normal to the GB plane (x-axis) of MD 800 K for GB-containing structures.

5.3.4   Ionic conductivity

For ionic conductivities, we first studied the grain size effect by comparing three different grain sizes of the Σ3(112) model. The grain length along the b and c axis (along the GB plane) are the same, whereas it is different along the a-axis (normal to the GB plane), which are 3.21, 4.81, and 9.63 nm named as 3, 5, and 10 nm, respectively (see **Table 9**). **Figure 40** compares the ionic conductivity of these three models with the bulk Li_7 in two perpendicular directions separately. Again, crystal Li_7 has a tetragonal-cubic phase transition at 1000 K. Above this temperature, the ionic conductivities of the GB structures are lower than that of the bulk, while under this temperature, it is vice versa. Based on the width of GB area (as shown in the density map later) and the ionic conductivity of bulk Li_7 from **Figure 34**, we calculated the local ionic conductivity

of $\Sigma 3(112)$ of different grain size at 1000 K, as shown in **Figure 40**c. It indicates that the grain size

has a significant effect on the behavior of GBs with respect to Li-ion transport. The GB structure

with the biggest grain size behaves more like the bulk material in both directions, confirming that

GB models with small grain sizes overestimate the GB effect of the Li-ion transport in the material.
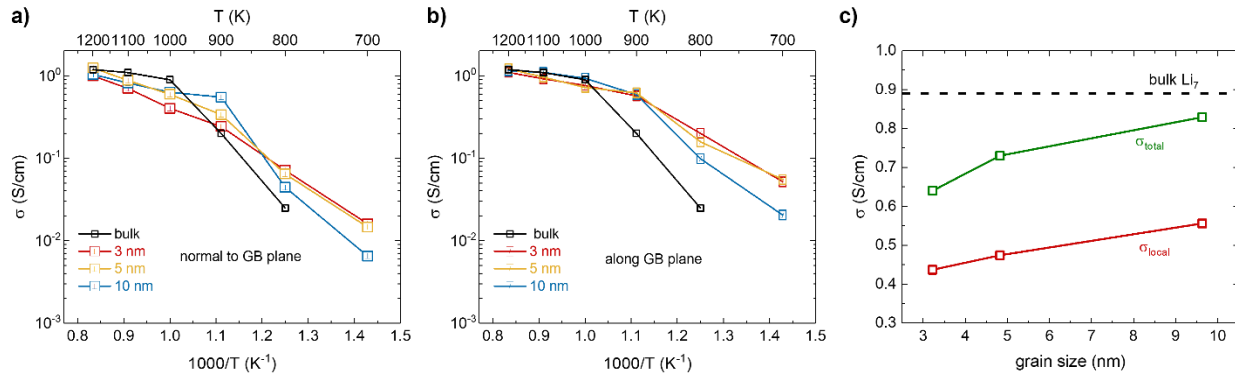

Figure 40 Ionic conductivity as a function of the temperature of different grain sizes of $\Sigma 3(112)$. (a) normal to and (b) along the GB plane. (c) ionic conductivity as a function of grain size.

Figure 41a-d shows the ionic conductivity of different GB structures along and normal to

the GB plane. The smallest cell size for each GB structure in **Table 9** was used to clearly see the

GB effect. It can be seen that $\Sigma 3(112)$ exhibits obvious anisotropic characteristics especially when

temperature decreases. The ionic conductivity normal to the GB plane is much lower than that

along the GB plane, and it is almost four times lower at 700 K. This observation is consistent with

the analysis from Yu et al.[144] and Shiiba et al.[145] while completely opposite to the conclusion

from Gao et al. where $\Sigma 3(112)$ exhibits a high intergranular diffusion[144]. $\Sigma 1(110)$ exhibits

similar behavior with a small difference between these two perpendicular directions. However,

$\Sigma 5(310)$ shows an almost isotropic characteristic at high temperatures, and interestingly, the ionic

conductivity normal to the GB plane is even slightly lower. For the mixGB(110)(211), it shows an

anisotropic behavior with lower ionic conductivity normal to the GB plane. **Figure 41**e-f compared

the ionic conductivity of each GB structure normal to the GB plane and along the GB plane,

79

respectively. First, the mixGB(110)(211) exhibits an obviously lower ionic conductivity at high temperatures in both directions, and it is vice versa at low temperatures. For symmetric GBs, the conductivity normal to the GB plane increases with increasing GB energy, i.e., $\Sigma3(112)$ to $\Sigma1(110)$ and to $\Sigma5(310)$. There is no direct correlation between conductivity along the GB plane with the GB energy, but $\Sigma5(310)$ shows the smallest value.

Figure 41g compared the average ionic conductivity of different GB structures with the bulk. For symmetric GBs, there is a kink between 900 and 1000 K. At the temperature range of 1000 – 1200 K, the ionic conductivities of all the GB structures are smaller than the bulk, suggesting that the ionic conductivity degrades at the GBs in the cubic phase. At the temperature range of 700 – 900 K, the ionic conductivities of all the GB structures are higher than the bulk, suggesting that the existence of GB changes the transport properties in the tetragonal phase. The activation energies of $\Sigma3(112)$, $\Sigma1(110)$, and $\Sigma5(310)$ at high temperatures are 0.26, 0.17, and 0.20 eV, respectively, which are all higher than the bulk (0.15 eV), while activation energies at low temperatures are 0.63, 0.70, and 0.51 eV, respectively, which are lower than the bulk (1.24 eV). The activation energy difference between high and low temperatures is not observed in the literatures, and therefore only one value of activation energy was presented for each GB structure, as listed in **Table 10**. Interestingly, the ionic conductivity of mixGB(110)(211) shows an Arrhenius behavior with an activation energy of 0.29 eV. Overall, for symmetric GBs in the cubic phase, the higher the GB formation energy, the higher the ionic conductivity and smaller activation energy, and vice versa. This is consistent with the conclusion from Shiiba et al.[145] but opposite to that from Yu et al.[144, 145].
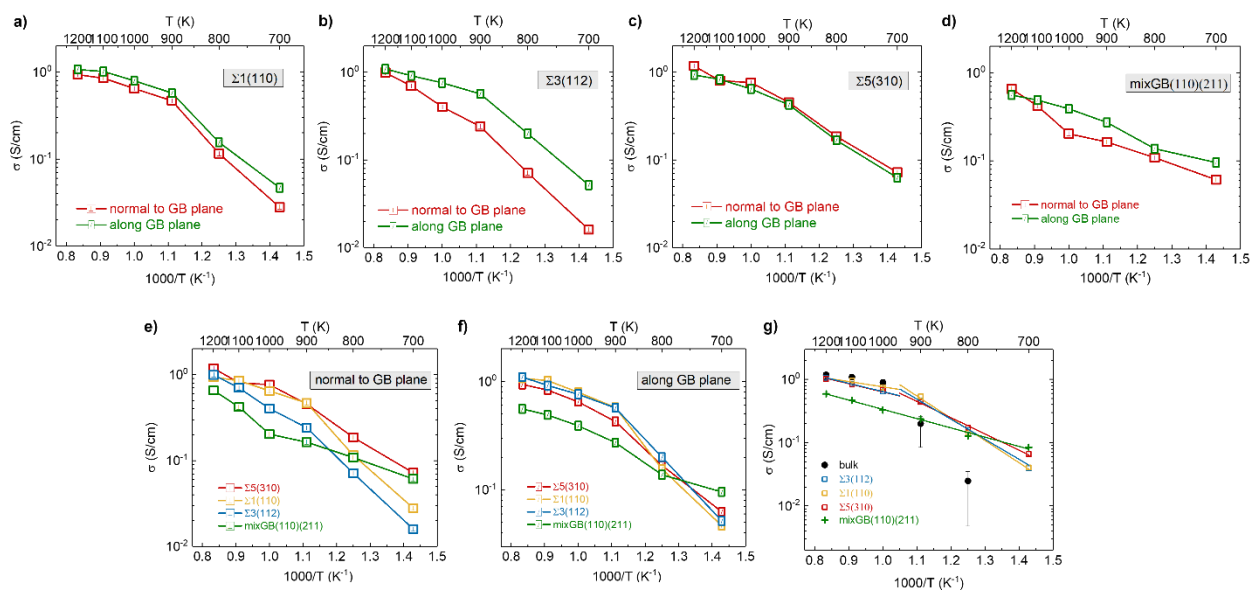
Figure 41 Comparison of ionic conductivity between normal to and along the GB plane for GB structures (a-d) Σ1(110), Σ3(112), Σ5(310), and mixGB(110)(211). (e-f) Comparison of ionic conductivity among different GB structures normal to and along the GB plane, respectively. (g)Comparison of average ionic conductivity of each GB structure with bulk material. Solid lines are Arrhenius fit. Error bars of the bulk structure represent the ionic conductivity in the *ab* and *c* directions in the tetragonal phase.

Table 10 Activation energy, Ea (eV), of current work and literatures [144-146]. Activation energies of high T are calculated from 1000 – 1200 K for all the structures, and of low T from 700 – 900 K for the GB structures and 800 – 1000 K for the bulk. The GB energy was obtained by averaging over 700 – 1200K.

Structures	GB energy (J/m^2)	Current work		Yu (Core)	Shiiba (Core)	Gao (DFT)
		High T	Low T			
bulk	—	0.15	1.24	0.52	0.18	0.25
Σ1(110)	0.74	0.17	0.70	—	0.32	0.49
Σ3(112)	0.63	0.26	0.63	0.52	0.41	0.20
Σ5(310)	1.05	0.20	0.51	0.64	0.31	—
mixGB(110)(211)	2.23	0.29		—	—	—

5.3.5 Nuclear density map

Figure 42 and **Figure 43** show nuclear density maps of Li-ions with an isosurface level of 0.2 Å^{-3} viewed from along the GB plane (i.e., along the b-axis) of different GB structures at temperatures of 1000 and 800 K, respectively. These maps provide a visualization of the pathway

of atoms by dividing the supercell into voxels with a length of roughly 0.1 Å and calculating the probability density of each type of atom in each voxel. The figures show that the GB structures exhibit different characteristics in the vicinity of the GB compared to the bulk area. The widths of the GB area of $\Sigma 1(110)$, $\Sigma 3(112)$, $\Sigma 5(310)$, and mixGB(110)(211) at 1000 K are approximately 1.61, 1.22, 1.86, and 1.89 nm, respectively, as indicated by the black dash frame. These widths are consistent with the results from Tenheff et al.[149], who synthesized Li_7 pellets using the hot-pressed technique and observed a grain boundary width of ~2 nm in pellets with a relative density of 98% and a grain size of 5 μm. According to **Figure 43**, all the GB structures exhibit a more discontinuous network for Li in both GB and the bulk areas due to the lower thermal energy at 800 K compared to 1000 K. Moreover, the width of the GB area at 800 K is slightly longer than that at 1000 K, which is around 2 nm.

The first two GBs, $\Sigma 1(110)$ and $\Sigma 3(112)$, show a clear discontinuity along the a-axis (normal to the GB plane), implying that the ionic conductivity in this direction is low, which could be attributed to the fact that Li-ions require high energy to diffuse across the GB plane. Consequently, the overall ionic conductivity in the GB region is reduced. This behavior is illustrated in **Figure 41**a-b and **Figure 41**d. On the other hand, $\Sigma 5(310)$ exhibits a discontinuity along both the a- and c-axes, which explains the relatively small difference in ionic conductivity along and normal to the GB plane, as shown in **Figure 41**c. Finally, mixGB(110)(211) also displays a discontinuity along the a-axis, which suggests that the ionic conductivity in this direction is low as well, leading to reduced overall ionic conductivity in the GB region, as shown in **Figure 41**f.

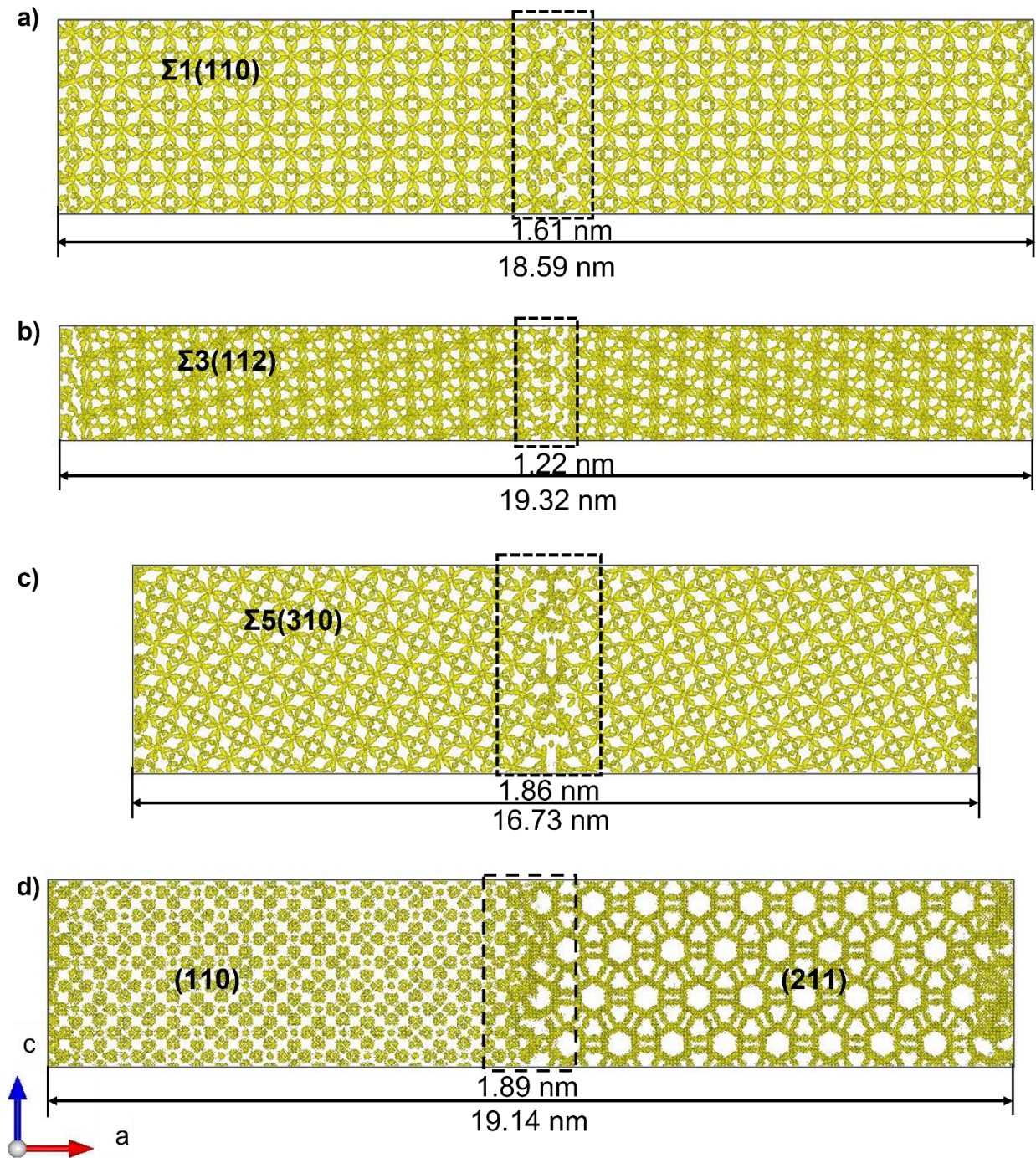**Figure 42** Li nuclear density map of (a-d) Σ1(110), Σ3(112), Σ5(310), and mixGB(110)(211) derived from MD trajectories at 1000 K with an isosurface level of 0.2 Å^{-3}.
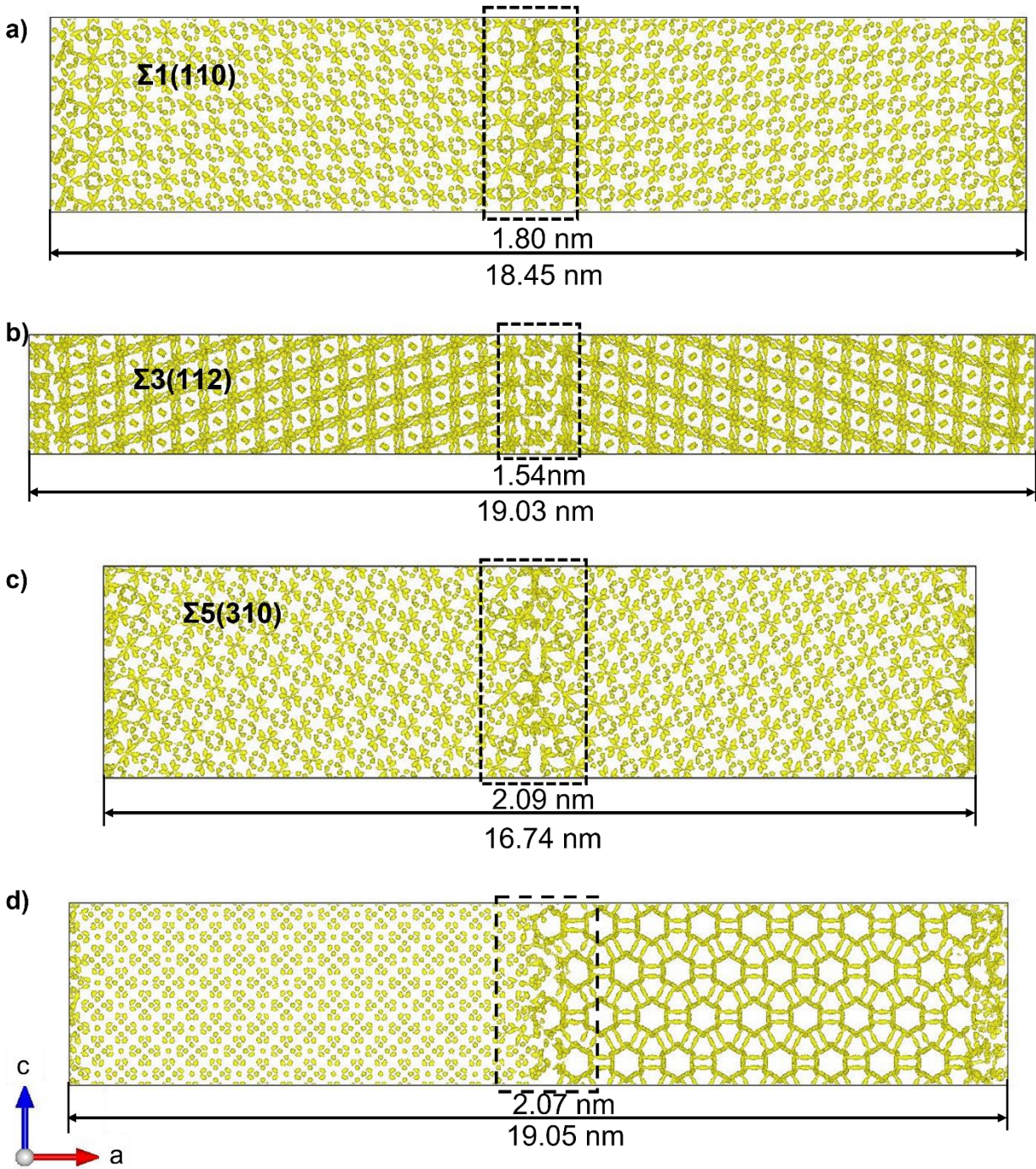
Figure 43 Li nuclear density map of (a-d) Σ1(110), Σ3(112), Σ5(310), and mixGB(110)(211) derived from MD trajectories at 800 K with an isosurface level of 0.2 Å^{-3}.

5.3.6   Self-diffusivity

Figure 44 compares the self-diffusivity of Li-ions in bulk Li_7 and GB-containing structures at 1000 K. The figure uses boxplots to illustrate the range, median, and quartiles of diffusivity values, with the boxes representing the interquartile range (IQR) and the whiskers extending to the minimum and maximum values that fall within 1.5 times the IQR. The black boxes represent the average diffusivity in the a, b, and c directions, while the green and orange boxes represent the diffusivity along and normal to the GB plane, respectively. Outliers beyond the range of 1-99% values are marked with open circles.
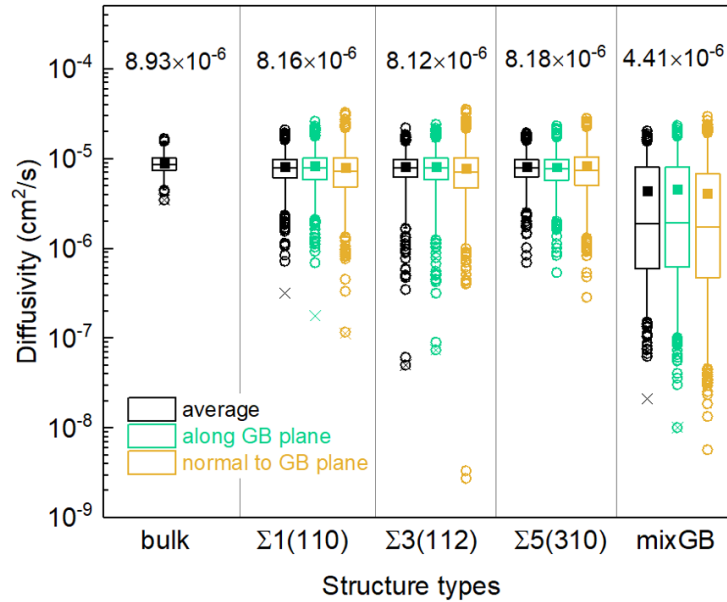
Figure 44 Boxplots of Li-ion self-diffusivity of bulk $Li_7La_3Zr_2O_{12}$ and GB-containing structures at 1000 K.

The figure shows that the bulk Li_7 has the highest average self-diffusivity, which is expected since there are no GBs to hinder the movement of ions. In contrast, the mixGB(110)(211) structure has the lowest average self-diffusivity and a larger range of box and whisker compared to the symmetric GB structures. Among the symmetric GB structures, $\Sigma3(112)$ shows a longer whisker than the other two, suggesting a wider range of self-diffusivity values. The diffusivity

normal to the GB plane has a larger range and longer whisker compared to that along the GB plane, and the average diffusivity normal to the GB plane is generally smaller than that along the GB plane, except for Σ5(310). This observation is consistent with the conclusion drawn from **Figure 41**, which showed that Σ1(110) and Σ3(112) exhibit anisotropic diffusion, while Σ5(310) exhibits isotropic diffusion.

Figure 45 shows the scatter plots of structures extracted from MD trajectories over a time period of 2 ns at a temperature of 1000 K for the fastest and slowest 0.5% Li ions in terms of average diffusivities shown in **Figure 44**. In the case of symmetric grain boundaries, the slowest-moving Li-ions appear to be confined to the boundary itself, while the fastest-moving ions are located in the bulk area and move around freely. However, in the case of mixed GBs, the behavior of the Li-ions appears to be dramatically different. Specifically, the fastest-moving 0.5% of ions are found exclusively in one type of grain (211), while the slowest-moving 0.5% of ions are found exclusively in another type of grain (110). This is likely to be related to reduced Li content in the (110) grain shown in **Figure 38**.
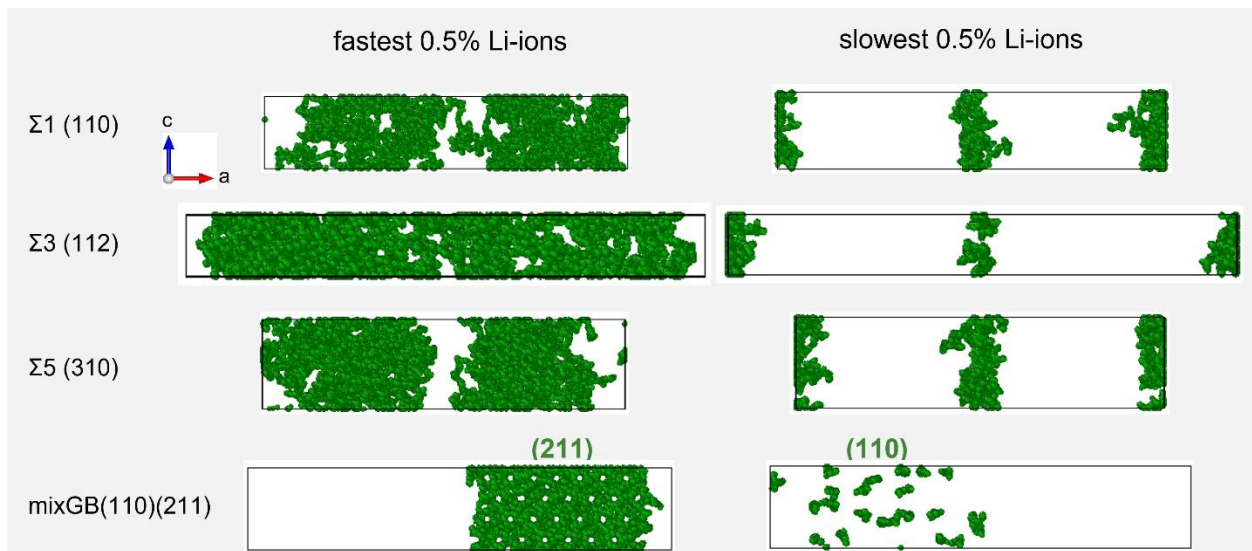

Figure 45 Scatter plots of structures extracted from the MD trajectories over 2 ns at 1000 K for the fastest and slowest 0.5% Li-ions.

5.4 Conclusions

In this chapter, the effects of GB on lithium garnet oxide $Li_7La_3Zr_2O_{12}$ were comprehensively studied. It was found that the existence of GBs significantly affects the composition and Li^+ transport behavior in the vicinity of GBs regardless of the grain orientation and GB types. Firstly, the GB effect is strongly associated with the grain size, the GB-contained structures act more like bulk materials as grain size increases. Secondly, it shows that the GB effect depends on the crystal phase of the lithium garnet oxide. At high temperatures the bulk of Li_7 is a cubic phase, the structure with the high GB formation energy delivers lower ionic conductivity. Especially, the ionic conductivity is significantly reduced at randomly mixed GBs compared to symmetric GBs. However, at low temperatures the bulk of Li_7 is a tetragonal phase, the existence of the GB changed the ordered structure in the bulk area and increased the total ionic conductivity of the structure.

CHAPTER 6 Dissertation conclusions and future work

6.1 Dissertation conclusions

Lithium garnet oxides are a family of promising candidates for all-solid-state Li-ion batteries. In this thesis, we studied Li-ion self-diffusion and coherent ionic conduction of $Li_xLa_3Zr_{x-5}Ta_{7-x}O_{12}$ (x=5-7) using MD simulations. We applied several IP models including Core, CS, ID, and MLIP models as well as a DFTB model. The DFTB model has high accuracy but is still too slow to study complex systems with thousands of atoms. Overall, we think the ID model combined with the force-matching approach is the most advanced physical IP model as it includes the polarization through atomic polarizability and takes from first-principles results as the input. On the other hand, MLIP is a pure mathematic model approaching DFT accuracy in force error. Both of these two models can study the lithium garnet oxides and even complex GB systems, in the meanwhile, they are 2 to 3 orders of magnitude faster than DFT.

In terms of which composition has the maximum ionic conductivity, there are some different conclusions in experimental works, which could be induced by the contamination of the sample from the alumina crucible, low relative density, grain boundary defects in the polycrystalline, and uncertainty of the composition from arbitrarily amount of extra Li added to compensate for the Li loss in the preparation process. However, there is no such issue in computational simulations, which enables the accuracy of the results. Our MLIP-MD simulations reveal that the maximum room-temperature conductivity occurs between x=6.6 to 6.8. Besides, temperature-dependent ionic conductivity shows the Vogel-Tammann-Fulcher (VTF) equation should be used to fit the data and extract the ionic conductivity at room temperature instead of the Arrhenius fit.

As most of the samples are polycrystalline, the effect of grain boundary is significantly important, and in-depth research is imperative. According to the GB models we built, including both symmetric and mixed ones, the Li-ion migration is hindered at the GBs despite the type of GBs at high temperatures for Li_7 where the bulk material is a cubic phase. Specifically, the mixed GB with higher GB formation energy penalizes Li-ion conduction more than the symmetric GBs with lower GB formation energies. Our model also reveals that the contribution of GB in Li-ion transport along and normal to the GBs is dependent on the type of grain orientation. Besides, the grain size plays an important role in the conductivity too, the bigger the grain size the higher the ionic conductivity.

6.2 Future work

Due to the cubic-tetragonal phase transition of Li_7, it is virtually impossible to study the GB influence in Li_7 at room temperatures through MD simulations directly. Based on our MD simulations, $Li_{6.5}$ is a cubic phase and has relatively higher ionic conductivity in lithium garnet oxide families, thus it is essential to study the GB influence on the ionic conductivity of $Li_{6.5}$ under the guidance of our preliminary work of Li_7.

In this thesis, we studied the diffusion and conduction in lithium garnet oxides at the temperature range of 400 – 1200 K through MD simulations and extrapolate the ionic conductivity at low temperatures using VTF equation. However, there is another method can be tried to investigate the dynamics of Li-ions at low temperatures directly, i.e., kinetic Monte Carlo, which approximates the transport of Li-ion as a sequence of discrete 'hops' between distinct lattice sites[150].

As lithium garnet oxides are electrochemical stable with Li metal which enables the Li metal to be used as a negative electrode, the computational study of the interface between the

garnet/Li metal has attracted much attention[151-153]. However, as far as we know, there is no

report of the study using MLIP, which makes it worth using our MLIP model to study the interface

properties.

BIBLIOGRAPHY

[1]   I. E. Agency. Available: https://www.iea.org/reports/world-energy-outlook-2022

[2]   B. Dunn, H. Kamath, and J. M. Tarascon "Electrical Energy Storage for the Grid: A Battery of Choices." *Science* **2011***,* 334, 928-935. http://dx.doi.org/10.1126/science.1212741

[3]   G. L. Soloveichik, "Battery Technologies for Large-Scale Stationary Energy Storage," in *Annual Review of Chemical and Biomolecular Engineering, Vol 2*. vol. 2, J. M. Prausnitz, Ed., ed Palo Alto: Annual Reviews, 2011, pp. 503-527.

[4]   W. E. Council. Available: www.worldenergy.org

[5]   A. Afir, S. M. H. Rahman, A. T. Azad, J. Zaini, M. A. Islan, and A. Azad "Advanced materials and technologies for hybrid supercapacitors for energy storage - A review." *Journal of Energy Storage* **2019***,* 25, 24. http://dx.doi.org/10.1016/j.est.2019.100852

[6]   J. M. Tarascon and M. Armand "Issues and challenges facing rechargeable lithium batteries." *Nature* **2001***,* 414, 359-367. http://dx.doi.org/10.1038/35104644

[7]   M. Armand and J. M. Tarascon "Building better batteries." *Nature* **2008***,* 451, 652-657. http://dx.doi.org/10.1038/451652a

[8]   J. B. Goodenough and Y. Kim "Challenges for Rechargeable Li Batteries." *Chemistry of Materials* **2010***,* 22, 587-603. http://dx.doi.org/10.1021/cm901452z

[9]   B. Scrosati and J. Garche "Lithium batteries: Status, prospects and future." *Journal of Power Sources* **2010***,* 195, 2419-2430. http://dx.doi.org/10.1016/j.jpowsour.2009.11.048

[10]   V. Etacheri, R. Marom, R. Elazari, G. Salitra, and D. Aurbach "Challenges in the development of advanced Li-ion batteries: a review." *Energy & Environmental Science* **2011***,* 4, 3243-3262. http://dx.doi.org/10.1039/c1ee01598b

[11]   S. Ramakumar, C. Deviannapoorani, L. Dhivya, L. S. Shankar, and R. Murugan "Lithium garnets: Synthesis, structure, Li+ conductivity, Li+ dynamics and applications." *Progress in Materials Science* **2017***,* 88, 325-411. http://dx.doi.org/10.1016/j.pmatsci.2017.04.007

[12]   N. Kamaya, K. Homma, Y. Yamakawa, M. Hirayama, R. Kanno, M. Yonemura*, et al.* "A lithium superionic conductor." *Nature Materials* **2011***,* 10, 682-686. http://dx.doi.org/10.1038/nmat3066

[13]   J. T. Kummer "Beta-alumina Electrolytes." *Journal of the Electrochemical Society* **1972***,* 119, 141-175.

[14]   H. Y. P. Hong "Crystal Structure and Ionic Coductivity of $Li_{14}Zn(GeO_4)_4$ and Other New Li^+ Superionic Conductors." *Materials Research Bulletin* **1978***,* 13, 117-124. http://dx.doi.org/10.1016/0025-5408(78)90075-2

[15]   Y. Inaguma, L. Q. Chen, M. Itoh, T. Nakamura, T. Uchida, H. Ikuta, *et al.* "High Ionic Conductivity in LIthium Lanthanum Titanate." *Solid State Communications* **1993**, 86, 689-693. http://dx.doi.org/10.1016/0038-1098(93)90841-a

[16]   X. H. Yu, J. B. Bates, G. E. Jellison, and F. X. Hart "A stable thin-film lithium electrolyte: Lithium phosphorus oxynitride." *Journal of the Electrochemical Society* **1997**, 144, 524-532. http://dx.doi.org/10.1149/1.1837443

[17]   P. E. Stallworth, J. J. Fontanella, M. C. Wintersgill, C. D. Scheidler, J. J. Immel, S. G. Greenbaum, *et al.* "NMR, DSC and High Pressure Electrical Conductivity Studies on Liquid and Hybrid Electrolytes." *Journal of Power Sources* **1999**, 81, 739-747. http://dx.doi.org/10.1016/s0378-7753(99)00144-5

[18]   U. V. Alpen, A. Rabenau, and G. H. Talat "Ionic Conductivity in Li_3N Single Crystals." *Applied Physics Letters* **1977**, 30, 621-623. http://dx.doi.org/10.1063/1.89283

[19]   K. Kataoka and J. Akimoto "Lithium-ion conductivity and crystal structure of garnet-type solid electrolyte Li7-xLa3Zr2-xTaxO12 using single-crystal." *Journal of the Ceramic Society of Japan* **2019**, 127, 521-526. http://dx.doi.org/10.2109/jcersj2.19022

[20]   Y. Z. Zhu, X. F. He, and Y. F. Mo "Origin of Outstanding Stability in the Lithium Solid Electrolyte Materials: Insights from Thermodynamic Analyses Based on First-Principles Calculations." *Acs Applied Materials & Interfaces* **2015**, 7, 23685-23693. http://dx.doi.org/10.1021/acsami.5b07517

[21]   A. Dorai, N. Kuwata, R. Takekawa, J. Kawamura, K. Kataoka, and J. Akimoto "Diffusion coefficient of lithium ions in garnet-type $Li_{6.5}La_3Zr_{1.5}Ta_{0.5}O_{12}$ single crystal probed by ^{7}Li pulsed field gradient-NMR spectroscopy." *Solid State Ionics* **2018**, 327, 18-26. http://dx.doi.org/10.1016/j.ssi.2018.10.016

[22]   Y. X. Wang and W. Lai "High Ionic Conductivity Lithium Garnet Oxides of Li7-xLa3Zr2-xTaxO12 Compositions." *Electrochemical and Solid State Letters* **2012**, 15, A68-A71. http://dx.doi.org/10.1149/2.024205esl

[23]   Y. X. Wang and W. Lai "Phase transition in lithium garnet oxide ionic conductors Li7La3Zr2O12: The role of Ta substitution and H2O/CO2 exposure." *Journal of Power Sources* **2015**, 275, 612-620. http://dx.doi.org/10.1016/j.jpowsour.2014.11.062

[24]   W. Lai "Transport in Lithium Garnet Oxides as Revealed by Atomistic Simulations." *Annual Review of Materials Research* **2022**, 52, 305-330. http://dx.doi.org/10.1146/annurev-matsci-081720-115334

[25]   L. J. Miara, S. P. Ong, Y. F. Mo, W. D. Richards, Y. Park, J. M. Lee, *et al.* "Effect of Rb and Ta Doping on the Ionic Conductivity and Stability of the Garnet $Li_{7+2x-y}(La_{3-x}Rb_x)(Zr_{2-y}Ta_y)O_{12}$ ($0 <= x <= 0.375$, $0 <= y <= 1$) Superionic Conductor: A First Principles Investigation." *Chemistry of Materials* **2013**, 25, 3048-3055. http://dx.doi.org/10.1021/cm401232r

[26] J. L. Allen, J. Wolfenstine, E. Rangasamy, and J. Sakamoto "Effect of substitution (Ta, Al, Ga) on the conductivity of Li7La3Zr2O12." *Journal of Power Sources* **2012**, 206, 315-319. http://dx.doi.org/10.1016/j.jpowsour.2012.01.131

[27] J. Dai, Y. Jiang, and W. Lai "Study of diffusion and conduction in lithium garnet oxides $Li_xLa_3Zr_{x-5}Ta_{7-x}O_{12}$ by machine learning interatomic potentials." *Phys Chem Chem Phys* **2022**, 24, 15025-15033. http://dx.doi.org/10.1039/d2cp00591c

[28] S. Grimme, C. Bannwarth, and P. Shushkov "A Robust and Accurate Tight-Binding Quantum Chemical Method for Structures, Vibrational Frequencies, and Noncovalent Interactions of Large Molecular Systems Parametrized for All spd-Block Elements (Z=1-86)." *Journal of Chemical Theory and Computation* **2017**, 13, 1989-2009. http://dx.doi.org/10.1021/acs.jctc.7b00118

[29] C. W. Wang, K. Fu, S. P. Kammampata, D. W. McOwen, A. J. Samson, L. Zhang, *et al.* "Garnet-Type Solid-State Electrolytes: Materials, Interfaces, and Batteries." *Chemical Reviews* **2020**, 120, 4257-4300. http://dx.doi.org/10.1021/acs.chemrev.9b00427

[30] B. R. Tao, C. J. Ren, H. D. Li, B. S. Liu, X. B. Jia, X. W. Dong, *et al.* "Thio-/LISICON and LGPS-Type Solid Electrolytes for All-Solid-State Lithium-Ion Batteries." *Advanced Functional Materials* **2022**, 32, 25. http://dx.doi.org/10.1002/adfm.202203551

[31] K. Takada "Progress and prospective of solid-state lithium batteries." *Acta Materialia* **2013**, 61, 759-770. http://dx.doi.org/10.1016/j.actamat.2012.10.034

[32] J. C. Bachman, S. Muy, A. Grimaud, H. H. Chang, N. Pour, S. F. Lux, *et al.* "Inorganic Solid-State Electrolytes for Lithium Batteries: Mechanisms and Properties Governing Ion Conduction." *Chemical Reviews* **2016**, 116, 140-162. http://dx.doi.org/10.1021/acs.chemrev.5b00563

[33] P. Knauth "Inorganic solid Li ion conductors: An overview." *Solid State Ionics* **2009**, 180, 911-916. http://dx.doi.org/10.1016/j.ssi.2009.03.022

[34] Y. F. Y. Yao and J. T. Kummer "ION EXCHANGE PROPERTIES OF AND RATES OF IONIC DIFFUSION IN BETA-ALUMINA." *Journal of Inorganic & Nuclear Chemistry* **1967**, 29, 2453-&.

[35] A. Rabenau and H. Schulz "Re-evaluation of lithium nitrides structure." *Journal of the Less-Common Metals* **1976**, 50, 155-159. http://dx.doi.org/10.1016/0022-5088(76)90263-0

[36] A. Rabenau "Lithium nitride and related materials - case sudy of the use of modern solid-state research techniques." *Solid State Ionics* **1982**, 6, 277-293. http://dx.doi.org/10.1016/0167-2738(82)90012-1

[37] R. Kanno, T. Hata, Y. Kawamoto, and M. Irie "Synthesis of a new lithium ionic conductor, thio-LISICON-lithium germanium sulfide system." *Solid State Ionics* **2000**, 130, 97-104. http://dx.doi.org/10.1016/s0167-2738(00)00277-0

[38]   J. B. Bates, N. J. Dudney, G. R. Gruzalski, R. A. Zuhr, A. Choudhury, C. F. Luck, *et al.* "Electrical properties of amorphous lithium electrolyte thin-films." *Solid State Ionics* **1992,** 53, 647-654. http://dx.doi.org/10.1016/0167-2738(92)90442-r

[39]   V. Thangadurai, H. Kaack, and W. J. F. Weppner "Novel fast lithium ion conduction in garnet-type Li5La3M2O12 (M = Nb, Ta)." *Journal of the American Ceramic Society* **2003,** 86, 437-440. http://dx.doi.org/10.1111/j.1151-2916.2003.tb03318.x

[40]   V. Thangadurai and W. Weppner "Li(6)ALa(2)Ta(2)O(12) (A=Sr, Ba): Novel garnet-like oxides for fast lithium ion conduction." *Advanced Functional Materials* **2005,** 15, 107-112. http://dx.doi.org/10.1002/adfm.200400044

[41]   V. Thangadurai, S. Narayanan, and D. Pinzaru "Garnet-type solid-state fast Li ion conductors for Li batteries: critical review." *Chemical Society Reviews* **2014,** 43, 4714-4727. http://dx.doi.org/10.1039/c4cs00020j

[42]   M. Xu, M. S. Park, J. M. Lee, T. Y. Kim, Y. S. Park, and E. Ma "Mechanisms of Li+ transport in garnet-type cubic Li3+xLa3M2O12 (M = Te, Nb, Zr)." *Physical Review B* **2012,** 85, 5. http://dx.doi.org/10.1103/PhysRevB.85.052301

[43]   E. J. Cussen "The structure of lithium garnets: cation disorder and clustering in a new family of fast Li+ conductors." *Chemical Communications* **2006**, 412-413. http://dx.doi.org/10.1039/b514640b

[44]   M. J. Klenk, S. E. Boeberitz, J. Dai, N. H. Jalarvo, V. K. Peterson, and W. Lai "Lithium self-diffusion in a model lithium garnet oxide Li5La3Ta2O12: A combined quasi-elastic neutron scattering and molecular dynamics study." *Solid State Ionics* **2017,** 312, 1-7. http://dx.doi.org/10.1016/j.ssi.2017.09.022

[45]   J. Awaka, N. Kijima, H. Hayakawa, and J. Akimoto "Synthesis and structure analysis of tetragonal Li7La3Zr2O12 with the garnet-related type structure." *Journal of Solid State Chemistry* **2009,** 182, 2046-2052. http://dx.doi.org/10.1016/j.jssc.2009.05.020

[46]   H. Buschmann, S. Berendts, B. Mogwitz, and J. Janek "Lithium metal electrode kinetics and ionic conductivity of the solid lithium ion conductors "Li7La3Zr2O12" and Li7-xLa3Zr2-xTaxO12 with garnet-type structure." *Journal of Power Sources* **2012,** 206, 236-244. http://dx.doi.org/10.1016/j.jpowsour.2012.01.094

[47]   A. Logeat, T. Koohler, U. Eisele, B. Stiaszny, A. Harzer, M. Tovar, *et al.* "From order to disorder: The structure of lithium-conducting garnets Li7-xLa3TaxZr2-xO12 (x=0-2)." *Solid State Ionics* **2012,** 206, 33-38. http://dx.doi.org/10.1016/j.ssi.2011.10.023

[48]   R. Inada, K. Kusakabe, T. Tanaka, S. Kudo, and Y. Sakurai "Synthesis and properties of Al-free Li7-xLa3Zr2-xTaxO12 garnet related oxides." *Solid State Ionics* **2014,** 262, 568-572. http://dx.doi.org/10.1016/j.ssi.2013.09.008

[49]   N. Hamao, K. Kataoka, N. Kijima, and J. Akimoto "Synthesis, crystal structure and conductive properties of garnet-type lithium ion conductor Al-free Li7-xLa3Zr2-xTaxO12

(0 <= x <= 0.6)." *Journal of the Ceramic Society of Japan* **2016**, 124, 678-683. http://dx.doi.org/10.2109/jcersj2.16019

[50] Y. Gong, Z. G. Liu, Y. J. Jin, J. H. Ouyang, L. Chen, and Y. J. Wang "Effect of sintering process on the microstructure and ionic conductivity of Li7-xLa3Zr2-xTaxO12 ceramics." *Ceramics International* **2019**, 45, 18439-18444. http://dx.doi.org/10.1016/j.ceramint.2019.06.061

[51] M. Y. Yi, T. Liu, X. N. Wang, J. Y. Li, C. Wang, and Y. C. Mo "High densification and Li-ion conductivity of Al-free Li7-xLa3Zr2-xTaxO12 garnet solid electrolyte prepared by using ultrafine powders." *Ceramics International* **2019**, 45, 786-792. http://dx.doi.org/10.1016/j.ceramint.2018.09.245

[52] Y. T. Li, J. T. Han, C. A. Wang, H. Xie, and J. B. Goodenough "Optimizing Li+ conductivity in a garnet framework." *Journal of Materials Chemistry* **2012**, 22, 15357-15361. http://dx.doi.org/10.1039/c2jm31413d

[53] Y. Matsuda, K. Sakamoto, M. Matsui, O. Yamamoto, Y. Takeda, and N. Imanishi "Phase formation of a garnet-type lithium-ion conductor $Li_{7-3x}Al_xLa_3Zr_2O_{12}$." *Solid State Ionics* **2015**, 277, 23-29. http://dx.doi.org/10.1016/j.ssi.2015.04.011

[54] Y. Matsuda, Y. Itami, K. Hayamizu, T. Ishigaki, M. Matsui, Y. Takeda*, et al.* "Phase relation, structure and ionic conductivity of Li7-x-3yAlyLa3Zr2-xTaxO12." *Rsc Advances* **2016**, 6, 78210-78218. http://dx.doi.org/10.1039/c6ra13317g

[55] M. Botros, R. Djenadic, O. Clemens, M. Moller, and H. Hahn "Field assisted sintering of fine-grained Li7-3xLa3Zr2AlxO12 solid electrolyte and the influence of the microstructure on the electrochemical performance." *Journal of Power Sources* **2016**, 309, 108-115. http://dx.doi.org/10.1016/j.jpowsour.2016.01.086

[56] C. Bernuy-Lopez, W. Manalastas, J. M. L. del Amo, A. Aguadero, F. Aguesse, and J. A. Kilner "Atmosphere Controlled Processing of Ga-Substituted Garnets for High Li-Ion Conductivity Ceramics." *Chemistry of Materials* **2014**, 26, 3610-3617. http://dx.doi.org/10.1021/cm5008069

[57] R. Wagner, G. J. Redhammer, D. Rettenwander, A. Senyshyn, W. Schmidt, M. Wilkening*, et al.* "Crystal Structure of Garnet-Related Li-Ion Conductor Li7-3xGaxLa3Zr2O12: Fast Li-Ion Conduction Caused by a Different Cubic Modification?", *Chemistry of Materials* **2016**, 28, 1861-1871. http://dx.doi.org/10.1021/acs.chemmater.6b00038

[58] J. F. Wu, W. K. Pang, V. K. Peterson, L. Wei, and X. Guo "Garnet-Type Fast Li-Ion Conductors with High Ionic Conductivities for All-Solid-State Batteries." *Acs Applied Materials & Interfaces* **2017**, 9, 12461-12468. http://dx.doi.org/10.1021/acsami.7b00614

[59] S. Ohta, T. Kobayashi, and T. Asaoka "High lithium ionic conductivity in the garnet-type oxide $Li_{7-x}La_3(Zr_{2-x}, Nb_x)O_{12}$ (X=0-2)." *Journal of Power Sources* **2011**, 196, 3342-3345. http://dx.doi.org/10.1016/j.jpowsour.2010.11.089

[60] D. W. Wang, G. M. Zhong, W. K. Pang, Z. P. Guo, Y. X. Li, M. J. McDonald, *et al.* "Toward Understanding the Lithium Transport Mechanism in Garnet-type Solid Electrolytes: Li+ Ion Exchanges and Their Mobility at Octahedral/Tetrahedral Sites." *Chemistry of Materials* **2015**, 27, 6650-6659. http://dx.doi.org/10.1021/acs.chemmater.5b02429

[61] L. Dhivya, N. Janani, B. Palanivel, and R. Murugan "Li+ transport properties of W substituted Li7La3Zr2O12 cubic lithium garnets." *Aip Advances* **2013**, 3, 21. http://dx.doi.org/10.1063/1.4818971

[62] X. T. Liu, Y. Li, T. T. Yang, Z. Z. Cao, W. Y. He, Y. F. Gao, *et al.* "High lithium ionic conductivity in the garnet-type oxide Li7-2xLa3Zr2-xMoxO12 (x=0-0.3) ceramics by sol-gel method." *Journal of the American Ceramic Society* **2017**, 100, 1527-1533. http://dx.doi.org/10.1111/jace.14736

[63] P. Bottke, D. Rettenwander, W. Schmidt, G. Amthauer, and M. Wilkening "Ion Dynamics in Solid Electrolytes: NMR Reveals the Elementary Steps of Li+ Hopping in the Garnet Li6.5La3Zr1.75Mo0.25O12." *Chemistry of Materials* **2015**, 27, 6571-6582. http://dx.doi.org/10.1021/acs.chemmater.5b02231

[64] P. Hohenberg and W. Kohn "Inhomogeneous Electron Gas." *Physical Review B* **1964**, 136, B864-B871. http://dx.doi.org/10.1103/PhysRev.136.B864

[65] W. Kohn and L. J. Sham "SELF-CONSISTENT EQUATIONS INCLUDING EXCHANGE AND CORRELATION EFFECTS." *Physical Review* **1965**, 140, 1133-&. http://dx.doi.org/10.1103/PhysRev.140.A1133

[66] J. P. Perdew, K. Burke, and M. Ernzerhof "Generalized gradient approximation made simple." *Physical Review Letters* **1996**, 77, 3865-3868. http://dx.doi.org/10.1103/PhysRevLett.77.3865

[67] U. von Barth "Basic density-functional theory - an overview." *Physica Scripta* **2004**, T109, 9-39. http://dx.doi.org/10.1238/Physica.Topical.109a00009

[68] J. P. Perdew, A. Ruzsinszky, G. I. Csonka, O. A. Vydrov, G. E. Scuseria, L. A. Constantin, *et al.* "Restoring the density-gradient expansion for exchange in solids and surfaces." *Physical Review Letters* **2008**, 100, 4. http://dx.doi.org/10.1103/PhysRevLett.100.136406

[69] M. J. Klenk and W. Lai "Effect of exchange-correlation functionals on the density functional theory simulation of phase transformation of fast-ion conductors: A case study in the Li garnet oxide Li7La3Zr2O12." *Computational Materials Science* **2017**, 134, 132-136. http://dx.doi.org/10.1016/j.commatsci.2017.03.039

[70] M. Elstner, D. Porezag, G. Jungnickel, J. Elsner, M. Haugk, T. Frauenheim, *et al.* "Self-consistent-charge density-functional tight-binding method for simulations of complex materials properties." *Physical Review B* **1998**, 58, 7260-7268. http://dx.doi.org/10.1103/PhysRevB.58.7260

[71] T. Frauenheim, G. Seifert, M. Elstner, T. Niehaus, C. Kohler, M. Amkreutz*, et al.* "Atomistic simulations of complex materials: ground-state and excited-state properties." *Journal of Physics-Condensed Matter* **2002***,* 14, 3015-3047. http://dx.doi.org/10.1088/0953-8984/14/11/313

[72] P. Koskinen and V. Makinen "Density-functional tight-binding for beginners." *Computational Materials Science* **2009***,* 47, 237-253. http://dx.doi.org/10.1016/j.commatsci.2009.07.013

[73] D. Porezag, T. Frauenheim, T. Kohler, G. Seifert, and R. Kaschner "Construction of tight-binding-like potentials on the basis of density-functional theory: Application to carbon." *Physical Review B* **1995***,* 51, 12947-12957. http://dx.doi.org/10.1103/PhysRevB.51.12947

[74] P. Cieplak, F. Y. Dupradeau, Y. Duan, and J. M. Wang "Polarization effects in molecular mechanical force fields." *Journal of Physics-Condensed Matter* **2009***,* 21, 21. http://dx.doi.org/10.1088/0953-8984/21/33/333102

[75] S. W. Rick, S. J. Stuart, and B. J. Berne "Dynamical fluctuating charge force fields: Application to liquid water." *Journal of Chemical Physics* **1994***,* 101, 6141-6156. http://dx.doi.org/10.1063/1.468398

[76] J. Dai, Q. Chen, T. Glossmann, and W. Lai "Comparison of interatomic potential models on the molecular dynamics simulation of fast-ion conductors: A case study of a Li garnet oxide Li7La3Zr2O12." *Computational Materials Science* **2019***,* 162, 333-339. http://dx.doi.org/10.1016/j.commatsci.2019.02.044

[77] S. Tazi, J. J. Molina, B. Rotenberg, P. Turq, R. Vuilleumier, and M. Salanne "A transferable ab initio based force field for aqueous ions." *Journal of Chemical Physics* **2012***,* 136, 12. http://dx.doi.org/10.1063/1.3692965

[78] K. T. Tang and J. P. Toennies "An improved simple model for the van der Waals potential based on universal damping functions for the dispersion coefficients." *Journal of Chemical Physics* **1984***,* 80, 3726-3741. http://dx.doi.org/10.1063/1.447150

[79] J. Behler "Atom-centered symmetry functions for constructing high-dimensional neural network potentials." *Journal of Chemical Physics* **2011***,* 134, 13. http://dx.doi.org/10.1063/1.3553717

[80] M. Rupp, A. Tkatchenko, K. R. Muller, and O. A. von Lilienfeld "Fast and Accurate Modeling of Molecular Atomization Energies with Machine Learning." *Physical Review Letters* **2012***,* 108, 5. http://dx.doi.org/10.1103/PhysRevLett.108.058301

[81] F. Faber, A. Lindmaa, O. A. von Lilienfeld, and R. Armiento "Crystal structure representations for machine learning models of formation energies." *International Journal of Quantum Chemistry* **2015***,* 115, 1094-1101. http://dx.doi.org/10.1002/qua.24917

[82] A. P. Bartok, R. Kondor, and G. Csanyi "On representing chemical environments." *Physical Review B* **2013***,* 87, 16. http://dx.doi.org/10.1103/PhysRevB.87.184115

[83]   M. Hellström and J. Behler, "Neural Network Potentials in Materials Modeling," in *Handbook of Materials Modeling: Methods: Theory and Modeling*, W. Andreoni and S. Yip, Eds., ed Cham: Springer International Publishing, 2020, pp. 661-680.

[84]   N. Artrith and A. Urban "An implementation of artificial neural-network potentials for atomistic materials simulations: Performance for TiO2." *Computational Materials Science* **2016***, 114, 135-150. http://dx.doi.org/10.1016/j.commatsci.2015.11.047

[85]   M. J. Klenk and W. Lai "Finite-size effects on the molecular dynamics simulation of fast-ion conductors: A case study of lithium garnet oxide Li7La3Zr2O12." *Solid State Ionics* **2016***, 289, 143-149. http://dx.doi.org/10.1016/j.ssi.2016.03.002

[86]   Y. X. Wang, A. Huq, and W. Lai "Insight into lithium distribution in lithium-stuffed garnet oxides through neutron diffraction and atomistic simulation: Li7-xLa3Zr2-xTaxO12 (x=0-2) series." *Solid State Ionics* **2014***, 255, 39-49. http://dx.doi.org/10.1016/j.ssi.2013.11.017

[87]   F. Ercolessi and J. B. Adams "Interatomic Potentials from First-Principles Calculations: The Force-Matching Method." *Europhysics Letters* **1994***, 26, 583-588. http://dx.doi.org/10.1209/0295-5075/26/8/005

[88]   A. Carre, S. Ispas, J. Horbach, and W. Kob "Developing empirical potentials from ab initio simulations: The case of amorphous silica." *Computational Materials Science* **2016***, 124, 323-334. http://dx.doi.org/10.1016/j.commatsci.2016.07.041

[89]   N. G. Limas and T. A. Manz "Introducing DDEC6 atomic population analysis: part 2. Computed results for a wide range of periodic and nonperiodic materials." *Rsc Advances* **2016***, 6, 45727-45747. http://dx.doi.org/10.1039/c6ra05507a

[90]   T. A. Manz "Introducing DDEC6 atomic population analysis: part 3. Comprehensive method to compute bond orders." *Rsc Advances* **2017***, 7, 45552-45581. http://dx.doi.org/10.1039/c7ra07400j

[91]   T. A. Manz and N. G. Limas "Introducing DDEC6 atomic population analysis: part 1. Charge partitioning theory and methodology." *Rsc Advances* **2016***, 6, 47771-47801. http://dx.doi.org/10.1039/c6ra04656h

[92]   J.-P. Hansen and I. R. McDonald, *Theory of simple liquids: with applications to soft matter*, 4 ed.: Academic Press, 2013.

[93]   G. Williams and D. C. Watts "NON-SYMMETRICAL DIELECTRIC RELAXATION BEHAVIOUR ARISING FROM A SIMPLE EMPIRICAL DECAY FUNCTION." *Transactions of the Faraday Society* **1970***, 66, 80-+. http://dx.doi.org/10.1039/tf9706600080

[94]   K. Trachenko and V. V. Brazhkin "Collective modes and thermodynamics of the liquid state." *Reports on Progress in Physics* **2016***, 79, 36. http://dx.doi.org/10.1088/0034-4885/79/1/016502

[95]   K. L. Ngai "Short-time and long-time relaxation dynamics of glass-forming substances: a coupling model perspective." *Journal of Physics-Condensed Matter* **2000**, 12, 6437-6451. http://dx.doi.org/10.1088/0953-8984/12/29/316

[96]   H. Jobic and D. N. Theodorou "Quasi-elastic neutron scattering and molecular dynamics simulation as complementary techniques for studying diffusion in zeolites." *Microporous and Mesoporous Materials* **2007**, 102, 21-50. http://dx.doi.org/10.1016/j.micromeso.2006.12.034

[97]   K. S. Singwi and A. Sjolander "DIFFUSIVE MOTIONS IN WATER AND COLD NEUTRON SCATTERING." *Physical Review* **1960**, 119, 863-871. http://dx.doi.org/10.1103/PhysRev.119.863

[98]   E. Helfand "TRANSPORT COEFFICIENTS FROM DISSIPATION IN A CANONICAL ENSEMBLE." *Physical Review* **1960**, 119, 1-9. http://dx.doi.org/10.1103/PhysRev.119.1

[99]   A. S. Nowick and B. S. Berry, *Anelastic Relaxation in Crystalline Solids*: Academic Press, 1972.

[100]   Z. Deng, Z. B. Wang, I. H. Chu, J. Luo, and S. P. Ong "Elastic Properties of Alkali Superionic Conductor Electrolytes from First Principles Calculations." *Journal of the Electrochemical Society* **2016**, 163, A67-A74. http://dx.doi.org/10.1149/2.0061602jes

[101]   S. Adams and R. P. Rao "Ion transport and phase transition in $Li_{7-x}La_3(Zr_{2-x}M_x)O_{12}$ (M = Ta^{5+}, Nb^{5+}, x=0, 0.25)." *Journal of Materials Chemistry* **2012**, 22, 1426-1434. http://dx.doi.org/10.1039/c1jm14588f

[102]   C. Chen, Z. H. Lu, and F. Ciucci "Data mining of molecular dynamics data reveals Li diffusion characteristics in garnet Li7La3Zr2O12." *Scientific Reports* **2017**, 7, 8. http://dx.doi.org/10.1038/srep40769

[103]   M. Klenk and W. Lai "Local structure and dynamics of lithium garnet ionic conductors: tetragonal and cubic Li7La3Zr2O7." *Physical Chemistry Chemical Physics* **2015**, 17, 8758-8768. http://dx.doi.org/10.1039/c4cp05690f

[104]   M. Burbano, D. Carlier, F. Boucher, B. J. Morgan, and M. Salanne "Sparse Cyclic Excitations Explain the Low Ionic Conductivity of Stoichiometric Li7La3Zr2O12." *Physical Review Letters* **2016**, 116, 6. http://dx.doi.org/10.1103/PhysRevLett.116.135901

[105]   P. J. Mitchell and D. Fincham "Shell model simulations by adiabatic dynamics." *Journal of Physics-Condensed Matter* **1993**, 5, 1031-1038. http://dx.doi.org/10.1088/0953-8984/5/8/006

[106]   J. VandeVondele, M. Krack, F. Mohamed, M. Parrinello, T. Chassaing, and J. Hutter "QUICKSTEP: Fast and accurate density functional calculations using a mixed Gaussian and plane waves approach." *Computer Physics Communications* **2005**, 167, 103-128. http://dx.doi.org/10.1016/j.cpc.2004.12.014

[107] J. Hutter, M. Iannuzzi, F. Schiffmann, and J. VandeVondele "CP2K: atomistic simulations of condensed matter systems." *Wiley Interdisciplinary Reviews-Computational Molecular Science* **2014**, 4, 15-25. http://dx.doi.org/10.1002/wcms.1159

[108] G. I. Csonka, J. P. Perdew, A. Ruzsinszky, P. H. T. Philipsen, S. Lebegue, J. Paier, *et al.* "Assessing the performance of recent density functionals for bulk solids." *Physical Review B* **2009**, 79, 14. http://dx.doi.org/10.1103/PhysRevB.79.155107

[109] G. Kresse and D. Joubert "From ultrasoft pseudopotentials to the projector augmented-wave method." *Physical Review B* **1999**, 59, 1758-1775. http://dx.doi.org/10.1103/PhysRevB.59.1758

[110] G. Kresse and J. Furthmuller "Efficient iterative schemes for ab initio total-energy calculations using a plane-wave basis set." *Physical Review B* **1996**, 54, 11169-11186. http://dx.doi.org/10.1103/PhysRevB.54.11169

[111] W. Smith and T. R. Forester "DL_POLY_2.0: A general-purpose parallel molecular dynamics simulation package." *Journal of Molecular Graphics* **1996**, 14, 136-141. http://dx.doi.org/10.1016/s0263-7855(96)00043-4

[112] C. A. Geiger, E. Alekseev, B. Lazic, M. Fisch, T. Armbruster, R. Langner, *et al.* "Crystal Chemistry and Stability of "Li7La3Zr2O12" Garnet: A Fast Lithium-Ion Conductor." *Inorganic Chemistry* **2011**, 50, 1089-1097. http://dx.doi.org/10.1021/ic101914e

[113] M. Kotobuki, K. Kanamura, Y. Sato, and T. Yoshida "Fabrication of all-solid-state lithium battery with lithium metal anode using Al2O3-added Li7La3Zr2O12 solid electrolyte." *Journal of Power Sources* **2011**, 196, 7750-7754. http://dx.doi.org/10.1016/j.jpowsour.2011.04.047

[114] H. Buschmann, J. Dolle, S. Berendts, A. Kuhn, P. Bottke, M. Wilkening, *et al.* "Structure and dynamics of the fast lithium ion conductor "Li7La3Zr2O12"." *Physical Chemistry Chemical Physics* **2011**, 13, 19378-19392. http://dx.doi.org/10.1039/c1cp22108f

[115] G. Larraz, A. Orera, and M. L. Sanjuan "Cubic phases of garnet-type Li7La3Zr2O12: the role of hydration." *Journal of Materials Chemistry A* **2013**, 1, 11419-11428. http://dx.doi.org/10.1039/c3ta11996c

[116] R. Jalem, Y. Yamamoto, H. Shiiba, M. Nakayama, H. Munakata, T. Kasuga, *et al.* "Concerted Migration Mechanism in the Li Ion Dynamics of Garnet-Type Li7La3Zr2O12." *Chemistry of Materials* **2013**, 25, 425-430. http://dx.doi.org/10.1021/cm303542x

[117] A. Kuhn, S. Narayanan, L. Spencer, G. Goward, V. Thangadurai, and M. Wilkening "Li self-diffusion in garnet-type $Li_7La_3Zr_2O_{12}$ as probed directly by diffusion-induced ^7Li spin-lattice relaxation NMR spectroscopy." *Physical Review B* **2011**, 83, 11. http://dx.doi.org/10.1103/PhysRevB.83.094302

[118] M. Matsui, K. Takahashi, K. Sakamoto, A. Hirano, Y. Takeda, O. Yamamoto*, et al.* "Phase stability of a garnet-type lithium ion conductor Li7La3Zr2O12." *Dalton Transactions* **2014***, 43, 1019-1024. http://dx.doi.org/10.1039/c3dt52024b

[119] S. Narayanan, A. K. Baral, and V. Thangadurai "Dielectric characteristics of fast Li ion conducting garnet-type Li5+2xLa3Nb2-xYxO12 (x=0.25, 0.5 and 0.75)." *Physical Chemistry Chemical Physics* **2016***, 18, 15418-15426. http://dx.doi.org/10.1039/c6cp02287a

[120] C. Monroe and J. Newman "The impact of elastic deformation on deposition kinetics at lithium/polymer interfaces." *Journal of the Electrochemical Society* **2005***, 152, A396-A404. http://dx.doi.org/10.1149/1.1850854

[121] J. E. Ni, E. D. Case, J. S. Sakamoto, E. Rangasamy, and J. B. Wolfenstine "Room temperature elastic moduli and Vickers hardness of hot-pressed LLZO cubic garnet." *Journal of Materials Science* **2012***, 47, 7978-7985. http://dx.doi.org/10.1007/s10853-012-6687-5

[122] K. Lee, D. Yoo, W. Jeong, and S. Han "SIMPLE-NN: An efficient package for training and executing neural-network interatomic potentials." *Computer Physics Communications* **2019***, 242, 95-103. http://dx.doi.org/10.1016/j.cpc.2019.04.014

[123] L. Himanen, M. O. J. Jager, E. V. Morooka, F. F. Canova, Y. S. Ranawat, D. Z. Gao*, et al.* "DScribe: Library of descriptors for machine learning in materials science." *Computer Physics Communications* **2020***, 247, 12. http://dx.doi.org/10.1016/j.cpc.2019.106949

[124] W. W. Li, Y. Ando, E. Minamitani, and S. Watanabe "Study of Li atom diffusion in amorphous Li3PO4 with neural network potential." *Journal of Chemical Physics* **2017***, 147, 10. http://dx.doi.org/10.1063/1.4997242

[125] W. Jeong, K. Lee, D. Yoo, D. Lee, and S. Han "Toward Reliable and Transferable Machine Learning Potentials: Uniform Training by Overcoming Sampling Bias." *Journal of Physical Chemistry C* **2018***, 122, 22790-22795. http://dx.doi.org/10.1021/acs.jpcc.8b08063

[126] F. Aguesse, W. Manalastas, L. Buannic, J. M. L. del Amo, G. Singh, A. Llordes*, et al.* "Investigating the Dendritic Growth during Full Cell Cycling of Garnet Electrolyte in Direct Contact with Li Metal." *Acs Applied Materials & Interfaces* **2017***, 9, 3808-3816. http://dx.doi.org/10.1021/acsami.6b13925

[127] M. Van den Bossche, H. Gronbeck, and B. Hammer "Tight-Binding Approximation-Enhanced Global Optimization." *Journal of Chemical Theory and Computation* **2018***, 14, 2797-2807. http://dx.doi.org/10.1021/acs.jctc.8b00039

[128] S. Plimpton "Fast Parallel Algorithms for Short-Range Molecular Dynamics." *J. Computa. Phys.* **1995***, 117, 1-19. http://dx.doi.org/10.1006/jcph.1995.1039

[129] B. Stanje, D. Rettenwander, S. Breuer, M. Uitz, S. Berendts, M. Lerch*, et al.* "Solid Electrolytes: Extremely Fast Charge Carriers in Garnet-Type Li6La3ZrTaO12 Single Crystals." *Annalen Der Physik* **2017***,* 529, 9. http://dx.doi.org/10.1002/andp.201700140

[130] T. Thompson, A. Sharafi, M. D. Johannes, A. Huq, J. L. Allen, J. Wolfenstine*, et al.* "A Tale of Two Sites: On Defining the Carrier Concentration in Garnet-Based Ionic Conductors for Advanced Li Batteries." *Advanced Energy Materials* **2015***,* 5, 9. http://dx.doi.org/10.1002/aenm.201500096

[131] K. Kataoka and J. Akimoto "High Ionic Conductor Member of Garnet-Type Oxide Li6.5La3Zr1.5Ta0.5O12." *Chemelectrochem* **2018***,* 5, 2551-2557. http://dx.doi.org/10.1002/celc.201800679

[132] K. Hayamizu, Y. Terada, K. Kataoka, and J. Akimoto "Toward understanding the anomalous Li diffusion in inorganic solid electrolytes by studying a single-crystal garnet of LLZO-Ta by pulsed-gradient spin-echo nuclear magnetic resonance spectroscopy." *Journal of Chemical Physics* **2019***,* 150, 9. http://dx.doi.org/10.1063/1.5089576

[133] Y. Jin, K. Liu, J. L. Lang, D. Zhuo, Z. Y. Huang, C. A. Wang*, et al.* "An intermediate temperature garnet-type solid electrolyte-based molten lithium battery for grid energy storage." *Nature Energy* **2018***,* 3, 732-738. http://dx.doi.org/10.1038/s41560-018-0198-9

[134] K. Xu "Nonaqueous liquid electrolytes for lithium-based rechargeable batteries." *Chemical Reviews* **2004***,* 104, 4303-4417. http://dx.doi.org/10.1021/cr030203g

[135] K. M. Diederichsen, H. G. Buss, and B. D. McCloskey "The Compensation Effect in the Vogel-Tammann-Fulcher (VTF) Equation for Polymer-Based Electrolytes." *Macromolecules* **2017***,* 50, 3832-3841. http://dx.doi.org/10.1021/acs.macromol.7b00423

[136] G. Y. Gu, S. Bouvier, C. Wu, R. Laura, M. Rzeznik, and K. M. Abraham "2-Methoxyethyl (methyl) carbonate-based electrolytes for Li-ion batteries." *Electrochimica Acta* **2000***,* 45, 3127-3139. http://dx.doi.org/10.1016/s0013-4686(00)00394-7

[137] X. F. He, Y. Z. Zhu, and Y. F. Mo "Origin of fast ion diffusion in super-ionic conductors." *Nature Communications* **2017***,* 8. http://dx.doi.org/10.1038/ncomms15893

[138] M. Mottet, A. Marcolongo, T. Laino, and I. Tavernelli "Doping in garnet-type electrolytes: Kinetic and thermodynamic effects from molecular dynamics simulations." *Physical Review Materials* **2019***,* 3. http://dx.doi.org/10.1103/PhysRevMaterials.3.035403

[139] R. Murugan, V. Thangadurai, and W. Weppner "Fast lithium ion conduction in garnet-type Li7La3Zr2O12." *Angewandte Chemie-International Edition* **2007***,* 46, 7778-7781. http://dx.doi.org/10.1002/anie.200701144

[140] S. Sasano, R. Ishikawa, K. Kawahara, T. Kimura, Y. H. Ikuhara, N. Shibata*, et al.* "Grain boundary Li-ion conductivity in (Li0.33La0.56)TiO3 polycrystal." *Applied Physics Letters* **2020***,* 116, 4. http://dx.doi.org/10.1063/1.5141396

[141] B. B. Chen, C. Q. Xu, and J. Q. Zhou "Insights into Grain Boundary in Lithium-Rich Anti-Perovskite as Solid Electrolytes." *Journal of the Electrochemical Society* **2018**, 165, A3946-A3951. http://dx.doi.org/10.1149/2.0831816jes

[142] J. A. Dawson, P. Canepa, T. Famprikis, C. Masquelier, and M. S. Islam "Atomic-Scale Influence of Grain Boundaries on Li-Ion Conduction in Solid Electrolytes for All-Solid-State Batteries." *Journal of the American Chemical Society* **2018**, 140, 362-368. http://dx.doi.org/10.1021/jacs.7b10593

[143] J. A. Dawson, P. Canepa, M. J. Clarke, T. Famprikis, D. Ghosh, and M. S. Islam "Toward Understanding the Different Influences of Grain Boundaries on Ion Transport in Sulfide and Oxide Solid Electrolytes." *Chemistry of Materials* **2019**, 31, 5296-5304. http://dx.doi.org/10.1021/acs.chemmater.9b01794

[144] S. Yu and D. J. Siegel "Grain Boundary Contributions to Li-Ion Transport in the Solid Electrolyte Li7La3Zr2O12 (LLZO)." *Chemistry of Materials* **2017**, 29, 9639-9647. http://dx.doi.org/10.1021/acs.chemmater.7b02805

[145] H. Shiiba, N. Zettsu, M. Yamashita, H. Onodera, R. Jalem, M. Nakayama, *et al.* "Molecular Dynamics Studies on the Lithium Ion Conduction Behaviors Depending on Tilted Grain Boundaries with Various Symmetries in Garnet-Type Li7La3Zr2O12." *Journal of Physical Chemistry C* **2018**, 122, 21755-21762. http://dx.doi.org/10.1021/acs.jpcc.8b06275

[146] B. Gao, R. Jalem, H. K. Tian, and Y. Tateyama "Revealing Atomic-Scale Ionic Stability and Transport around Grain Boundaries of Garnet $Li_7La_3Zr_2O_{12}$ Solid Electrolyte." *Advanced Energy Materials* **2021**, 12, 202102151. http://dx.doi.org/10.1002/aenm.202102151

[147] M. A. Tschopp, K. N. Solanki, F. Gao, X. Sun, M. A. Khaleel, and M. F. Horstemeyer "Probing grain boundary sink strength at the nanoscale: Energetics and length scales of vacancy and interstitial absorption by grain boundaries in alpha-Fe." *Physical Review B* **2012**, 85, 21. http://dx.doi.org/10.1103/PhysRevB.85.064108

[148] M. Rajagopalan, M. A. Tschopp, and K. N. Solanki "Grain Boundary Segregation of Interstitial and Substitutional Impurity Atoms in Alpha-Iron." *Jom* **2014**, 66, 129-138. http://dx.doi.org/10.1007/s11837-013-0807-9

[149] W. E. Tenhaeff, E. Rangasamy, Y. Y. Wang, A. P. Sokolov, J. Wolfenstine, J. Sakamoto, *et al.* "Resolving the Grain Boundary and Lattice Impedance of Hot-Pressed Li7La3Zr2O12 Garnet Electrolytes." *Chemelectrochem* **2014**, 1, 375-378. http://dx.doi.org/10.1002/celc.201300022

[150] B. J. Morgan "Lattice-geometry effects in garnet solid electrolytes: a lattice-gas Monte Carlo simulation study." *Royal Society Open Science* **2017**, 4, 21. http://dx.doi.org/10.1098/rsos.170824

[151]   J. Goo, X. Y. Guo, Y. T. Li, Z. H. Ma, X. X. Guo, H. Li, *et al.* "The Ab Initio Calculations on the Areal Specific Resistance of Li-Metal/Li$_7$La$_3$Zr$_2$O$_{12}$ Interphase." *Advanced Theory and Simulations* **2019**, 2, 7. http://dx.doi.org/10.1002/adts.201900028

[152]   B. Gao, R. Jalem, and Y. Tateyama "Surface-Dependent Stability of the Interface between Garnet Li7La3Zr2O12 and the Li Metal in the All-Solid-State Battery from First-Principles Calculations." *Acs Applied Materials & Interfaces* **2020**, 12, 16350-16358. http://dx.doi.org/10.1021/acsami.9b23019

[153]   X. G. Han, Y. H. Gong, K. Fu, X. F. He, G. T. Hitz, J. Q. Dai, *et al.* "Negating interfacial impedance in garnet-based solid-state Li metal batteries." *Nature Materials* **2017**, 16, 572-+. http://dx.doi.org/10.1038/nmat4821